FIBER OPTIC TECHNIQUES FOR REMOTE SENSING

by

Kimberly Dean Bennett

Thesis submitted to the Faculty of the
Virginia Polytechnic Institute and State University
in partial fulfillment of the requirements for the degree of
MASTER OF SCIENCE
in
Electrical Engineering

APPROVED:

_____
Dr. R. O. Claus

_____ _____
Dr. T. C. Poon Dr. L. C. Burton

September, 1985
Blacksburg, Virginia

FIBER OPTIC TECHNIQUES FOR REMOTE SENSING

by

Kimberly Dean Bennett

(ABSTRACT)

The need for sensors demonstrating both high sensitivity and electromagnetic noise immunity has prompted the development of sensing systems based on optical fiber technology. This presentation opens with a short review of fiber optic sensing methods, including a discussion of several devices developed in prominent laboratories. The theoretical and empirical results of a particular technique of distributed pressure sensing appear next. This sensing approach, aimed towards the nondestructive testing of graphite/epoxy composite structures, relies on optical time-domain reflectometry in imbedded optical fibers. The method is investigated primarily in terms of its sensitivity and its effect on the mechanical integrity of the host composite. The work concludes with a discussion of results and ideas relating to microbending sensor research, as well as the design of several novel sensing devices.

ACKNOWLEDGEMENTS

My highest praise and most sincere thanks belong first to my Lord and Friend, Jesus Christ. Throughout my short career I have constantly experienced His very tangible encouragement, guidance, and enabling, as well as the comfort of His presence.

I wish to gratefully acknowledge my advisor, Dr. R.O. Claus, for his help in so many areas of my professional life, and thank him also for the endless hours of stimulating conversation we have shared. I also wish to thank Dr. T.C. Poon and Dr. L.C. Burton for serving on my graduate committee.

In addition, I would like to thank Mr. Eric Park of Inland Motor, for contributing his time and ideas, as well as for the understanding he extended during the last phase of this effort.

I also wish to acknowledge my fellow members of the Acousto-Optic Group. In particular, I thank Scott Jackson, especially for his technical contributions, on which much of this thesis rests, and Jessicah Shih for her technical and moral support.

I would like to thank Dr. Tom Freeman of NASA, Langley, and his staff for their able help in the preparation of com-

posite samples, and A.O. Garg of Siecor for his assistance with OTDR measurements.

Finally I wish to extend many sincere thanks to Alice McCarter for her faithful and able assistance in the preparation of this manuscript.

TABLE OF CONTENTS

Appendix

LIST OF FIGURES

Figure

Chapter I

INTRODUCTION

For thousands of years, man has been concerned with converting energy from one form to another. Burning a piece of wood to change mass energy into light and heat provides an early example. Later, the potential energy of a coiled spring was transformed to kinetic energy to drive mechanical systems. Of considerable importance during the last century has been the conversion of mechanical energy to electrical energy, primarily for the generation of power, and the subsequent conversion of electrical energy to other forms. In the average home for instance, electrical energy enters and is transformed to light energy via light bulbs, heat energy via resistive coils, mechanical or kinetic energy via electric motors, and so on.

The generation and transferal of power is driven by man's insatiable desire to accomplish, to produce. But nearly as fundamental in man is his desire to communicate. This is evidenced in part by the ever-present push to develop new ways to send information from place to place. Such communication not only allows for personal exchange of ideas; it helps man to meet his goal to achieve.

In reality, information is being generated, detected and processed by man in a vast number of ways, often subliminally. For example, the eyes detect a decrease of ambient light below some predetermined threshold, and a lamp is switched on. In this case, the eyes act as an information sensor, one link in a total system. Light energy is received, converted to an electronic brain signal, processed, and another signal is sent to the hand. Chemical energy internal to the body is transformed into mechanical energy, and the switch is turned.

Engineering systems are simply man-made versions of the same, though few work as precisely as the human body. Their overall performance depends in many ways on the sensor used. Generally, a high response to signal and low response to noise is desired, being determined by the efficiency of energy conversion from one form to another. For example, though light creates heat on the skin, the process is inefficient so that hands are rarely used as light level indicators. Much of engineering effort concerns itself with the development of efficient and appropriate sensors for use in larger systems.

This report investigates an increasingly popular method of sensing: the conversion of input variables to light signals in optical fibers. In one class of sensors, referred

to as extrinsic, light signals are captured by the fiber and are guided along its length to a light-to-electric energy converter known as a photodetector. The other chief type of sensor is termed intrinsic. The parameter to be measured actually changes the transmission characteristics of the fiber itself; light inside the fiber is thus affected to create the required signal.

Optical fibers offer the same advantages to sensing systems as they do to telecommunications, [1]. First, the dielectric nature of optical waveguides render them inherently less sensitive to electrical noise than conventional signal carriers [2]. This fact drives much of the development of such sensors, especially in view of mounting concern about electromagnetic pulse (EMP) weaponry and electromagnetic interference (EMI), both designed to destroy or cripple communications. Their chemical structure also makes these sensors safe for certain types of corrosive or high temperature environments which conventional sensors cannot tolerate.

Second, optical fibers can be made responsive to any number of parameters: electric, magnetic, or acoustic fields, displacement, velocity, acceleration, pressure, strain, chemical concentration, or temperature, to name just a few [3,4]. This often constitutes the point of separation between fiber sensor and communications applications. Whereas

communications engineers wish to reduce a fiber's sensitivity to physical perturbations, sensor designers wish to increase and exploit it. Furthermore, because of their small size, and more particularly because of the small wavelength of light, optical sensors can demonstrate extremely high sensitivity. For instance, the measurement of displacements the size of fractions of wavelengths and of magnetic fields of 10^{-9} Gauss was reported as early as 1981, even with what are now considered somewhat crude techniques [4].

Other benefits of fiber optic sensors stem from their geometric versatility. Glass fibers are thin and light, and can be incorporated into an endless variety of sensor configurations. Moreover, because of their common components, fiber sensors and fiber telemetry systems are highly compatible. Besides the obvious advantage of being able to construct all-fiber systems, this means that advances in communications technology often translate into enhanced capabilities in the sensor field.

The first major effort towards fiber optic sensor development began at the Naval Research Laboratory (NRL), Washington, D.C., in 1977 [4]. Early work concentrated on the production of acoustic wave monitors, presumably for undersea applications, but the scope of investigation expanded quickly. Other large-scale operations dedicated to fiber

optic sensors started soon after, notably at United Technologies Research Center, East Hartford, Connecticut [5,6], and Sperry Research Center, Sudbury, Massachusetts [1,7,8]. This resulted in rapid progress in the field, so that when the first thorough review of fiber optic sensors was written by Giallorenzi, *et al*, in 1981, over sixty different sensor types were being developed [4]. Since then, the scale of work and number of researchers in the field has enlarged to the point that writing a truly comprehensive review would be a formidable, if not impossible task.

This presentation is organized into four chapters. Chapter 1 introduces the reader to optical fiber sensors, including a justification for their development. Chapter 2 presents an overview of the basic sensing concepts, providing a few examples of how each concept has been applied. Chapter 3 concentrates on a particular sensor investigated to detect distributed strain in graphite/epoxy composite panels. It includes the motivation, background, and fundamentals of the method, as well as the results of preliminary tests and a computer simulation of the technique. Chapter 4 presents a variety of sensor concepts developed or considered as a part of this work, their intent, any data taken, and computer models where applicable. It also includes a discussion of a few tools and components conceived for use

in fiber sensor design, as well as potential areas for future work.

Chapter II

FIBER OPTIC SENSING TECHNOLOGY

Fiber optic sensors consist of three basic components, the sending electronics and optics, the fiber transmission line, and the receiving optics and electronics. Along the transmission length, a physical process to be measured modulates the light in the fiber. Although one of several mechanisms can be responsible for the light modulation, each is eventually detected as a change in the output light amplitude. The modulating mechanisms are traditionally classified as affecting one of four basic light properties: amplitude, phase, polarization, and wavelength. A fifth mechanism is based on the propagation of various modes of light in a optical fiber. In the following paragraphs, each of these sensing methods will be briefly discussed and a few examples in each category will be reviewed.

2.1 AMPLITUDE SENSORS

Amplitude sensors detect changes in light intensity arising from the conversion of fiber transmission modes to radiating modes. Because of their relative simplicity of design, amplitude sensors are the most developed category of fiber optic sensors. In what are called *extrinsic* sensors, light leaves the fiber, interacts with some phenomenon to be measured, and then is collected either by the sending fiber or by another fiber. This is in contrast to *intrinsic* sensors, which guide their signal intensity along their entire length. Transduction mechanisms for extrinsic sensors include reflecting off a moveable surface, transmitting through a variable filter, or linking the collection ability to the phenomenon directly.

Reflectance-based devices are now well developed and commercially available; object motions ranging from tens of microns to several inches can be reliably measured. The important quantity in such measurements is the ratio of the fiber-reflector separation to the span of the collecting fiber [2]. This can be seen in Figure 2.1, showing the normalized optical intensity versus this ratio for three different cases. A schematic of a pressure sensor based on these curves, consisting of light modulated by a metallic diaphragm, can be seen in Figure 2.2. Furthermore, several

researchers, notably those at Sperry, have extensively investigated both reflectance and transmission designs for use in hydrophones with considerable success [7,9].

A variable transmission design can be seen in Figure 2.3a, where a Schlieren grating is coupled to an incident sound field by means of a diaphragm. A varying acoustic excitation causes relative motion between the gratings and is detected as a modulation of light intensity. In another hydrophone, the coupling between two abutted single-mode fibers is directly affected by the incoming sound, as seen in Figure 2.3b. As the pressure wave propagates across the housing, again the transmitted signal intensity is modulated. However, a major disadvantage is incurred in both the reflectance and transmission designs since the optical signal actually leaves the fiber waveguide, and so is subject to various forms of interference.

Another class of amplitude sensors depends on the effects of microbending a multimode fiber. As light in a fiber rounds the sharp corner caused by a bend, the critical angle is exceeded and higher order modes are no longer totally internally reflected. This conversion of propagating modes to radiating modes adds to the light scattering from bend-induced local refractive index changes to yield a signal loss which implies the amount of bending incurred. Micro-bending

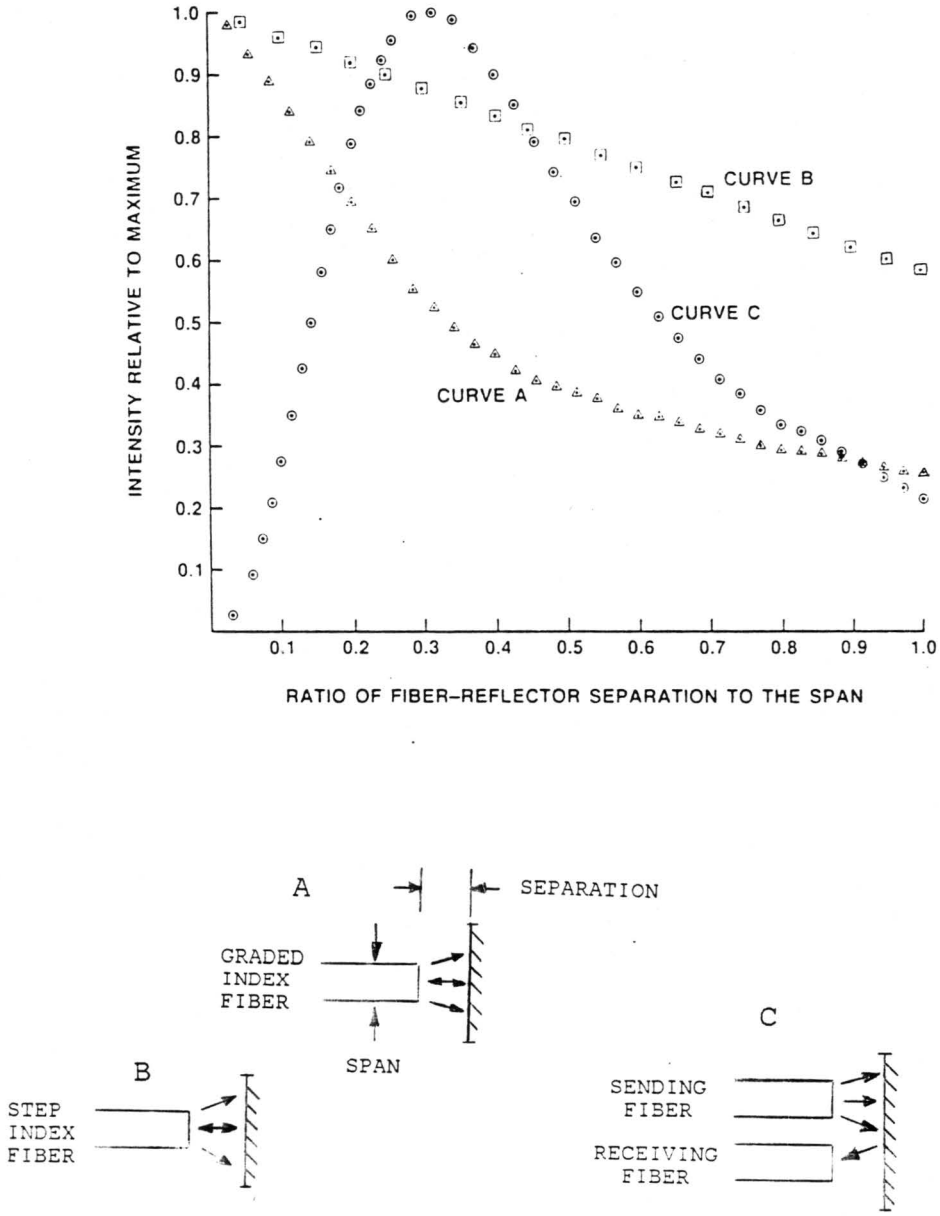

Figure 2.1: Reflected Intensity versus Fiber Separation/Span (after [4])

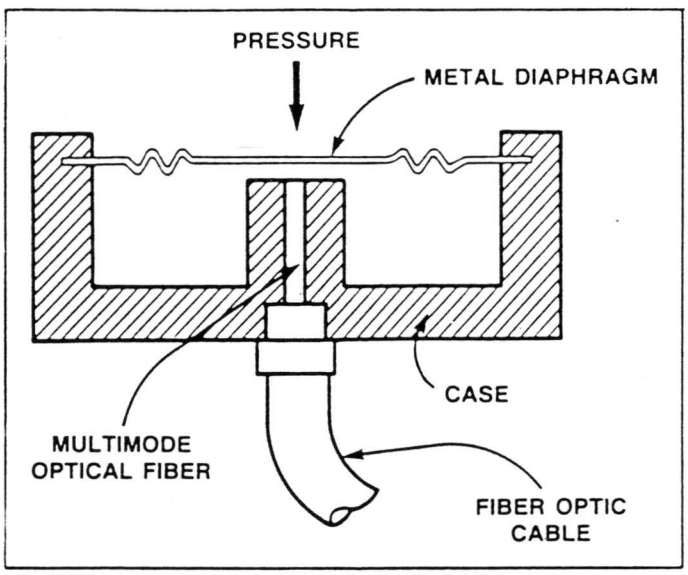

Figure 2.2: Reflection-Based Fiber Optic Pressure Sensor (after [2])

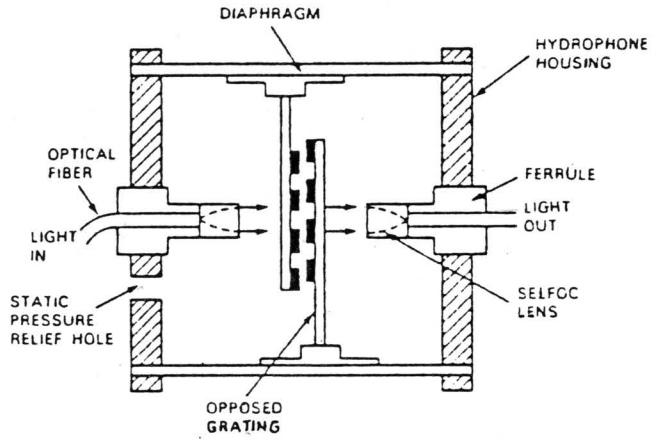

(a)

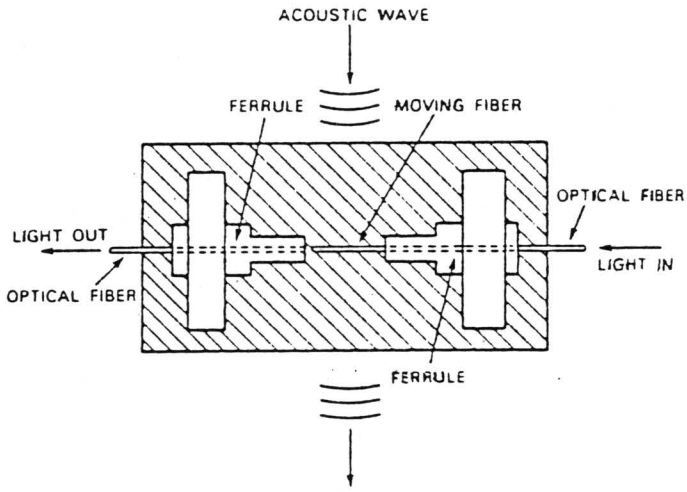

(b)

Figure 2.3: Two Transmission-Based Fiber Optic Pressure Sensors (after [4])

in single mode fiber displays further losses due to core and cladding mode interactions [10]. Bending may be induced by changes in strain, pressure, temperature, or many other parameters. Figure 2.4 shows the conventional microbend sensor consisting of a fiber sandwiched between two deforming surfaces.

As an example, researchers at NRL have demonstrated a microbend-based hydrophone capable of detecting audio frequency signals only 25 dB above the sea state zero [11]. As Figure 2.5 shows, a multimode fiber responds to an acoustic wave by bending into slots milled in a threaded cylinder. In another example, a microbending modulated accelerometer having a linear range from 7×10^{-6} to 0.7 times the gravitational acceleration g was recently reported by workers at OPTECH [2].

Since the signal light never leaves the fiber, microbend sensors have been proven to be quite suitable for distributed sensor arrays using optical time domain reflectometry (OTDR). Investigators at Occidental Research Corporation recently employed this method to monitor the motion of roof strata in various places in coal mines [12]. An even more integrated approach of measuring continuous microbending loss of optical fibers imbedded in composite panels will be presented in Chapter 3.

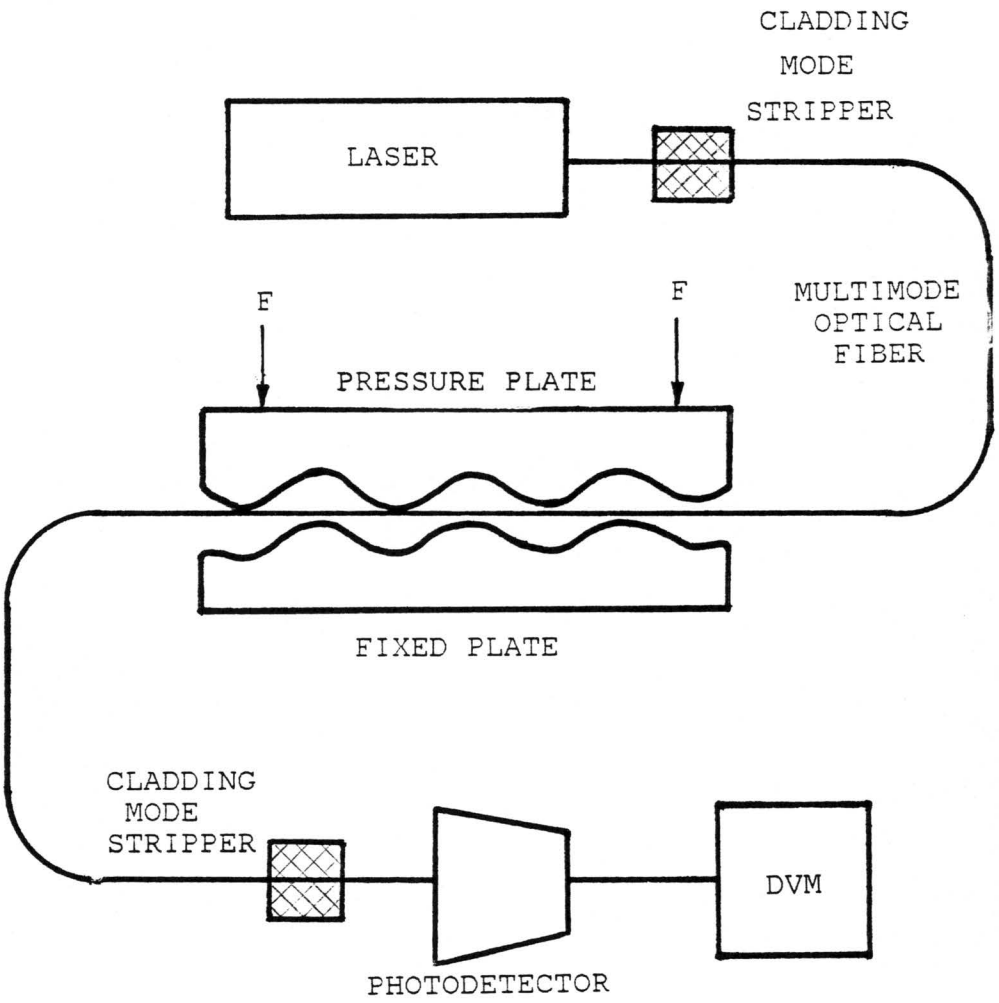

Figure 2.4: Conventional Microbend Sensor

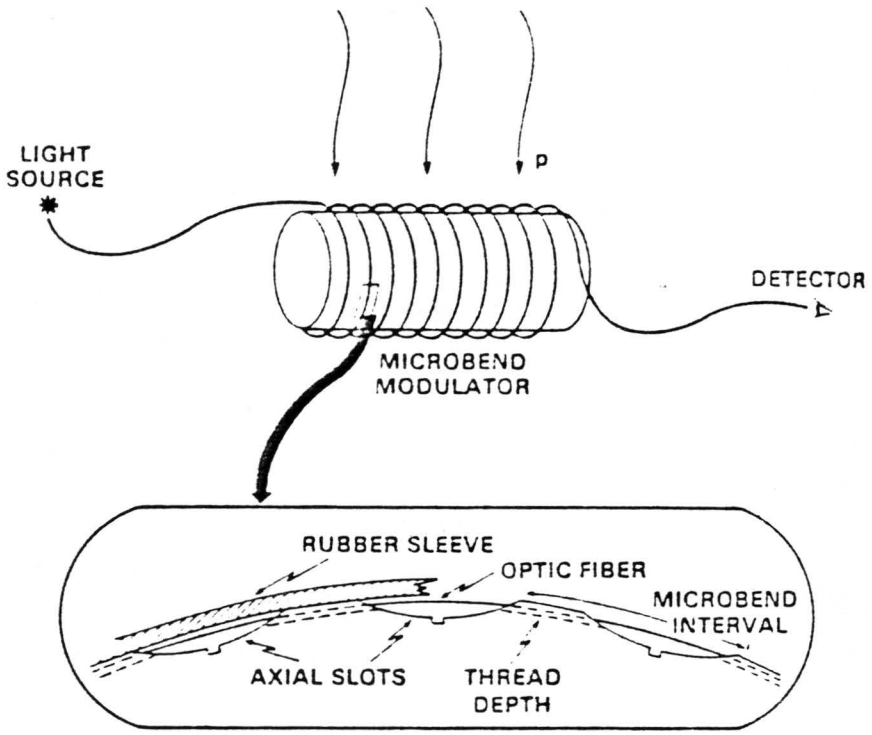

Figure 2.5: Microbend-Based Hydrophone (after [11])

2.2 PHASE SENSORS

Phase sensors all rely on principles of optical interferometry, and thus take one of four basic forms, as seen in Figure 2.6, all employing single mode fiber. Sensors employing the Mach-Zehnder configuration are the most developed type, having been extensively researched at NRL [4,13,14]. In this form, monochromatic, coherent radiation is divided into two rays by a directional coupler. One fiber path is an untouched reference arm, while the other "signal" path is physically perturbed by the process of interest. If the two paths are recombined by a second coupler, an interference pattern appears at the detector. Often the SNR is increased by frequency or phase modulating the reference signal. Demodulation schemes are then chosen suitable for the specific sensor application [4].

Whereas the Mach-Zehnder interferometer detects the path length difference integrated along the entire signal arm, the Fabry-Perot approach actually measures the length of a "cavity" created between the two ends of the fiber. Whether the ends are silvered [2], or unsilvered [15], this has the property of separating the sensing portion of the fiber at the end from the lead portion. Also, if a 2x2 directional coupler is used (as shown), a second photodetector can be used to monitor the laser source, allowing for correction of

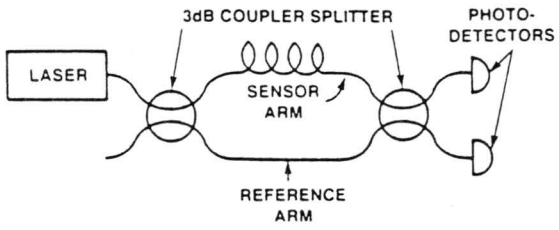

MACH-ZEHNDER

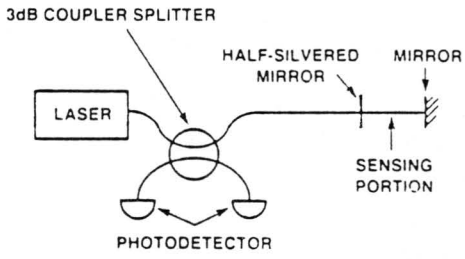

FABRY-PEROT

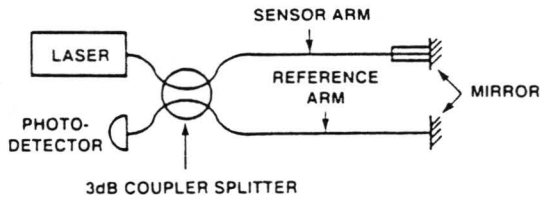

MICHELSON

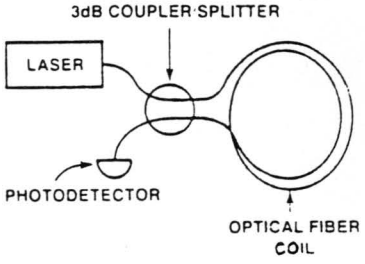

SAGNAC

Figure 2.6: The Four Basic Optical Fiber Interferometers

input power fluctuations. In addition, high sensitivity can often be achieved by increasing the *finesse* of the interferometer. Such devices have been applied to sensors of temperature, vibration, acoustic wave including human voice, ac voltage, and ac and dc magnetic fields [16].

In the Michelson approach, the fibers merely act as light conduits. Both fibers and the reference mirror are fixed, while movement of the signal mirror causes interference to take place at the detector. This has the disadvantage of suggesting the need for either collimating optics at the sensing end or for a high reflectance silver coating applied to the fiber itself, and so is rarely used. However, it has been shown that the Michelson technique is theoretically twice as sensitive as the Mach-Zehnder in certain applications. In thermometry, for example, where changes in the actual fiber length act as the interference mechanism, the light passes through the elongated fiber twice and incurs twice the phase change [17].

Often the signal fiber in the Mach-Zehnder configuration is coated with a special coating which is sensitive to the modulating field [18]. Most often a magnetostrictive coating, which changes its shape in response to an applied magnetic field, is employed [19,20,21]. Depending on the quality of the coating, changes in the applied field imply

changes in the optical path length of the signal arm, and thereby changes in the relative phase between the two arms. Changes smaller than 10^{-12} Gauss per meter of fiber have been detected by this method [22]. Problems traditionally arise from the quality of the coating itself. Recently, however, thick uniform nickel coatings applied to long, continuous lengths of single mode fiber have been reported by engineers at ITT-EOPD [23].

In addition to magnetostrictive coatings, a number of groups have recently applied polymer-based piezoelectric jackets to optical fibers [24]. This coating is easily applied and is inherently sensitive to electric field changes. To date, however, electrically induced optical phase shifts are somewhat lower than theoretical values, presumably due to inefficiencies in the molecular dipole alignment process.

Two main noise sources limit the sensitivity of phase sensors: instability of the wavelength and intensity of the laser source, and random temperature and pressure variations between the two sensing arms. The most common approach to overcoming the latter problem is to couple both sensing arms to the signal field and measure differential phase changes. This technique has been carried out one step further, most recently at Hirst Research Center [25]. In this approach, fiber supporting only two modes (LP_{01} and LP_{11}) is "created"

by using single mode fiber and a laser source just below the cutoff wavelength of the fiber. Interference between these two modes has been demonstrated to be quite stable and repeatable, although the sensitivity of such measurements is predictably two orders of magnitude below the two-fiber arrangement [26]. Figure 2.7a shows the intensity distribution across the endface for these modes; 2.7b shows an experimental arrangement for measuring temperature; 2.7c shows the power variation (fringes) obtained.

The fourth basic phase sensing method arises from the Sagnac effect, used to advantage in fiber optic gyroscopes [4]. Generally light from a single-mode laser diode is split by a directional coupler and injected into opposite ends of a single mode fiber coil. The rays travel in opposite directions around the coil, are recombined by the coupler, and the resulting interference pattern is imaged onto a detector. When the fiber coil rotates, the progress of the beam going in the rotation direction will be relatively slowed, while the progress of the opposite-travelling beam will be aided. This gives rise to a phase shift between the two beams corresponding to the coil rotation rate. Although fiber optic gyros are extremely sensitive [27,28], work is still required to make them practical for common use.

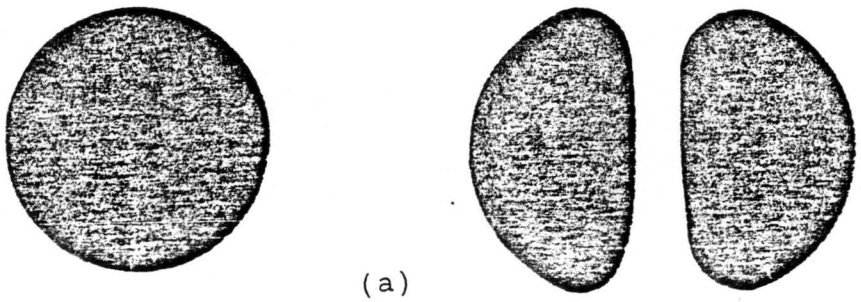

(a)

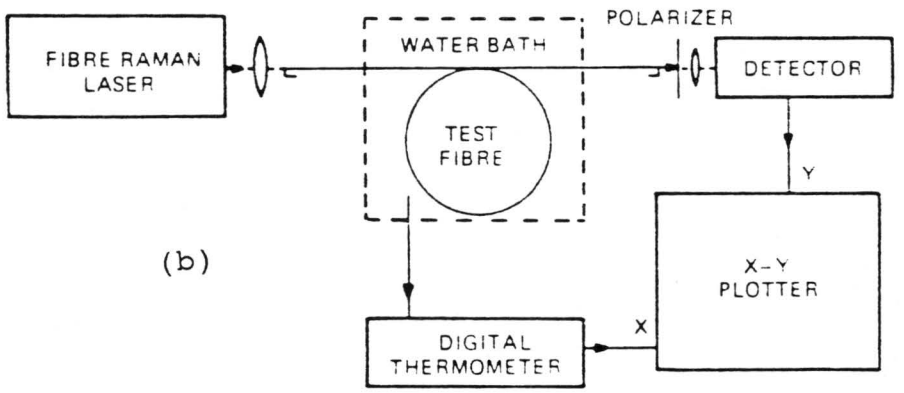

(b)

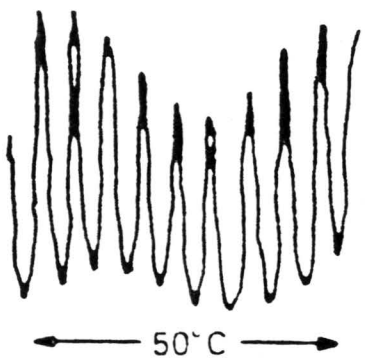

(c)

Figure 2.7: Temperature Sensor Based on Intramodal Interference (after [3])

Because the previously mentioned noise sources are generally low frequency sources, phase sensors are most effective when monitoring processes which occur at moderate to high frequencies.

2.3 POLARIZATION SENSORS

Polarization sensors depend on the fact that some physical phenomena can change the birefringence of an optical fiber [29,30]. The amount of birefringence change is a function of the physical constants of the fiber and of the magnitude of the phenomenon itself. These devices require a polarized light source and polarization-maintaining single mode fibers. The state of polarization of the light in the fiber is altered as the birefringence of the fiber is influenced. A polarization analyzer in series with an ordinary detector monitors the light amplitude, inferring the amount of the modulating phenomenon.

An early example of a polarization-based sensor was demonstrated at NRL in the form of a single mode fiber wrapped around a compliant cylinder [31]. Tension in the fiber varied with the intensity of an acoustic wave deforming the cylinder, and the varying tension induced varying amounts of birefringence. In a more fundamental experiment, the birefringence of a straight piece of fiber was shown to change noticeably when subject to a high frequency ultrasonic wave [4]. This could be used to measure both the frequency and the intensity of the disturbing acoustic wave.

The electro-optic effect of certain transparent crystals has also been used in polarization sensors. Scientists at

Sumitomo Electric Industries in Japan have shown that circularly polarized light impinging on a bismuth silicone oxide single crystal can be changed to elliptically polarized light in response to an ac voltage applied to the crystal [32,33]. Using this principle, a highly linear, noise insensitive, and sturdy sensor was packaged to measure rms voltages in the range of 1 to 1000 V; see Figure 2.8.

Some of the most researched polarization sensors are those employing the Faraday effect, whereby an applied magnetic field induces a change in the fiber birefringence [4]. Although the effect is a weak one, as dictated by the Verdet constant of the fiber, it has been used successfully to measure current flow near the fiber. Efforts to increase the Verdet constant of the fiber by various doping methods have been met with only limited success. In any case, this approach requires special materials and fabrication care, and the theoretical sensitivities of approximately 10^{-4} Gauss per meter are far below those using magnetostrictive coatings.

Because of the limitations in strain-induced birefringence and the Faraday effect, polarization sensors appeared to be losing popularity with respect to other sensing methods. However, two recent developments seem to have reversed, or at least slowed this trend. One development is

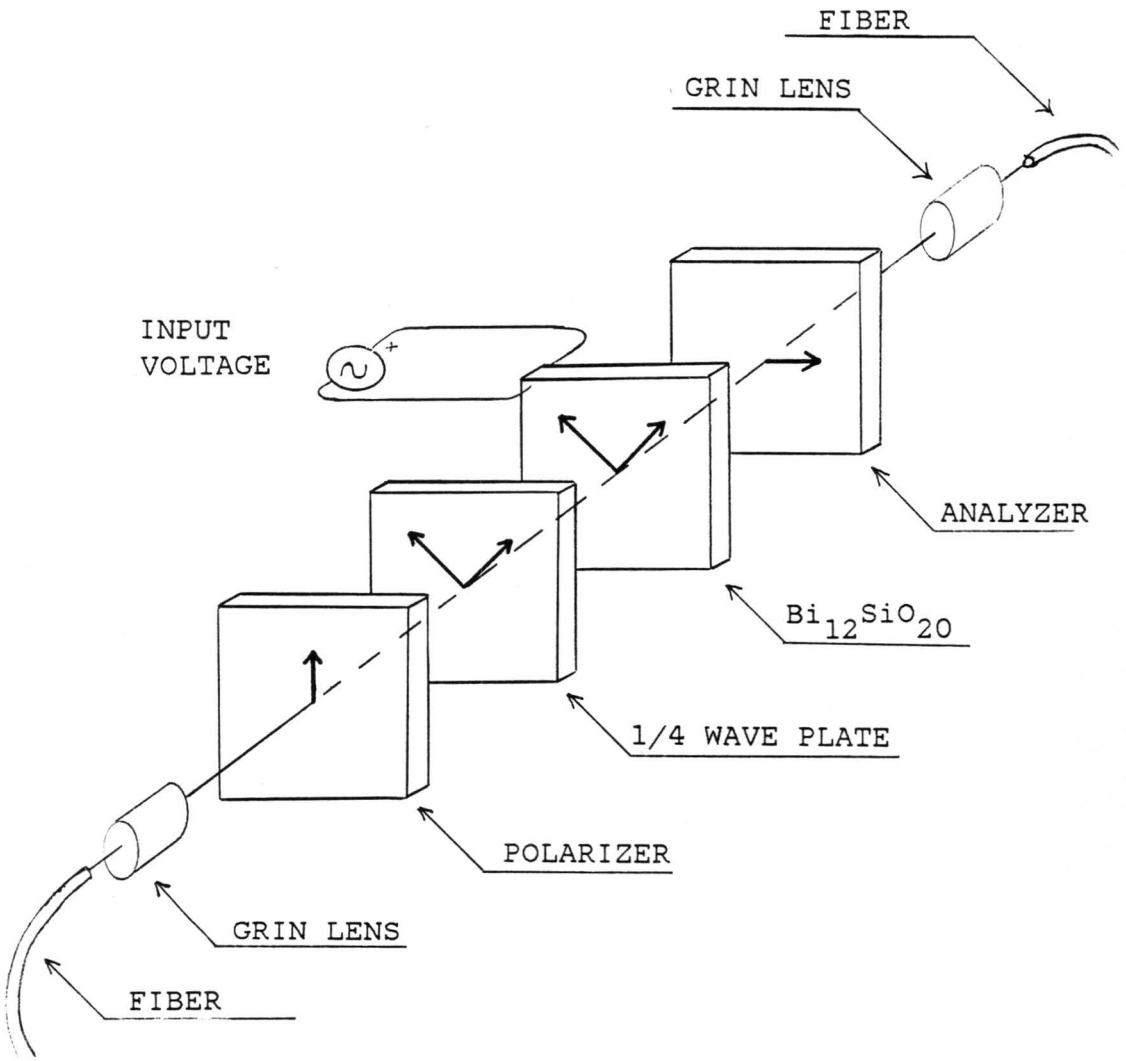

Figure 2.8: Voltage Sensor Using Polarization Changes in Crystals (after [32])

the fabrication of readily available but expensive polarization preserving fibers, made with either elliptical stress cladding or isolated stress regions [34]. With the quality of such fibers increasing and the price gradually decreasing, this necessary tool for precise measurements is more accessible. Already workers in England have tested a dual Fabry-Perot cavity based on highly birefringent single mode fiber [35], and many other similar devices have been designed.

The other advancement for polarization sensors appears in the area of polarization optical time domain reflectometry (POTDR). A POTDR set-up is only slightly more complex than a conventional OTDR, and has the advantage of being able to interrogate polarization-based sensors in single line sensor arrays [3]. This will likely find application where sensing is to be done in several locations remote from the electronic processor.

2.4 WAVELENGTH SENSORS

Sensors which are categorized as being wavelength-based generally result from fiber optic technology combined with spectroscopic techniques. Often the wavelength of light launched into a fiber is determined by a parameter to be measured. At the detecting end, variations in wavelength are converted to amplitude changes through the use of prisms, diffraction gratings, filters, or other differentiating optics. The same detection scheme can also be used when wavelength is the key factor in light that is chemically generated at the sensing end of the fiber.

In a slightly different approach, two or more wavelengths can be made to enter a sensing head and be affected differently by the variable of interest. A sensor using this idea was reported by Inaba, *et al*, with the application of monitoring air pollution [36]. Two wavelengths, λ_a and λ_w, enter a multipass White cell containing the sample gas. These wavelengths are chosen so that one is highly absorbed by a chemical of interest, while the other is virtually unaffected. Bulk optics collect the light emerging from the cell and send it to a spectrometer and a set of detectors. The relative amplitudes of λ_a and λ_w are compared to determine the concentration of the chemical.

In this technique, the optical fibers act solely to conduct light from the electronics to the sensing element. This allows for remote sensing in hazardous conditions. However, as discussed by the authors, the intrinsic absorption of the fiber itself is wavelength dependent, placing limits on both the distance and the spectral range of the device. The latter quantity in turn affects the number of atmospheric contaminants which can be monitored. Figure 2.9 shows the setup used, as well as a comparison of fiber transmission loss with respect to wavelength, and the absorption wavelengths of some common compounds.

As another example, a technique to determine position using a wavelength division multiplexing format is underway at Inland Motor, Radford, Virginia [37]. Radiation from a broadband source enters the sensing head through a fiber, and is color multiplexed by a number of small, rugged interference filters. After interacting with an encoder plate, the light is recollected and sent back to the processing location. There, a set of filters matching the first set act in conjunction with photodetectors to decode the signal. This device will be further discussed in Chapter 4, as well as a related sensor array multiplexing scheme.

In biomedicine, wavelength sensors utilizing the Doppler effect have been constructed [38]. As blood strikes a mem-

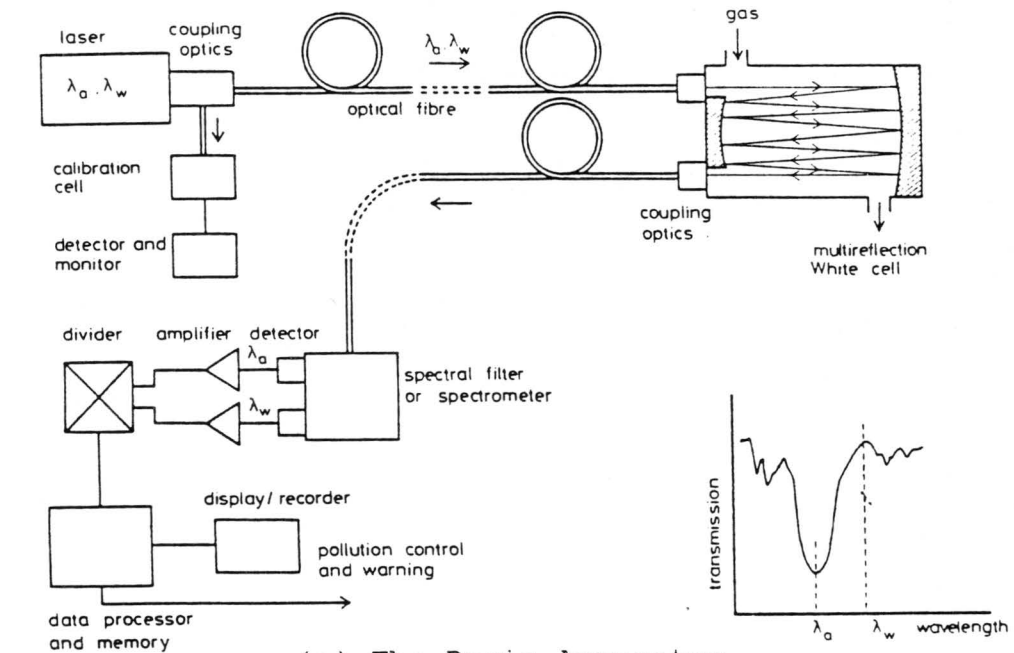

(a) The Basic Apparatus

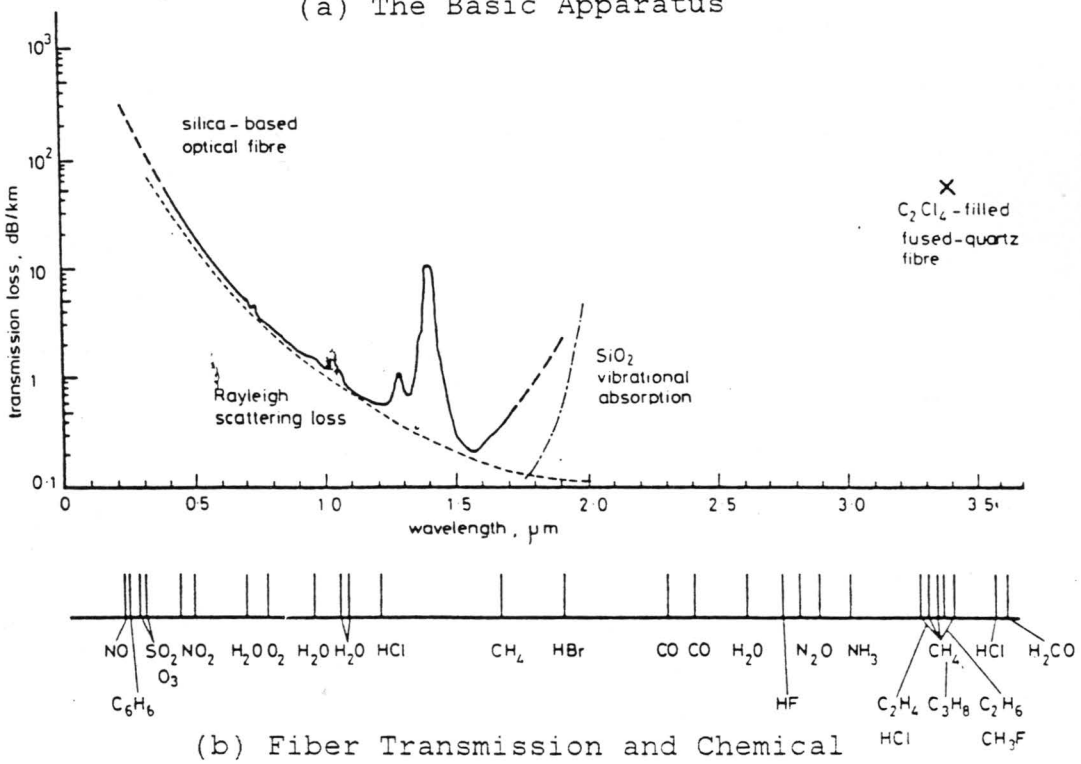

(b) Fiber Transmission and Chemical Absorption versus Wavelength

Figure 2.9: Pollution Monitoring System Based on Wavelength Modulation (after [36])

brane inserted into a vein, light reflected from the membrane is blue-shifted by an amount proportional to the blood velocity. This technique has obvious application to many other velocity measuring situations. However, this sensor has the disadvantage of requiring a highly stable monochromatic light source in order to distinguish signal variations from, say, random thermal fluctuations of the source.

Scientists at the National Physical Laboratory in England have demonstrated a variety of wavelength sensing devices, mostly for use in measuring displacement [39]. Their schemes generally rely on a sensing monochrometer working in reverse: white light is injected into the monochrometer and the displacement to be measured either turns an internal grating (for rotary sensors) or translates a zone plate (for linear sensors). The output wavelength is a function of position, and is resolved by another monochrometer or any other spectrometer, ranging from the eye to a computer-controlled spectrum analyzer. Some of these cases are illustrated in Figure 2.10.

A temperature sensor based on a similar concept was recently developed at Rockwell International [40]. White light launched into one end of a fiber is fed into a Fabry-Perot gap which varies with temperature. With an increase in temperature comes an increase in the gap width and thus

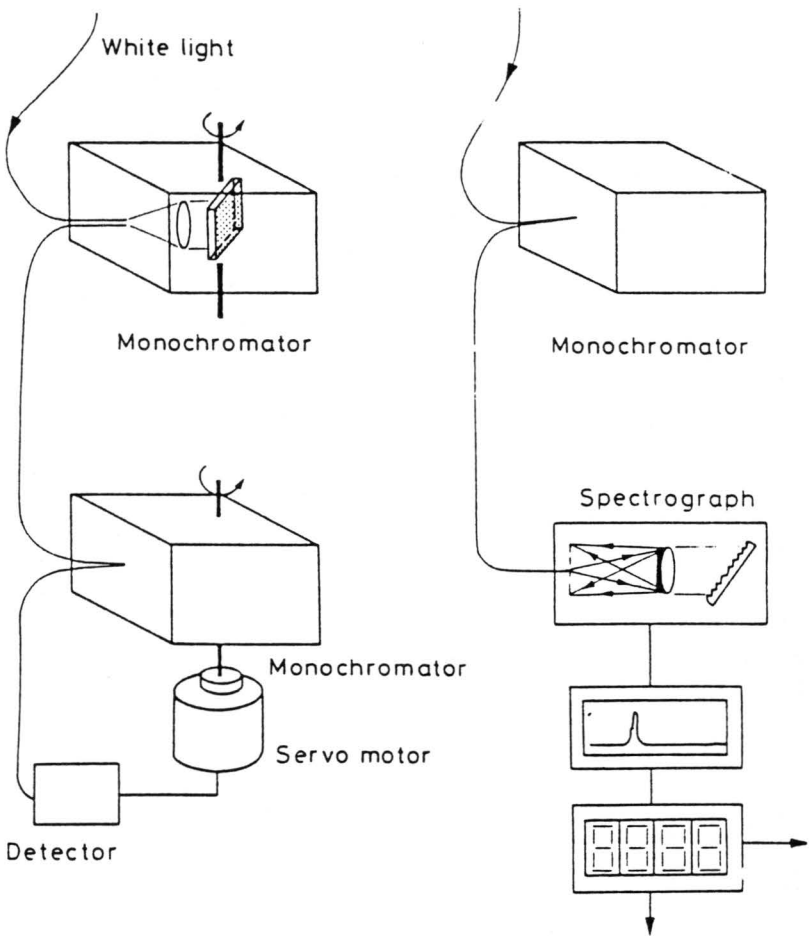

Figure 2.10: Wavelength Encoded Sensors Using Monochrometers (after [39])

an increase in the number of spectral bands passing to the detector. By counting this number of bands one can infer the temperature change. The major disadvantage of this scheme is the ability to measure only relative changes. A knowledge of the beginning temperature is required if absolute temperatures are to be determined.

2.5 MODAL MODULATION SENSORS

The fifth, virtually undeveloped class of sensors rests on the phenomenon known as modal modulation. Because an optical fiber is a waveguide, some propagation modes are supported in the fiber while others are not, depending on the fiber structure. In a multimode fiber, many such modes propagate and interact with each other all along the length of the guide. When these modes emerge from the end of the fiber, they form a complex pseudo-random interference pattern known as a speckle pattern. It consists of hundreds of areas of varying intensity depending on the modal behavior and thus on the exact fiber geometry and local refractive index profile. Monitoring the intensity of any one speckle is then a measure of any process which changes these parameters. As with other sensitive measuring techniques, however, noise problems arise due to random environmental variations.

Early work done at NRL hinted at this idea when interference was performed between modes in a multimode fiber [26]. From that time however, emphasis has been placed on decreasing the number of modes to two, and detecting differential phase changes, as mentioned earlier. A few efforts have continued using the multimode fiber speckle concept, notably at the University College in London [41]. There, Culshaw *et*

al, correlated strain, pressure, and temperature changes with single speckle intensities; their method is called Fiberdyne. Other sensors, intended to measure current and temperature have been described, as well as one specifically geared towards acoustic wave monitoring [42,43]. However, interest in this method of sensing seems to be low, presumably due to insensitivity with respect to conventional interferometric techniques.

Chapter III

OTDR TECHNIQUES IN COMPOSITES

Materials engineers have ever pursued the fabrication of strong but light materials. Demands for their use appear in a broad spectrum of human activity, ranging from recreation to tooling to weaponry. Recently developed laminated fiber reinforced composite materials have been made to meet a great many of these demands.

The merits of such composite materials are now well established. They include high strength-to-weight ratios, stiffness-to-weight ratios and high corrosion resistance. As structural members they reduce parts counts and display increased longevity over high technology metals, making them attractive from a financial point of view. Furthermore, the constituents of such composites are created from abundant materials, as opposed to aluminum or titanium, for example. Finally, the dielectric nature of composites offers advantages considered paramount in importance for certain applications, such as offering low radar cross-sections.

Naturally, the ubiquity of composite materials calls for a variety of means to test them. Previous optical fiber measurements have included both destructive and nondestructive tests. Crane, for example, imbedded two-dimensional

grid arrays of similar multimode fibers and used the interruption of transmitted light caused by internal fiber breakage to indicate regions of excessive local strain [44,45]. Since in the future it may be more economical to replace rather than repair large composite parts, such a sensor array may provide all the materials evaluation information that is needed in many applications.

In an effort to obtain quantitative information concerning material loading, Meltz and Dunphy demonstrated excellent sensitivity to subsurface strains and stresses within orthotropic plates and symmetric cross-ply laminates [46]. They have used twin core fibers to measure differential changes in core cross-talk, as well as polarization-maintaining fibers to interferometrically monitor stress-induced birefringence. Additionally, Claus and Wade implemented imbedded single mode fiber grid arrays and multiple channel Mach-Zehnder instrumentation to obtain good spatial sensitivity to static strain distributions in small composite coupons [47,48].

The vision behind the present research entails a nondestructive evaluation technique (NDE) which is both repeatable and sensitive, and with which real-time analysis can be performed. Although several NDE methods currently exist, such as ultrasonic measurement, x-ray analysis, acoustic emission

sensing, vibrothermography, and Moire analysis, none are well suited to dynamic measurements.

In 1982 the Virginia Tech Acousto-Optics Group proposed a strain measurement system to meet the desired goal. It relies on the use of optical fiber imbedded in the composite material, and employs optical time-domain reflectometry (OTDR) as the sensing technique. In 1984 a preliminary study of the system was conducted, culminating in a Master's Thesis by group member B.S. Jackson [49]. The study contained a theoretical analysis of OTDR, especially as applied to imbedded optical fibers, as well as a detailed description of laminated reinforced composite plates. It also included the testing of a sample containing an optical fiber, the description of a computer model to simulate OTDR, and a comprehensive set of references on OTDR and related techniques.

Jackson's work resulted in full justification of continuing investigation into the proposed system. This chapter rests on that foundation, and uses it as a springboard for further research. Although mentions of the previous work will appear where appropriate, no effort will be made to reiterate what has been said before.

This chapter presents first a review of the OTDR method, the meaning of the backscattered signal and its analysis,

its theoretical and practical limitations, and its advantages and possible applications. A short summary of prior work follows, and resulting problematic questions are identified. Both the rational for and the results of tests designed to answer those questions are the subject of the next sections. A modified OTDR computer simulation is then presented, as well as a signal processing program and a discussion of its usefulness. The chapter concludes with suggestions for future work, both near and far term.

3.1 OTDR CONCEPTS

OTDR is conventionally used in optical fibers to characterize propagation properties such as attenuation or as a fault location technique. Ideally an optical pulse approaching zero width (an impulse) is launched into one end of a fiber. At each point within the fiber, material atoms scatter light in all directions. Most continue as a forward travelling wave; a small percentage is backscattered within the numerical aperture of the fiber. Because of these Rayleigh scatterers, the intensity of the forward travelling wave continually decreases, allowing for less and less light to be backscattered. Figure 3.1 shows a typical backscattered signal, including its various attenuation regions, while Figure 3.2 shows the simplified arrangement used to generate such a signal.

Theoretically, the backscattered intensity in homogeneous fibers can be shown to experience an exponential decrease with respect to time [50]. When the intensity is plotted on a natural logarithmic scale, a straight line results. The slope of the line can be correlated to the attenuation of the fiber in terms of dB per kilometer. A sharp slope indicates the presence of many scatterers in a given distance, so that the forward traveling wave is attenuated rather quickly. It should be noted, however, that the attenuation

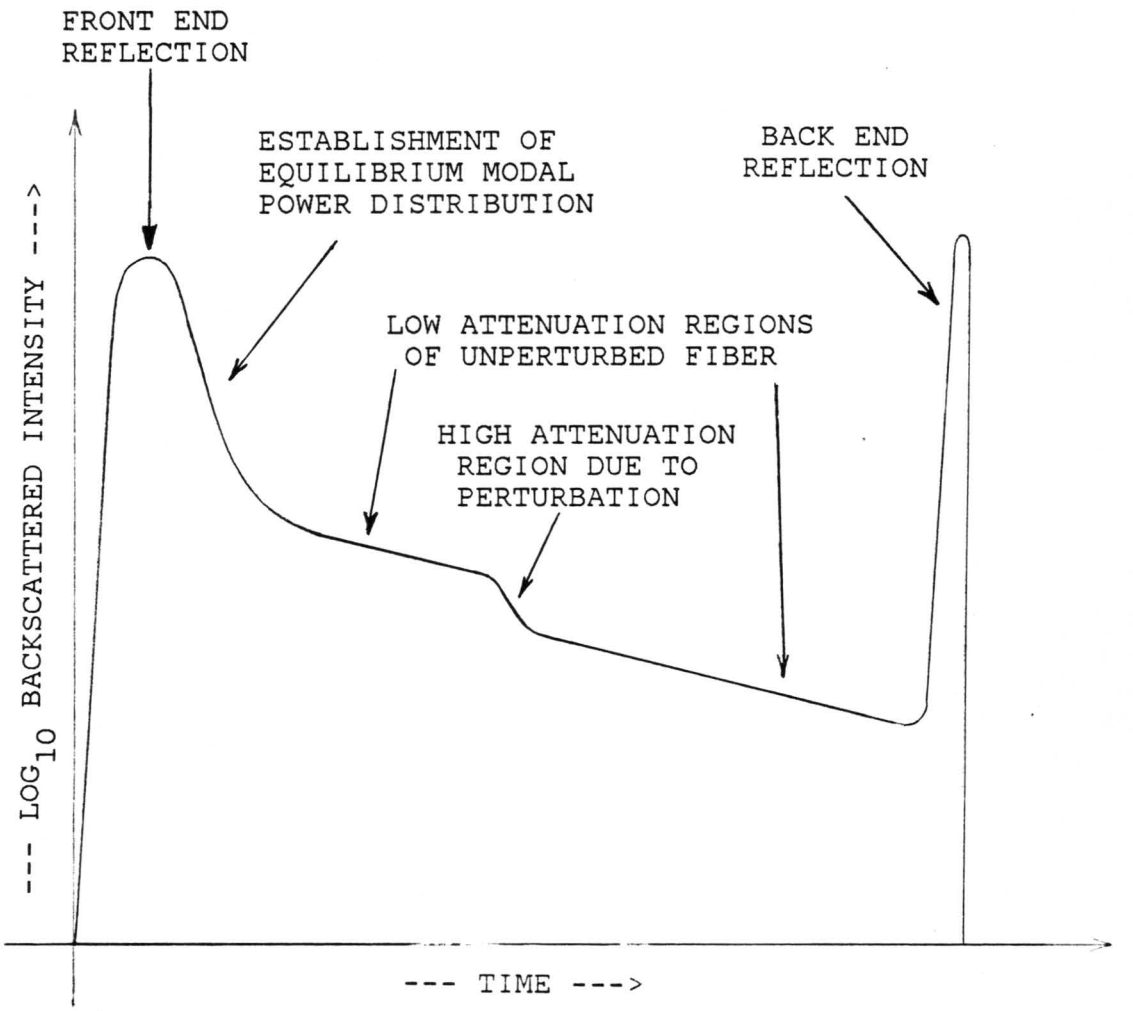

Figure 3.1: Standard OTDR Signature

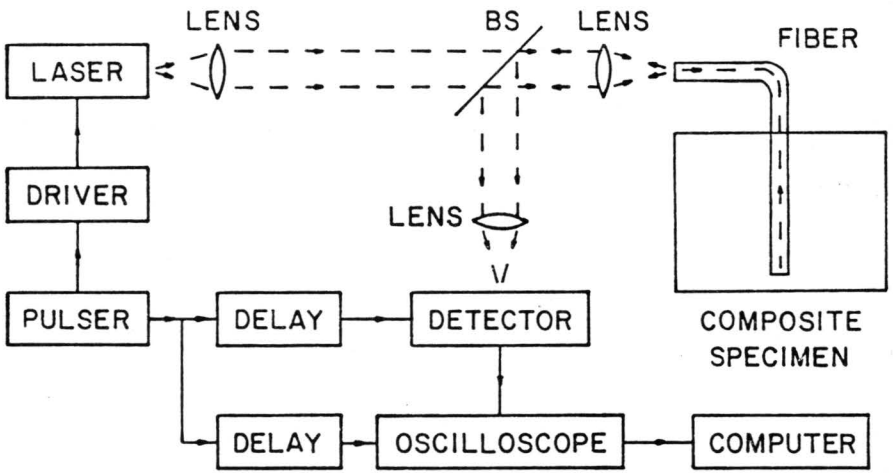

Figure 3.2: Basic OTDR System

due to Rayleigh scattering is highly dependent on the source wavelength, λ, as seen in the relationship

$$I_R \propto 1/\lambda^4 \tag{3.1}$$

where I_R is the Rayleigh scattered intensity [51].

If the far end of the fiber is cleaved flat, then light internal to the fiber will experience the normal 4% reflection at the glass-air interface. This is actually quite large with respect to the Rayleigh backscatter. Furthermore, if the group velocity, v_g, of the optical pulse in the fiber is known, the length L of the fiber can be obtained from the roundtrip transit time t of the optical pulse. That is,

$$L = v_g t/2 \tag{3.2}$$

where v_g is easily determined from the refractive index n of the fiber, and the speed of light in a vacuum, c,

$$v_g = c/n \tag{3.3}$$

For most calculations, n is considered as approximately 1.5 (actually it is usually around 1.458), making $v_g \approx 2 \times 10^8$ m/sec. The large end reflection can also be seen in Figure &otdrf..

For various reasons, cracks or outright breaks sometimes occur in fiber lengths. These faults generally transmit a small portion of light, scattering the rest. In essence, they act as regions having a very high local attenuation.

Consequently, the OTDR signature shows a drastic change in slope at a time corresponding to the location of the damage. This principle is used to advantage in field operations calling for the isolation and repair of cable faults.

Besides the fiber end, cracks, and breaks, other perturbations in the fiber homogeneity exist due to impurity atoms. Although they are not uniformly distributed in the fiber core, their presence acts to increase the average attenuation. Although this type of scattering loss limited the range of early fiber optic transmission, fabrication techniques are now capable of producing extremely pure preforms. In addition, fiber drawing processes have been refined to the point that inhomogeneities due to intrinsic local refractive index changes (which themselves act as light scatterers), have been nearly eliminated. Finally, although some light is actually absorbed by the medium, choice of the proper fiber core dopants and emission wavelength render this loss as small compared to other loss mechanisms. Thus the attenuation of advanced fiber is approaching the theoretical minimum [52].

When stress is applied to an optical fiber, areas of local index changes result. This, as well as light losses due to microbending give rise to concentrated regions of high attenuation. As mentioned before, slope variations in the

backscattered signal locate these regions, and therefore the applied stress. Furthermore, although calibration problems exist, it can be said that small stresses lead to small slope changes, while large stresses lead to large slope changes.

The spatial resolution of a practical OTDR system depends primarily on the pulse width of the optical probe, the photodetector rise time, and the pulse dispersion characteristics of the fiber. For the lengths and types of fiber generally used, the latter factor can usually be neglected. In this case the spatial resolution limit can be expressed as

$$\Delta l \approx (t_p + t_d)v_g/2 \tag{3.4}$$

where t_p is the pulse width and t_d is the detector response time [50]. Since generally $t_d >> t_p$, (3.4) is conventionally reduced to

$$\Delta l \approx t_d v_g/2 \tag{3.5}$$

As will be shown, this resolution limit was successfully confirmed by actual measurements.

3.2 OTDR IN IMBEDDED FIBERS

From the previous discussion, we conclude that to within limits, the location and amplitude of stresses applied to optical fibers can be determined using OTDR. This concept was partially demonstrated by McMillan and Robertson [3], whereby a remote microbend sensor such as in Figure 2.4 was monitored with an OTDR system. As Figure 3.3 shows, their results concentrate on the pressure calibration of the sensor. In a later paper, Marvin and Ives report the distribution of three such sensors in series along a single fiber [12]. Their work features the use of both deconvolution and background subtraction schemes for proper data interpretation. However, in neither case were the authors particularly concerned with the precise location of the strain, since discrete sensors were being used.

In the present research, a continuous length of optical fiber imbedded in a composite plate is envisioned as a distributed strain sensor. Due to both the periodic graphite fiber bundle structure within the composite, and the matrix flow properties, the imbedded fiber is inherently subject to some microbending. The geometry of this microbending depends in part on the periodicity of the fiber bundles, and thus on the orientation of the optical fiber with respect to the ply layers which contain it. Moreover, the degree of

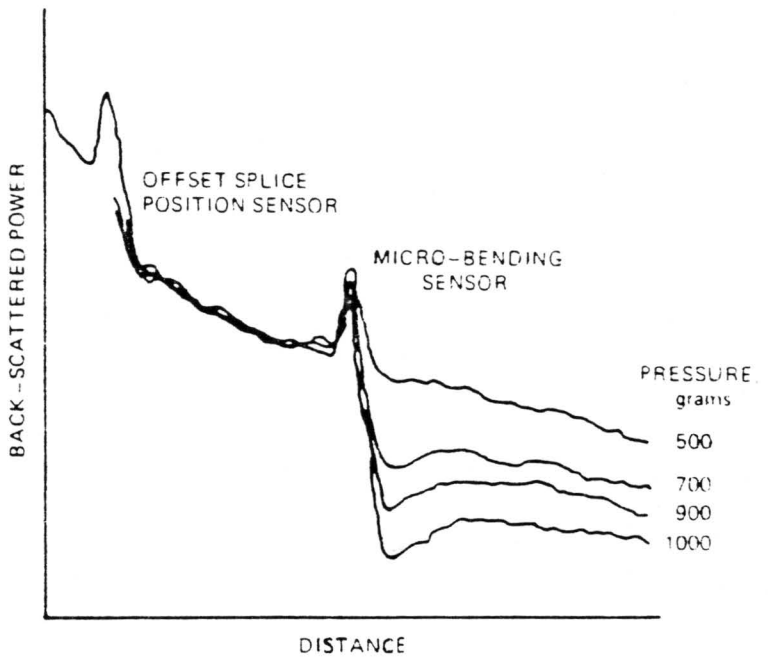

Figure 3.3: OTDR Signature of a Remote Microbend Sensor (after [3])

microbending rests on the size and mechanical compliance of the optical fiber, the degree to which the fiber contacts the composite plys, and finally on the external load applied to the composite itself. The amount which each of these factors contribute to total fiber attenuation is unknown at present, but would certainly vary from sample to sample.

Many advantages accrue to the continuous sensor. If the first derivative of the OTDR signature is performed, the magnitude of the slope at various points becomes evident. The second derivative further enhances changes in the slope. Together these give information concerning the stress at any point along the fiber, again, to within the resolution limits.

Because of the composition of fiber optics, the all-dielectric nature of the composite can be maintained with this sensor. Further, dynamic strain measurements are possible with this system, depending largely on the capabilities of the processing electronics. Together with a knowledge of the layout of the fiber within the composite specimen, these advantages suggest the possibility of obtaining a dynamic, three-dimensional strain map of the specimen, similar to a topographical map. The applications of such a powerful measurement tool would be boundless, ranging from monitoring of composite lay-up and curing processes, to strain monitoring of panels installed in aircraft wings.

In view of the foregoing, imbedded optical fiber sensors certainly deserve investigation; however, some caution should be exercised. First, while the system is theoretically capable of making real-time measurements, limitations in the data acquisition timing thwart this somewhat. For example, the system used in this work was limited to approximately one strain measurement every two seconds [53]. This was due in part to the digital averaging of many individual waveforms needed to improve output SNR. In addition, further signal processing such as taking derivatives and making layout/strain correlations would significantly impact the overall dynamic measurement ability.

Second, the effect of continuous microbending on modal power distribution is unclear. When light is injected into a fiber, power is not generally distributed evenly among the modes. It has been shown however, that for distances

$$z > 1/\gamma_1 \tag{3.6}$$

in a straight fiber, where γ_1 is the attenuation coefficient of the lowest order mode, mode mixing occurs so that an even power distribution can be assumed [54].

As mentioned previously, high order modes are more susceptible to bending loss than are low order modes. Also, as pointed out by Marcuse, even nearly imperceptible bends and bumps can cause significant mode coupling and mode conver-

sion [55,56]. Thus, while calibration assuming even distribution may be valid for the first bend, subsequent bends violate the assumption. Some high mode power is lost due to the bend, and some low mode power is transferred to high modes.

To assume that these latter two effects offset one another in a waveguide supporting hundreds or even thousands of modes, thus instantly creating modal equilibrium, is at best precipitous and unconfirmed. In fact, the net result of such bending is an unpredictable scrambling of the modal distribution. If a guess were to be ventured however, it is likely that more higher mode power was lost than replaced. This could cause the second bend to appear less severe than it would have if modal equilibrium had existed prior to it. This concern is confirmed by Marvin and Ives' emphasis on the need for proper background (previous signal) subtraction.

3.3 OPTICAL MEASUREMENTS

As a first attempt towards the realization of a composite strain sensor using OTDR, Jackson imbedded a jacketed, graded index fiber between two plys of a 30 cm square composite panel. An ultrasonic C-scan of the panel, seen in Figure 3.4 shows the serpentine fiber lay-up pattern used to maximize the amount of fiber within the panel. Except at the bends near the edges, the optical fiber lay parallel to the graphite fibers in the adjacent plys, as seen in Figure 3.5.

Static measurements of the fiber's sensitivity to mechanical loading was performed using the set up shown in Figure 3.6. Figure 3.7 displays the optical signal transmitted through the fiber as a function of time, in response to loading the sample with an 8.2 kg weight with a circular contact area one cm in diameter. The points marked "A" in the figure represent the time the weight was placed on the composite, while those marked "B" delineate its removal.

The upper trace shows the response obtained by placing the weight near the edge of the panel. Clearly the attenuation of the imbedded fiber has increased due to the mechanical load. The lower two traces were obtained by placing the weight near the center of the composite. In one case the local attenuation has increased, while in the other it has apparently decreased. As suggested by Jackson, the latter

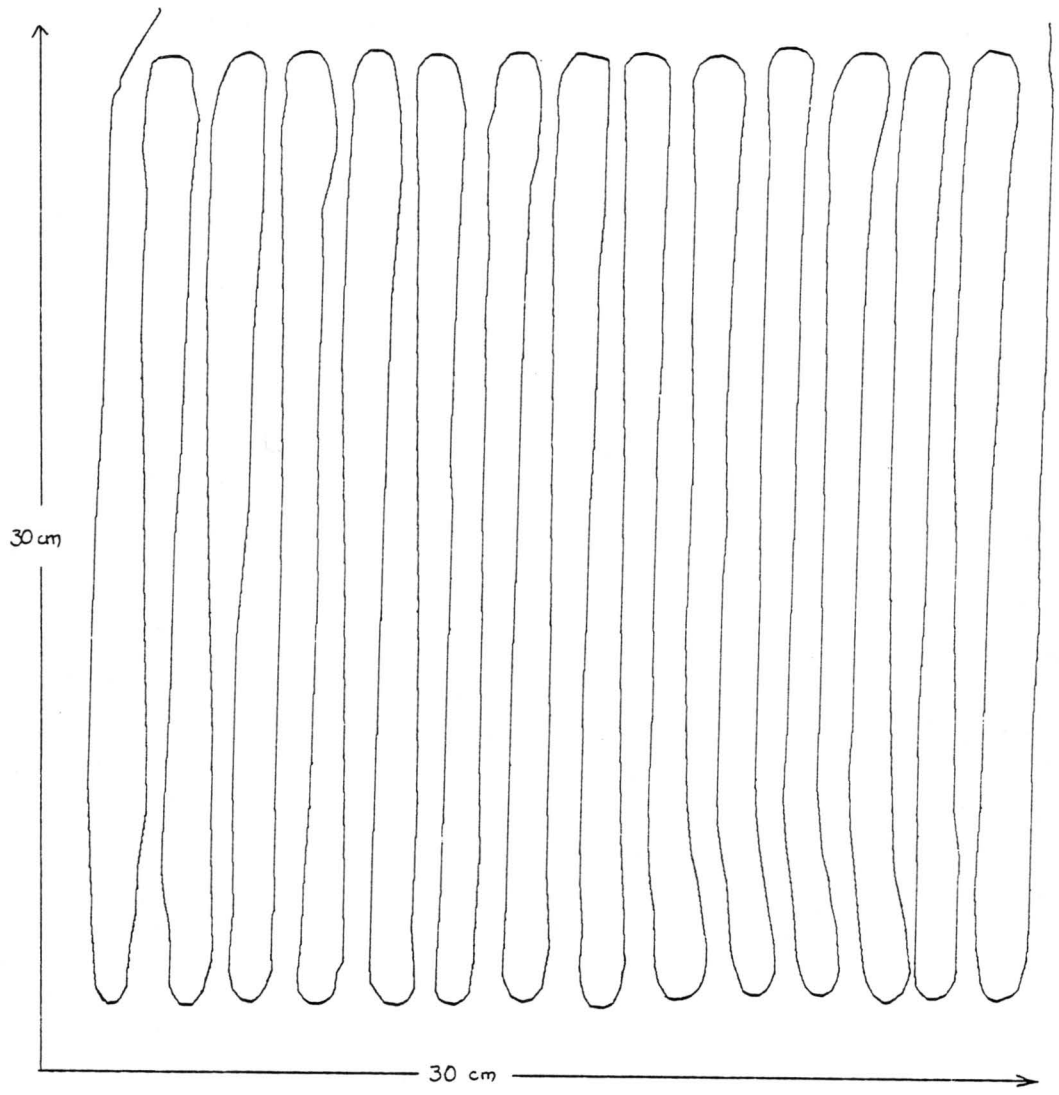

Figure 3.4: Enhanced C-Scan of Imbedded Optical Fiber Layout (after [49])

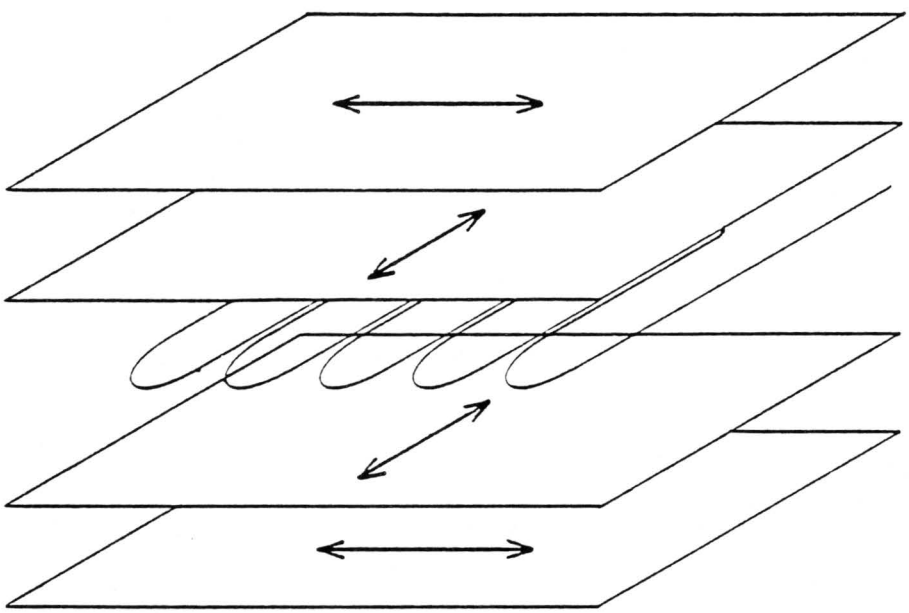

Arrows indicate direction of
fiber axes in composite material.

Figure 3.5: Orientation of Optical and Composite Fibers (after [49])

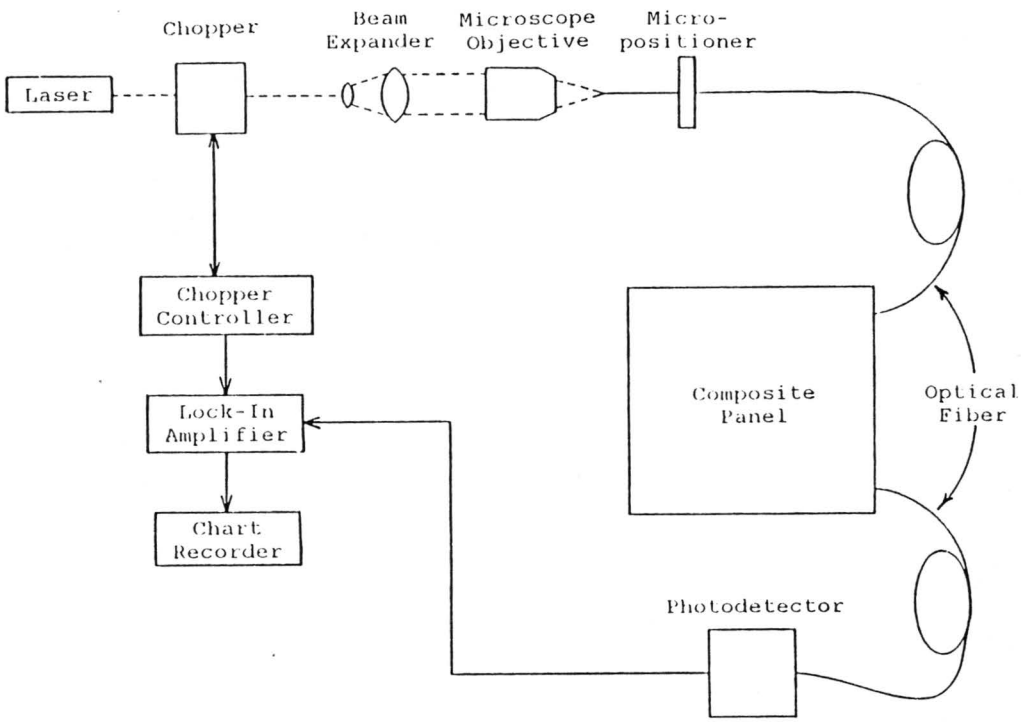

Figure 3.6: Setup for Measuring Loss in Imbedded Fiber (after [49])

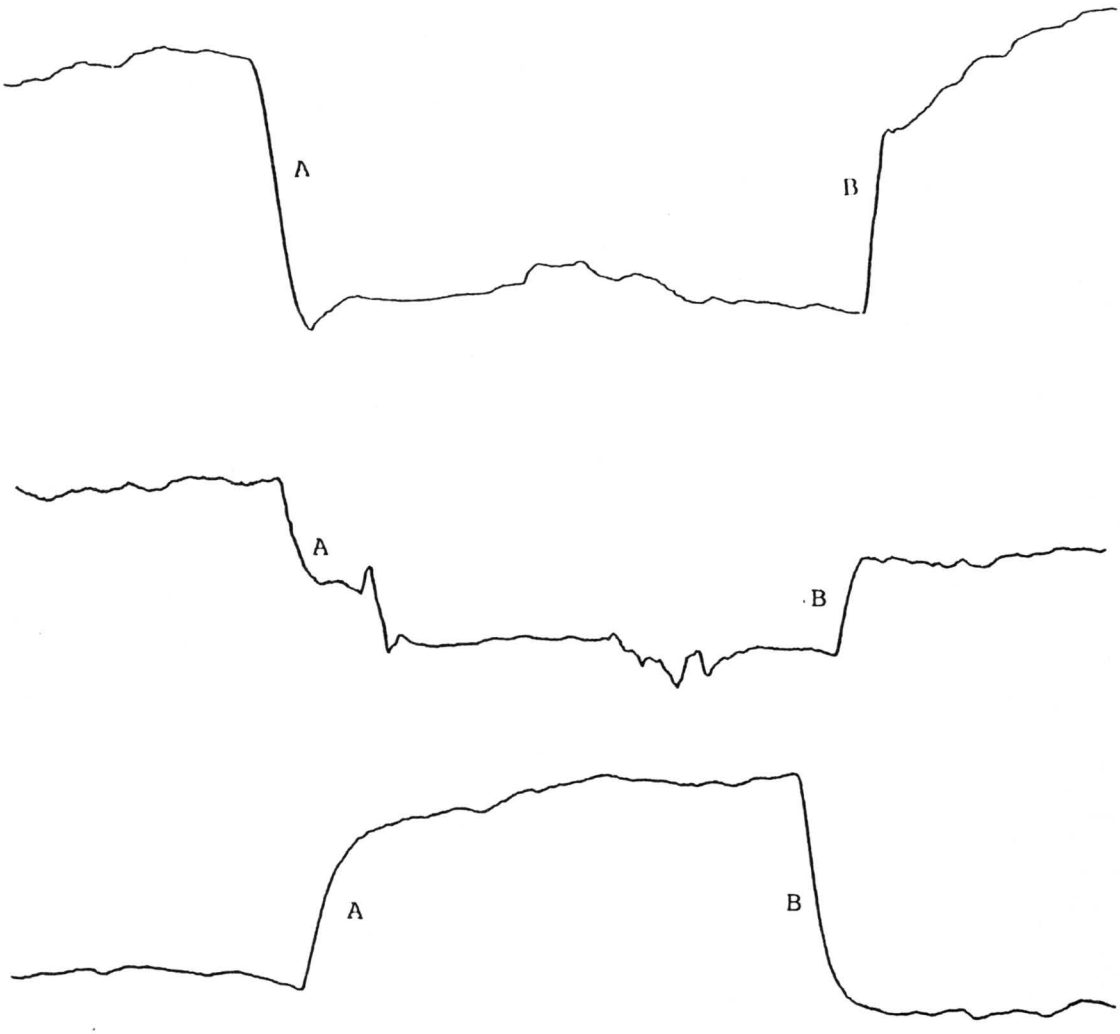

Figure 3.7: Signal Produced by Weight on Composite (after [49])

case is presumably due to either the mass straightening out a kink induced by the composite, or a change in fiber geometry which couples cladding modes back into the core. It is mentioned here to further demonstrate the need for care when trying to correlate electronic signal levels with load-induced strain.

Next, OTDR measurements were performed on the sample. The backscattered slope revealed a low attenuation of roughly 4 dB/km for the fiber portions on either side of the composite, while the ten meters of imbedded fiber experienced a high attenuation of about 1 dB per meter. When the panel was clamped with a C-clamp along the first straight portion of fiber, a significant slope change occurred, indicating an increased overall attenuation. Figure 3.8 shows the OTDR signal returned from the imbedded portion for both the unloaded and loaded cases. When the clamp was moved further along the fiber, the slope change also moved, as expected. This can be seen in Figure 3.9.

Recently, further optical measurements were carried out on the same composite/fiber sample to confirm previous results. Due to the spatial resolution limitation cited earlier, mechanical loading was performed by clamping 16 cm long rectangular solid bars of aluminum above and below straight sections of the imbedded fiber in such a way that

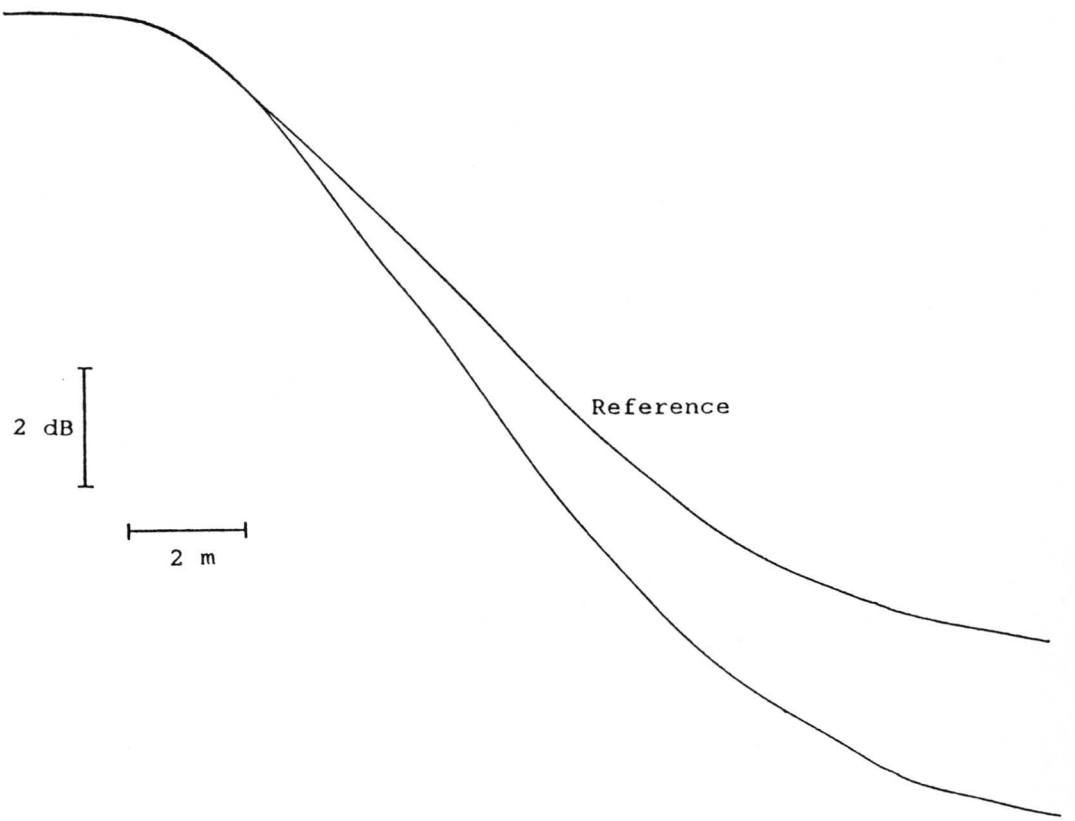

Figure 3.8: OTDR Signal from Weighted Imbedded Fiber (after [49])

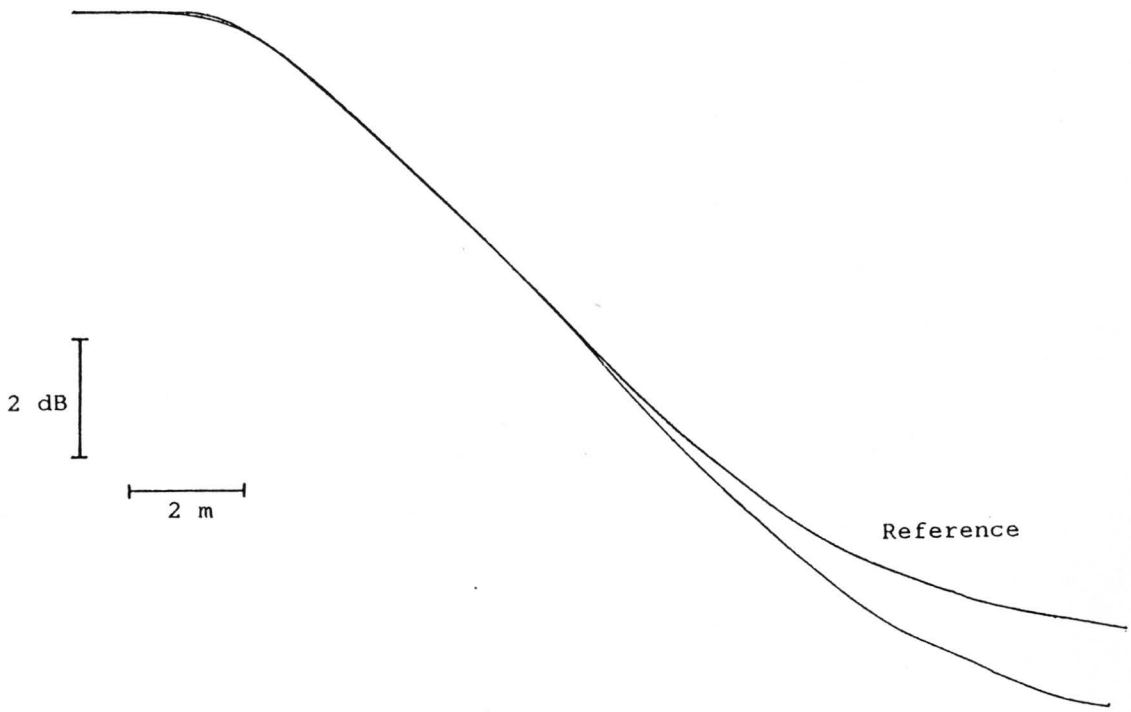

Figure 3.9: OTDR Signal from Fiber Weighted in Center (after [49])

the internal load was approximately 350 kPa and uniform along the bars. The OTDR signature obtained for this type of loading is shown in Figure 3.10a. SNR was improved here by digitally averaging 250 individual waveforms per trace.

Next, the specimen was loaded with three similar bars on which different pressures were exerted. The relative locations of the separate loads may be observed from Figure 3.10b. In addition, the relative difference in the signals resulting from the three separate loads of 350, 700, and 1050 kPa is easily discernible.

By reducing the spacing between adjacent loading points and observing the local excess attenuation regions approach each other on the OTDR output, a practical linear spatial resolution of somewhat over 18 cm was determined. For the system used, the optical pulse width t_p was 245 psec, while the detector response time t_d was 1.6 nsec. Resolution measurements were then in excellent agreement with Equation (3.4), which predicts a limitation of 18.45 cm.

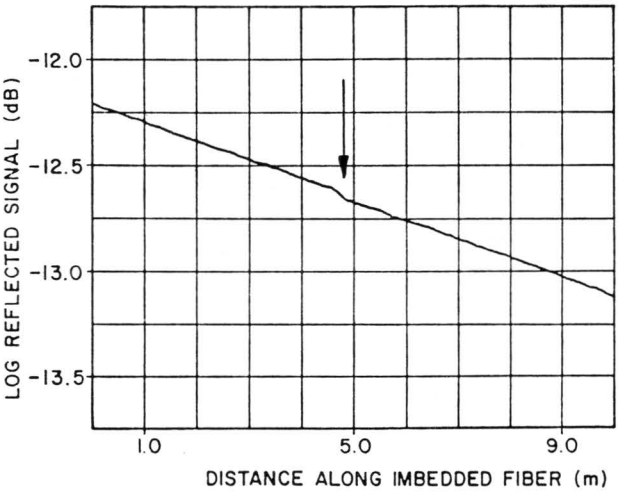

(a)

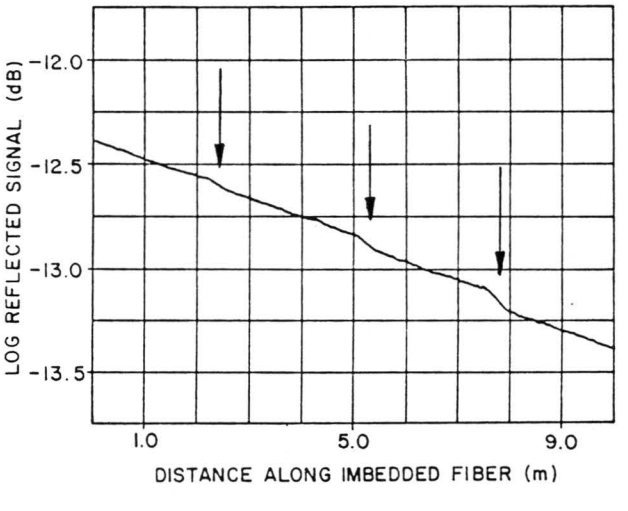

(b)

Figure 3.10: OTDR Signal Obtained for Loaded Composite Specimen

3.4 MECHANICAL CONSIDERATIONS

The optical measurements give confidence that imbedded optical fibers do offer promise as a means for measuring strain in composites. However, nothing has been said thus far about the strain sensitivity of the imbedded fiber, nor has there been any discussion of how the fiber affects the integrity of the host composite. These factors must be realistically evaluated if the usefulness of this sensing concept is to be established.

3.4.1 Mechanical Sensitivity

As discussed in Section 3.2, it has been assumed that the imbedded fiber will act as an integrated microbend sensor. Even with no loading on the composite sample, the fiber should undergo some microbending due to its interaction with the graphite fiber tows, and thus experience a higher attenuation than non-imbedded fiber. Loading the specimen would then cause bulk strain, which should be transferred to the fiber through the laminated plys. The additional force is then noticeable through further attenuation.

As mentioned, the portion of fiber imbedded in the panel does indeed show a higher attenuation than normal, even with the sample unloaded. It may be naive however to assume that this is only due to interaction with the tows. One reason

is that although the composite fibers start out in discrete bundles (tows), during the pre-preg formation they are pressed into a nearly uniform density [57]. This is illustrated in Figure 3.11. Thus, if the optical fiber is laid across the composite fibers and is in intimate contact with them, the greatest bending amplitude it can experience is on the order of a graphite fiber radius. When one considers that this radius of 5 to 15 microns is roughly an order of magnitude smaller than that of the typical unjacketed optical fiber, and nearly two smaller than a jacketed fiber [58], it is unlikely that this would cause significant bending.

The bending periodicity is also of extreme importance to the loss characteristics. Formulation and data presented in Section 4.1 show that when optical power loss is plotted against the spatial deformation period, a strong peak occurs at periods of a few millimeters, depending on the exact fiber used. The loss occurring at periods typically presented by the composite fibers is generally very low.

Another consideration in discussing the high attenuation of the imbedded fiber has to do with the degree of contact between it and the composite fibers. First of all, in the fabricated specimen, the polymer buffer remained on the fiber. Generally a jacket is applied to an optical fiber in

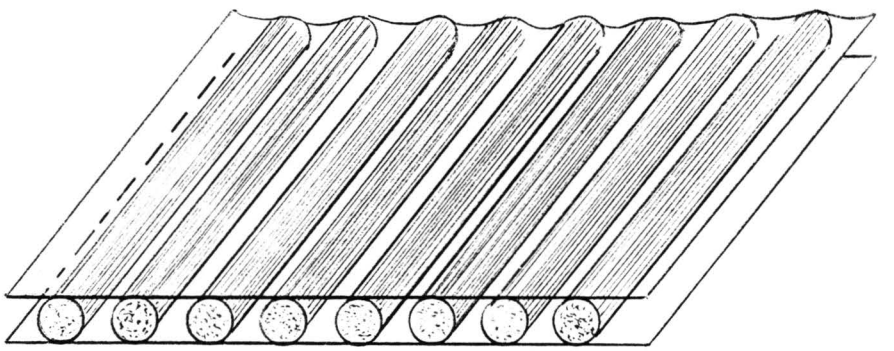

(a) fiber tows are coated with resin and aligned between two sheets of siliconized paper.

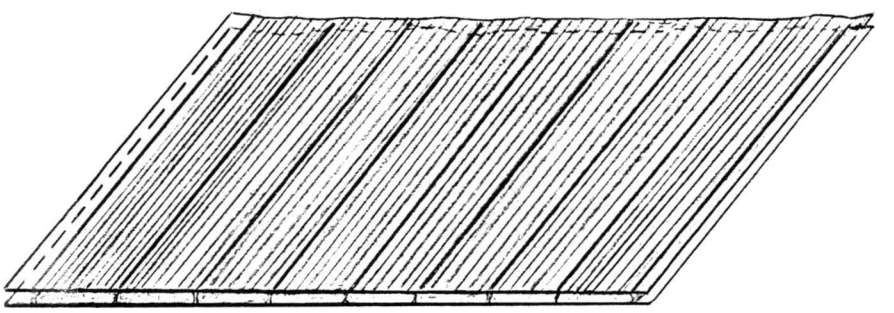

(b) tows are rolled between sheets -- alignment is preserved and trapped air is removed.

Figure 3.11: Making of a Pre-Preg Sheet(after [57])

order to reduce the coupling between external mechanical effects and the light guiding core. Obviously that property is undesirable in this case. Also, although the coating shows some yellowing due to the 350°F heat applied to cure the panel, it appears to be relatively intact. Thus the jacket acts to increase the effective fiber diameter, allowing for even less bending in small periods.

Secondly, the contact between the optical fiber and the graphite fibers is impeded by the matrix material. Not only are the fiber tows laminated in the epoxy resin, the individual plys (pre-pregs) are glued together with it. Thus, before curing, the optical fiber may be considered to be partially surrounded by a low modulus material, and is therefore unlikely to be easily perturbed. However, the panel is generally cured under pressure, in this case 588 kPa (85 psi). The degree to which the optical and composite fibers were forced into contact is not clear. It is suspected however, that since the epoxy remained in the panel, the contact is not as intimate as desired.

Finally, as noted before, the optical fibers and the graphite fibers actually run parallel in most of the sample. Thus, the entire discussion of whether or not the optical fiber follows a sinusoidal bend (as in Figure 2.4), while instructive, is somewhat superfluous. Of course some fiber

crossings are expected; they are not all exactly perpendicular along their entire length. Also, the two types of fiber do cross significantly at the edges, where the optical fiber reverses direction. Nevertheless, the combined effect of these types of crossings is considered insignificant, though more data is needed in order to reach a firm conclusion.

The question still remains then as to the cause of the high attenuation exhibited by the imbedded fiber. One explanation is that the fiber experiences significant loss at the large curves near the edges. To test this theory, a similar piece of fiber was laid on a flat board in the same geometry as the imbedded fiber. While it was true that light was quite visible at the hairpin turns, the actual intensity varied little when the bends were carefully released, one at a time. Since the fiber was not mode stripped at the bends, coupling between core and cladding modes is permitted, presenting a complicated, as of yet unpredictable situation. Also, the amount of loss introduced by a given bend has been observed to be highly dependent on precisely how the light was launched into the fiber. Thus, though the claim above may be true, it is at best difficult to substantiate with repeatable data.

It is suggested that a large contribution to the observed fiber attenuation arises from small but severe bends caused

by irregularities in the fiber-resin interface. Although the addition of extra resin along the optical fiber during lay-up reduces voids between the fiber and the matrix [53], this extra resin was not applied to the specimen under discussion. Before the panel was cured therefore, some voids undoubtedly existed. This is confirmed in that the non-enhanced ultrasonic C-scan of the imbedded panel outlined the fiber, indicating a significant boundary existed between the fiber and the host material. This is especially noticeable near the direction reversals, where the effect is expected to be even greater.

When heat and pressure were applied, bends of smaller radius than those due to iteration with the tows or due to the direction reversals would likely have been created. This type of curvature would correspond to the bending easily induced by the low pressures. This has often been observed to cause through-put intensity decreases ranging up to 15 dB [59]. A combination of only a few such bends, while not regularly spaced (therefore not of the "optimum" deformation period), could be responsible for significant loss.

Another factor contributing to the mechanical sensitivity is the mechanical and adhesive properties of the fiber jacket, since the strain transfer from the material to the optical fiber depends on these. Although much work has been done

to identify jacketing materials having elastic constants which enhance fiber pressure sensitivity, little work has been done in this area to determine trade-off between such enhancement and the effect of the jacket on the overall mechanical properties of the composite. Preliminary analysis by Crane suggests only that a fiber coating of resin similar to that used as matrix has acceptable mechanical properties [45]. Dunphy and Meltz have shown that this type of coating also provides maximum bonding between the optical fibers and the surrounding composite structure [60].

Finally, how the fiber jacket is affected by the curing process is still unknown to us. It has been suggested that under heat and pressure, the elastomer simply melts into the surrounding resin. This would probably be favorable, since it would increase strain transfer and microbending possibilities. Also since stress concentrates around discontinuities, a smaller effective fiber size would probably add to the overall mechanical stability of the panel.

In view of the small bending radii required to observe microbending loss, as well as the fact that the imbedded fiber was jacketed, it is not surprising that significant pressures had to be applied in order to observe additional fiber attenuation (such as observed from Figure 3.8 and 3.10). However, it is presently too early to draw final

conclusions about the mechanical sensitivity obtainable with imbedded fibers. Much more research is required to sort out the ambiguities noted above.

3.4.2 Mechanical Integrity

Exactly how an imbedded optical fiber affects the structural integrity of a composite sample is unclear, but is certainly of great concern. As mentioned, voids between the fiber jacket and the matrix are known to occur if care is not exercised. Some composite engineers purport that these voids, or even the presence of extra resin added to alleviate them, greatly increase the risk of delamination [61]. Of course if the sensor were to thus compromise the mechanical properties of the sample the viability of the technique would be decreased, especially for *in situ* applications.

Related to the concern about delamination, questions have arisen regarding the tensile strength of samples containing optical fibers. Preliminary studies indicated that yield strengths of composite panels with imbedded optical fibers are higher along the fibers than panels with no optical fibers. Because the ultimate tensile strength (UTS) of the composite panel, σ_c, depends on the constituent components, this result is expected, if the optical fiber bonds to the matrix at least as well as the optical fibers do. That is,

$$\sigma_c = \sigma_g V_g + \sigma_m V_m + \sigma_o V_o \qquad (3.7)$$

where σ is the UTS and V is the volume fraction of g, the graphite fibers, m, the matrix, and o, the optical fibers [62]. Similarly, the Young's modulus, E_c, can be written

$$E_c = E_g V_g + E_m V_m + E_o V_o. \tag{3.8}$$

Generally, the yield stress of the matrix is much less than that of the fibers. This can be seen by considering that unreinforced epoxy resins usually possess a UTS of around 70 MPa and Young's moduli of around 2.5 GPa [63], while typical carbon fibers show a UTS of 2.0 GPa, and Young's moduli of 420 GPa. By comparison, drawn silica demonstrates a UTS typically higher than carbon, around 3.5 GPa, but a much lower Young's modulus, around 85 GPa [64]. Thus, as the load is increased on a composite sample containing these components, the matrix will flow plastically and the fibers will continue to deform elastically until they fracture (these fibers show virtually no plasticity).

In the range between the onset of matrix flow and fiber failure, the Young's modulus of the composite sample at a given strain can be shown to be

$$E_c = E_g V_g + \zeta_\varepsilon V_m + E_o V_o \tag{3.9}$$

where ζ is the slope of the stress-strain curve of the matrix [62]. This term is generally small and therefore neglected, simplifying (3.9) to

$$E_c = E_g V_g + E_o V_o. \tag{3.10}$$

In addition, since the UTS of the matrix is much smaller than that of the fibers, (3.7) can be written as

$$\sigma_c = \sigma_g V_g + \sigma_o V_o. \qquad (3.11)$$

Comparing (3.10) and (3.11) with the respective UTS and E values for the fiber types, it can be argued that if the optical fiber can be integrated into the composite without introducing points of stress concentration, the sample tensile strength should increase, while the Young's modulus should decrease. In practice, because the Young's modulus may be defined as the ratio between the applied stress and the fractional extension of the sample, this means that while the composite would exhibit greater strength, the toughness would suffer. However, ambiguities in fiber-matrix bonding, as well as the unknowns regarding the exact properties of the carbon and optical fibers in hand, all suggest that more quantitative data be collected to determine how different types of fibers and how the number of fibers per area affect yield strength.

3.4.3 Composite Testing

In considering the many questions regarding the fiber/composite interaction that remain the fabrication of several types of test panels was proposed. Because of the complexity involved, the tests aimed at isolating various factors

contributing to both the mechanical sensitivity and integrity. Ideally, several panels of each type would be desired to substantiate the data obtained from them, as well as establish "noise" boundaries, and so on. The suggested panels (listed by type), tests, and what they were intended to show, will be discussed in the following paragraphs. The results of those actually carried out will be presented in the next section.

1. Samples for Mechanical Testing (refer to Figure 3.12).
    a) Control panel: composite fibers in long direction, no optical fiber.
    b) Control panel: composite fibers in short direction, no optical fiber.
    c) Composite fibers in long direction, one parallel optical fiber.
    d) Composite fibers in short direction, one parallel optical fiber.
    e) composite figures in long direction, five parallel optical fibers inch.
    f) Composite fibers in short direction, five perpendicular optical fibers per inch.
    g) Component fibers in long direction, twenty parallel optical fibers per inch.

h) Component fibers in long direction, one perpendicular optical fiber.

i) Composite fibers in long direction, five perpendicular optical fibers.

The sample coupons were all to be 7.5 x 12.5 cm coupons, four plys thick. The fiber was the same Corning 50/125 graded index type used in earlier tests. The test procedure was to mount each sample lengthwise in a load frame and load until failure. With respect to control samples 1a and 1b, 1c and 1d were expected to show little added tensile strength, while 1e, 1f, 1g, and 1h were expected to show a measurable increase. Samples 1i and 1j were to help determine the degree to which optical fibers running across the strain field would degrade tensile strengths and concentrate the stress.

2. Samples for Optical Testing (refer to Figure 3.13).

a) Composite fibers in long direction, four long, parallel optical fibers, each of a different type.

b) Composite fibers in long direction, three long, parallel optical fibers.

c) Composite fibers in short direction, three perpendicular optical fibers.

d) Composite fibers in long direction, five short pieces of optical fiber in short direction, three long optical fibers in long direction.

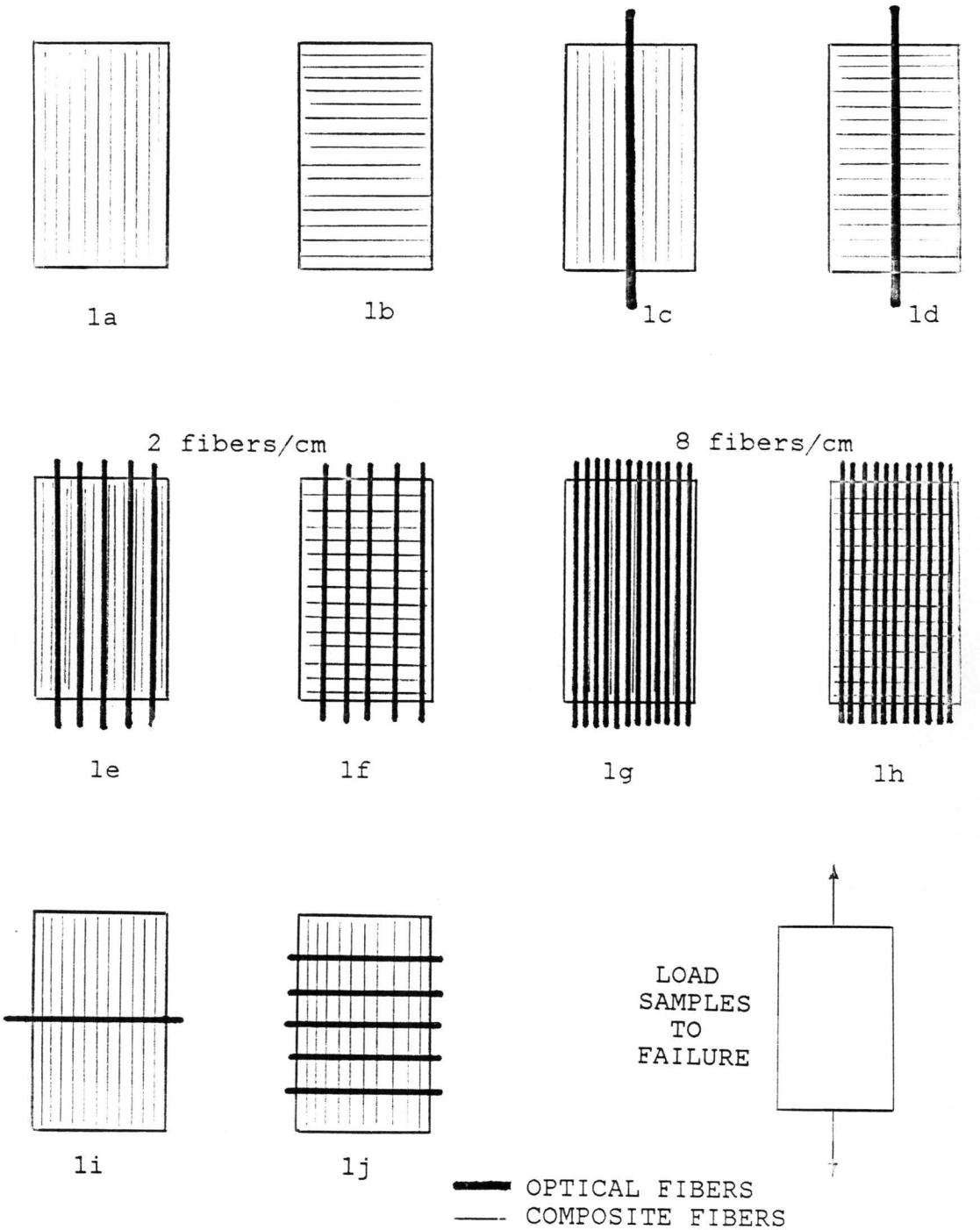

Figure 3.12: Samples for Mechanical Testing

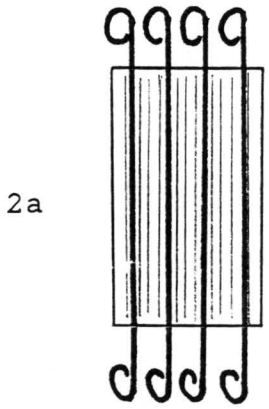

a) Corning
b) Plastic
c) ITT
d) Oil Filled

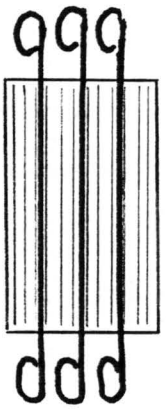

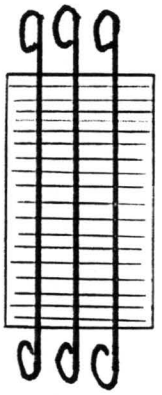

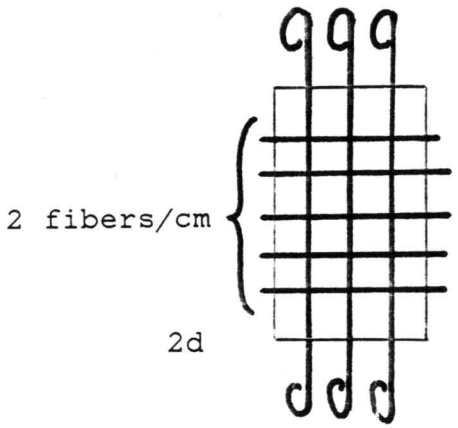

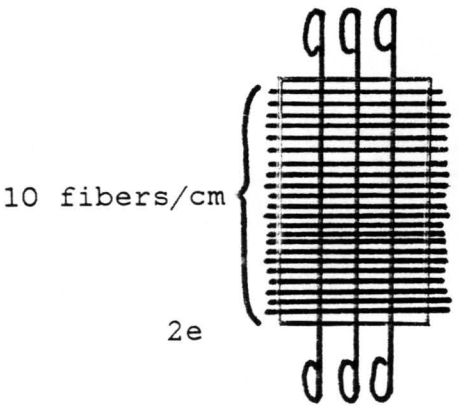

Figure 3.13: Samples for Optical Testing

e) Composite fibers in long direction, twenty-five short pieces of optical fiber in short direction, three long optical fibers in long direction.

Samples 2a - 2e are all 7.5 x 12.5 cm coupons, four plys thick. "Long" fibers are those having a meter or two on either side of the panel, suitable for optical coupling.

Sample 2a was to be loaded in the same way as the previous samples. However, in this case, light was to be injected into each fiber (perhaps one at a time) at equal load intervals, and their outputs monitored. Since the fibers are of different type, each should break at a different strain level, thus acting as a crude strain level indicator. The four fibers to be used were the Corning graded index, a graded index fiber in an oil-filled buffer (hereafter referred to as oil-filled), ITT single mode fiber, and a large diameter (0.5 mm) plastic fiber.

Samples 2b and 2c were to be used to compare the effect of running parallel and perpendicular to the composite fibers. If the fiber tows actually introduce significant microbending, 2c should allow considerably less thru-put intensity than 2b, or, if OTDR is used, 2c should display considerably higher negative slope (attenuation) than 2b.

Samples 2d and 2e were designed to purposely introduce deformation. Because of the similar dimensions between the

light-carrying fibers and the short fiber pieces, curvature and associated losses should be pronounced. Presumably 2e will create higher fiber attenuation, unless the bending periodicity comes into play.

f) 15 x 20 cm coupon, 8 plys thick; one long optical fiber weaves in and out of panel between top two plys. Another weaves between bottom two plys; all microbends exterior to panel, and ply orientations as shown. Refer to Figure 3.14

g) 15 x 20 cm coupon, 28 plys thick; three sets of three parallel optical fibers, each set of a different type; the first fiber in each set between top two plys, second between middle two plys; all optical fibers parallel to composite fibers in neighboring plys. Refer to Figure 3.15.

Sample 2f was mainly to be tested with an OTDR. The results of the attenuation measurement were to be compared with the data from the previously made panel. If the attenuation was due to the fiber tows, this sample should show more since each fiber was to be in contact with perpendicular composite fibers in one ply (as opposed to all parallel fibers in the previous case). If, on the other hand, the high attenuation was caused by large bends near the edges, this sample should show less, since the direction reversals

occur outside the panel in much larger bending radii than those inside the prior sample. In any case, this specimen was to provide OTDR slope information from two different layers when the panel was loaded.

Sample 2g was also intended to collect information originating in the different layers of composite. As with 2f, fibers a1, a2, and a3 and c1, c2, and c3 were to be multimode (Corning and oil-filled, respectively). Fibers b1, b2, and b3, were to be ITT single-mode, and available for interferometric measurements. The sample was to be loaded as a cantilever, while monitoring any of the fibers desired. Microbending due to tows would have been reduced, since all fibers were to be parallel.

3.4.3.1 Fabrication of Samples

Each of the proposed test panels were fabricated at NASA Langley Research Center, Hampton, Virginia, with aid of NASA personnel. In addition, one extra coupon resembling 1c, using ITT fiber, and two resembling 1e, one using ITT and the other using oil-filled fibers were made. Cutting the plys from pre-preg roll, laying the plys with optical fibers, and autoclaving the samples took about two full working days.

The results of the sample fabrication were rather disappointing. None of the samples intended for optical testing

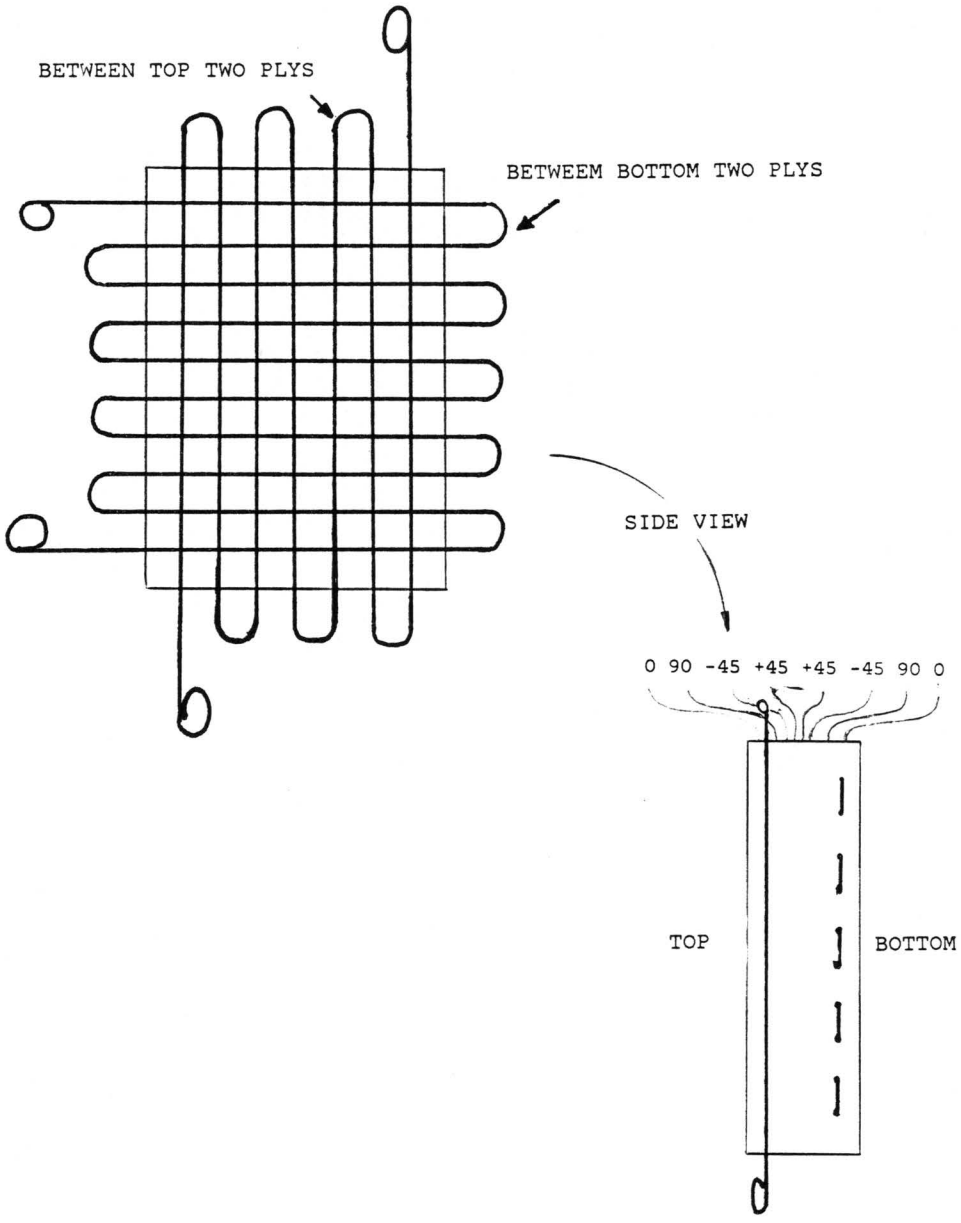

Figure 3.14: Sample for Testing Imbedded Fiber Attenuation

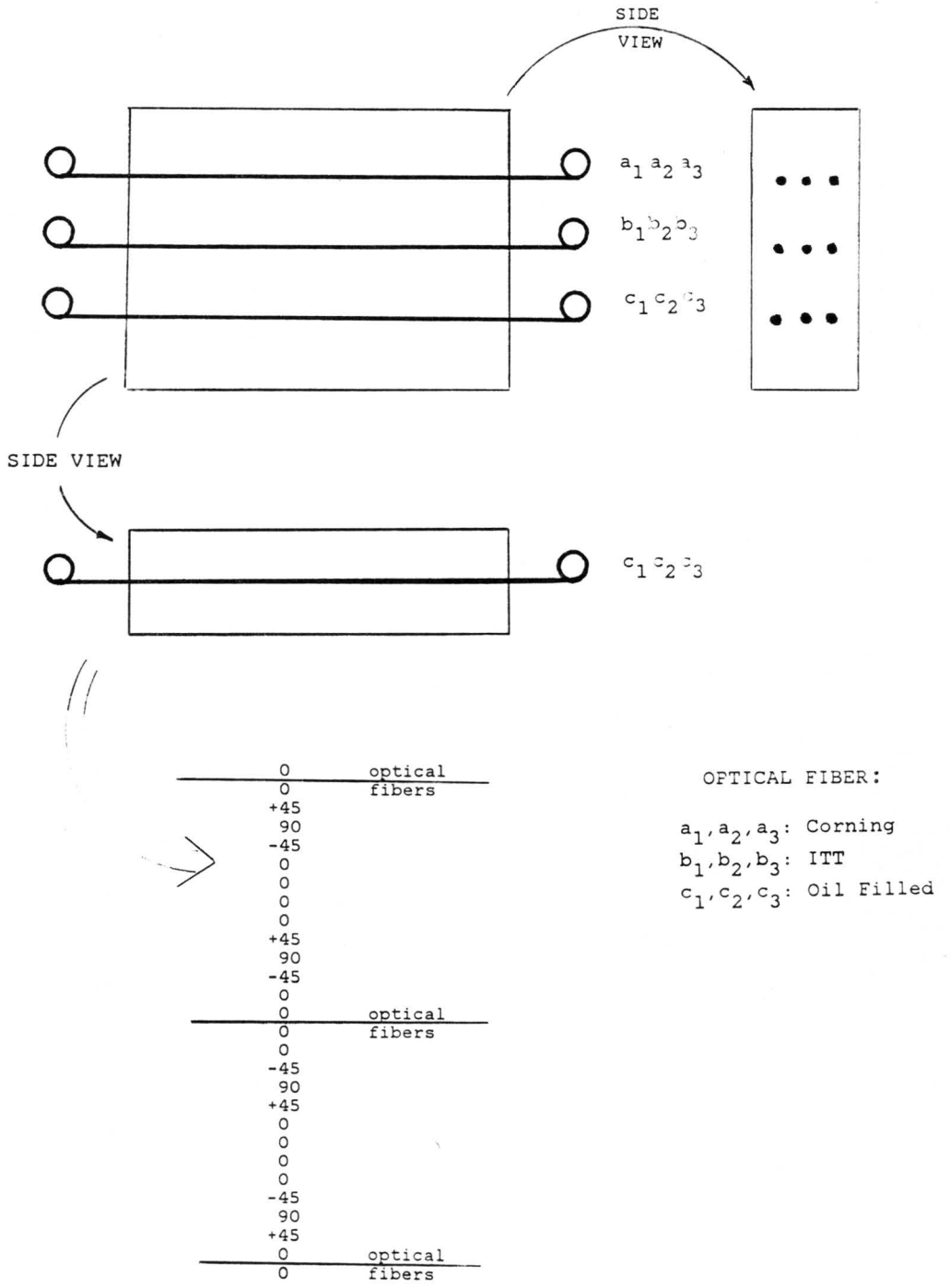

Figure 3.15: Sample for Multilayer Testing

survived the curing process, primarily due to the epoxy having bled out of the panels. When it hardened, it acted to glue the external fiber coils to one another and to the cloth in which the samples were wrapped for autoclaving.

In addition, the fiber jackets melted and burned to different degrees. The ITT jacket, consisting of a reasonably hard plastic coating on top of a soft elastomeric (Hytrel) coating, survived the best. This jacket did not melt enough to stick to itself, but did become brittle and kinked, sometimes severely enough to break the optical fiber within.

The Corning jacket, a soft polymer (CPC), softened enough to adhere the fiber coils to one another. It also yellowed and hardened, breaking the external fibers in dozens of places throughout the batch. Stripping this fiber after curing was only possible chemically (using methyl chloride); conventional razor blade stripping was intractable due to jacket hardening and subsequent fiber fragility.

The oil-filled fiber jacket apparently melted to a high degree, flowed into the cloth beneath, and rehardened. Broad lines of diffused black coating followed the original fiber coil paths, with the bare fiber clearly visible above the lines. In most cases the fiber itself remained in tact, revealing an even melting, unlike the previous cases.

Finally, the plastic fiber used in sample 2a was found to be totally unsuitable under the given curing conditions. When the specimen emerged from the autoclave, the fiber had completely disappeared; the lead lengths originally hanging out of the panel apparently had liquefied. And, although the broad ITT fiber was clearly visible inside the samples, the even broader plastic fiber could not be discerned, indicating that it had melted into the matrix.

3.4.3.2 Optical Testing

Only a few simple optical tests were actually carried out. In one case, a Corning fiber, one in a tangle of many coming out of sample 2e, was stripped and roughly cleaved. Laser light was focused onto the fiber end, and light was seen emerging on the other side of the coupon. Although the output intensity was not as high as could be expected (probably due to launch conditions), it seemed clear that the portion of fiber in the composite was relatively unharmed.

The second optical test was run on an ITT fiber in the extra sample resembling 1e. The jacket was easily stripped with a razor blade; the fiber ends were flat enough to allow for reasonable coupling without attempting to cleave them. The coupon was trimmed into a one inch strip and loaded in a cantilevered fashion, as shown in Figure 3.16. When laser

light was injected into the fiber, a surprisingly intense pattern resulted. However, even when the sample was subject to considerable bending, no change in the output pattern was visible.

3.4.3.3 Mechanical Testing

The samples for mechanical testing did not require long lengths of useable optical fiber before and after the panel, so it appeared that load testing would be quick and easy. However, the Instrom load frame used (Engineering and Science Mechanics Department, Virginia Tech) would accept only 5 cm wide strips, in contrast to the 7.5 cm wide samples. Accordingly, the panels were sectioned lengthwise, using a tool-mounted razor blade (with many replacement blades required). Also, the proper loading sequence had to be found by trial and error, since several panels were quite weak in one direction, depending on lay-up orientation. Care was required to insure that the sample broke due to tensile loading rather than due to some unwanted torsion or preloading stress.

The next problem occurred as a result of the load frame vise jaws. Sample 1a was mounted and loaded to 1650 kg before any change was visible. The load rate, constant throughout all the testing, was 0.127 cm/min. At 506 MPa.,

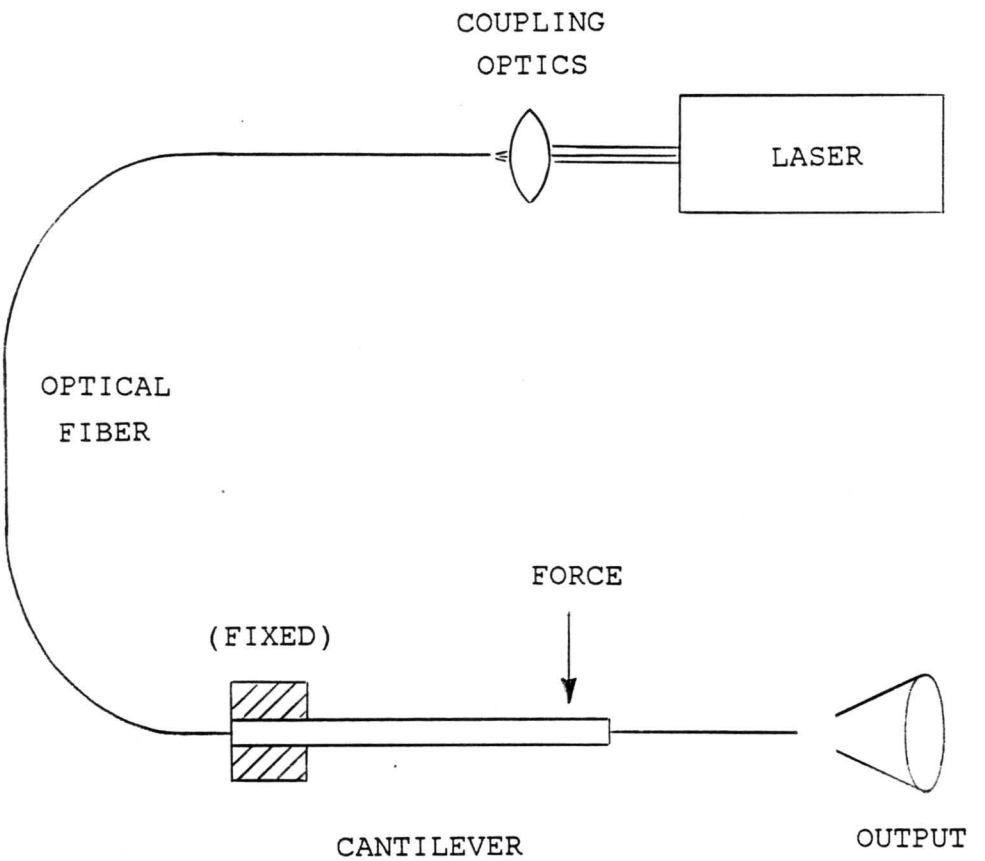

Figure 3.16: Optical Testing of Sample Under Cantilever Load

the sample splintered vertically because of the teeth in the vise jaws. All samples tested subsequently were padded with emery cloth in the grips.

Although the padding did prevent the vise from crushing the samples, it did not prohibit the sample from slipping. For example, sample 1c was loaded as before until it reached 2200 kg, when it split vertically, about 0.5 cm from the center. The marks left on the sample, as seen in Figure 3.17, indicate that the probable cause of breaking was due to uneven slippage. This in turn applied a high shearing moment against the epoxy matrix, resulting in an immediate split. Samples sections from 1e and 1g split in a similar manner.

Slipping was again the probable cause for failure with the samples which resembled 1c and 1e only using ITT fibers. However, in both these cases, the vertical split appeared along the optical fiber. It is important to note that the original diameter of the jacketed ITT fiber is twice as large as that of the Corning fiber (460 μm, compared to 230 μm). Also, as discussed earlier, the Corning fiber melts considerably during curing, while the ITT fiber does not, meaning their effective diameters are even more separated. It is therefore likely that more significant voids in the resin occur along the larger fiber. This would be the weak-

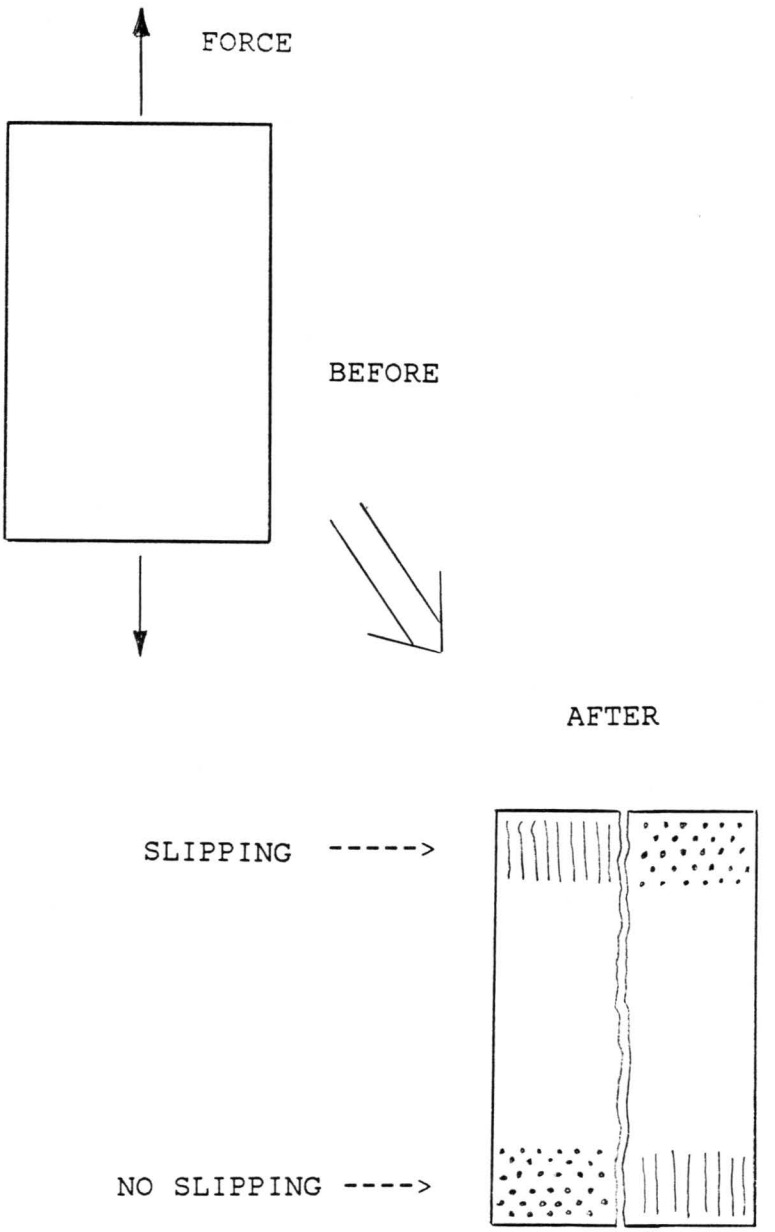

Figure 3.17: Sample Breakage Apparently Due to Slipping

est point in the matrix, and so would fail first when subject to shearing force.

Another section from sample 1g, containing 12 optical fibers, was tested next. When the load reached 8.73 GPa., a perpendicular break occurred on one side, as shown in Figure 3.17. Although some slip marks appeared on the splintered sections, these probably resulted from the transfer of the load to these pieces as the main break was taking place.

Finally, sample 1f, containing graphite fibers transverse to the applied load, was mounted and strained. A perpendicular break occurred at 34.6 MPa, this time at the edge of the vice jaw. It is not clear whether this point is valid, since the strain may have been concentrated right at the vice edge, causing the failure. However, even so, the relatively small load required to break the sample is not surprising, considering the only restoring forces resided in the optical fibers and the matrix material.

In an effort to alleviate the slipping problem, ways to grasp the samples more securely, yet not damage them or create stress "hot spots" were discussed. Bonding four rectangles of aluminum shim stock to the composite, as shown in Figure 3.18 seemed to be a reasonable solution. Both the optimum thickness of the aluminum shim and the appropriate adhesive, had yet to be determined, as well as any necessary

surface preparation, as has been suggested for similar Young's modulus tests [64]. Using some remaining composite strips, several samples were tried.

In one test, four pieces of shim, 0.2 mm thick, were bonded to a composite section using "5 Minute" Epoxy. After curing for one hour, the sample was mounted in the load frame and strained. At a load of 2250 kg, the epoxy let go of the aluminum shim and the sample split lengthwise on one edge.

In another test, Epoxy x-8073 was used. This time it was the thin shim stock that failed, tearing at 2700 kg of applied load. Again the composite sample split down the length.

In a third test, aluminum stock 1.6 mm thick was glued to a composite sample with Epoxy 907, and cured at room temperature. When the sample was loaded to 12.7 GPa, a perpendicular break occurred, partly along one joint between the composite and the aluminum, and partly in the middle. No slipping occurred. When the vice jaws of the Instrom were loosened, the two "halves" of the sample were held together by a single thread, that is, the only optical fiber in the sample. It is likely that the fiber was pulled *through* the sample, indicating rather poor adhesion between jacket and matrix. However, there is ample reason to believe that the middle break occurred first.

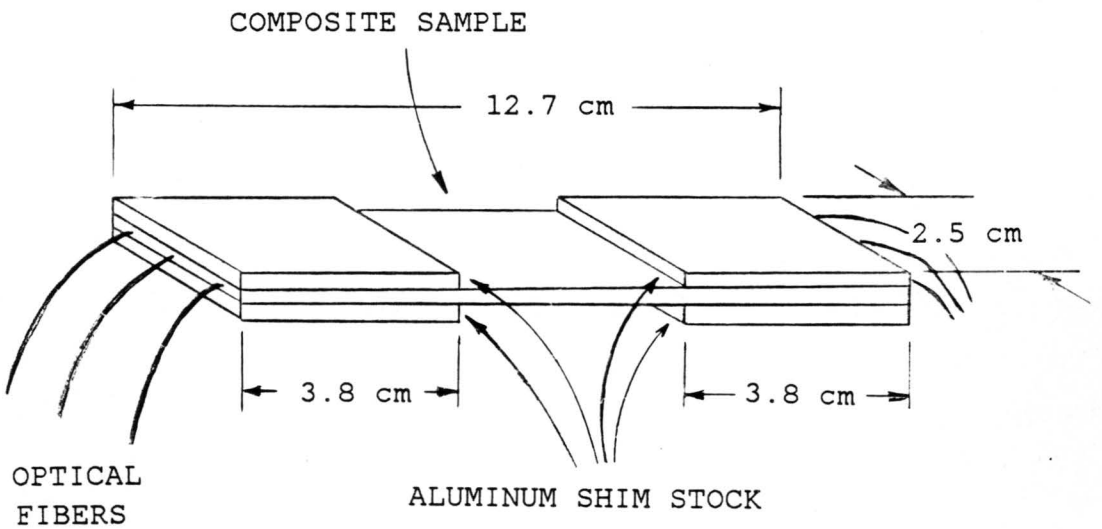

Figure 3.18: Composite Sample Prepared for Load Frame Testing

Two further samples using the same epoxy and aluminum were made and tested, though the epoxy was fast cured at 180°F. Neither sample contained optical fibers, and both broke in the middle without slipping. One sample failed at a load of 13.9 GPa, while the other failed at 11.6 GPa.

3.4.3.4 Discussion

With regard to the optical samples, several conclusions can be drawn and suggestions made for further work. First, it is worth noting that the pre-preg sheets do not actually need to be autoclaved to cure them; placing them on a covered hot plate has been shown to cure them quite adequately for initial testing [65]. This would present the immediate advantage of not significantly damaging any external fibers necessary for optical tests. Also, without a need for an autoclave, many different types of samples can be made quickly and easily, provided one has the pre-preg sheet on hand.

Second, one can see that the fiber jacket plays an important role in the overall considerations. Thus, while interferometric information could well be gained from imbedding the single-mode ITT fiber, the thick, rugged coating seems to compromise the integrity of the composite sample. Clearly, single-mode fiber having smaller dimensions is preferred

for such measurements. However, this may introduce more microbending which is generally unwanted in fiber interferometry. Obviously a maximum compromise needs to be struck between these effects.

For microbending measurements, the oil-filled fiber appeared to be a good choice since the jacket seemed to melt so completely. Again, this would allow the fiber to have more intimate contact with the composite components. However, this jacket could only be used practically if the jacket external to the sample remains intact. Further, this fiber would probably require the application of a strain relieving compound where the fiber enters and exits the sample. As well as protecting the fiber from breakage, the compound would reduce any excess microbending at these points.

For any fiber imbedded, more understanding is required about how the jacket reacts to the curing heat and how well it adheres to the matrix, how the resin fills in around the fiber, and how the fiber interacts with the composite tows. Cross-sectioning the samples already obtained may provide some information in this regard. However, because of the nature of the material, sectioning across fibers is difficult. Care and patience are required to avoid splintering, and special tools may be necessary to section without significantly altering the sample.

Except for gaining a little better understanding on how to imbed the fibers, very little was derived from the optical testings. It is suggested that several of the previous samples be remade, with the effort focusing on the mechanical interaction of the fiber types. Thus, samples resembling 2b and 2c should be remade to investigate the difference between parallel and perpendicular orientation of optical fibers with respect to composite fibers. In addition, a large sample such as 2f should be made, except that the two top and bottom plys should be parallel. Because the imbedded lengths are longer, and the large bends are outside the panel, the effect seen in the samples above should be amplified.

In addition, while the idea of purposely introducing deforming fibers into the composite structure has some merit, undoubtedly these fibers effect the mechanical properties of the panel. At this point in the research, they would raise more questions than they would answer. It is suggested that samples such as 2d and 2e be put off until more is known about the bending mechanisms involved with fiber and composites under test. However, because of the immediate applicability of dynamic break monitoring, another sample resembling 2a should be made. Efforts to find suitable fibers with differing tensile strengths, are currently underway.

It is proposed that a laser in conjunction with a scanning mirror be used to excite the test fibers "simultaneously." This would allow the use of a single, high power source, and would provide continuous amplitude information throughout the test.

Though some seemingly valid mechanical break data was obtained, further tests are definitely required. Several samples such as 1a and 1b needed to be tested to provide control values and standard deviation information. More samples like 1e - 1h should then be tested to obtain quantitative understanding of the effect of optical fibers on the composite tensile strengths.

Finally, a set of samples, each one containing an optical fiber of a different kind, is proposed. Both the optical fibers and the composite fibers are to run perpendicular to the applied load. Noting where the sample breaks would provide valuable insight into the questions concerning jacket, fiber, and matrix interaction, as well as the overall degradation of composites containing imbedded optical fibers.

3.5 OTDR COMPUTER MODELS

The reasons for often including computer models in fundamental research are now well established. A subtle, but important point in this light is that formulating an accurate model forces the researcher to clearly understand the internal mechanisms of the phenomenon under study. As well, the computational power available with a large computer usually brings within reach insights which were nearly impossible to gain with other means. Finally, as is the case here, computers are now frequently interfaced directly with data-gathering instrumentation in order to perform required signal processing. A program which simulates the data generating phenomenon often serves as a useful means of testing the processing program. In this section, a computer model of the OTDR process, as well as some signal processing programs are presented.

3.5.1 Modified Convolution

The original version of the OTDR simulator was written by Jackson [49]. Since that time, the model has been reformulated in order to reflect the current understanding of the OTDR process. Basically, the program simulates the generation and launch of an optical pulse into a fiber, the interaction between the pulse and the fiber, and the collection of the backscattered pulse.

Originally the interaction between pulse and fiber was envisioned as a convolution-type process. However, it was later realized that while strict convolution deals with two waveforms passing each other, OTDR involves constant reflection of one waveform off the other. The computational approach is somewhat similar between the straight convolution and the OTDR simulation however, thus the OTDR program is given the name MODCON (modified convolution).

In the true OTDR situation, the total distance travelled by any point in the reflected optical pulse, L_t, is given by

$$L_t = 2L_f + L_p, \tag{3.12}$$

where L_f is the length of the fiber and L_p is the length (in space) of the optical fiber, and where it is assumed that $L_f > L_p$. The $2L_f$ represents the distance for the pulse to go down and back, while the L_p term signifies that the entire pulse must go through the fiber. This is depicted in Figure 3.19.

For a pulse and a fiber consisting of L_p and L_f discrete units, respectively, the total distance (in units) travelled becomes

$$L_t = 2L_f + L_p - 1. \tag{3.13}$$

The subtraction of one comes about because two blocks interface at their common boundary. The boundaries number one less than the blocks, in much the same way as there are four spaces between five fingers.

$$D_t = 2L_f + L_p$$

(D_t = TOTAL DISTANCE TRAVELED BY POINT a)

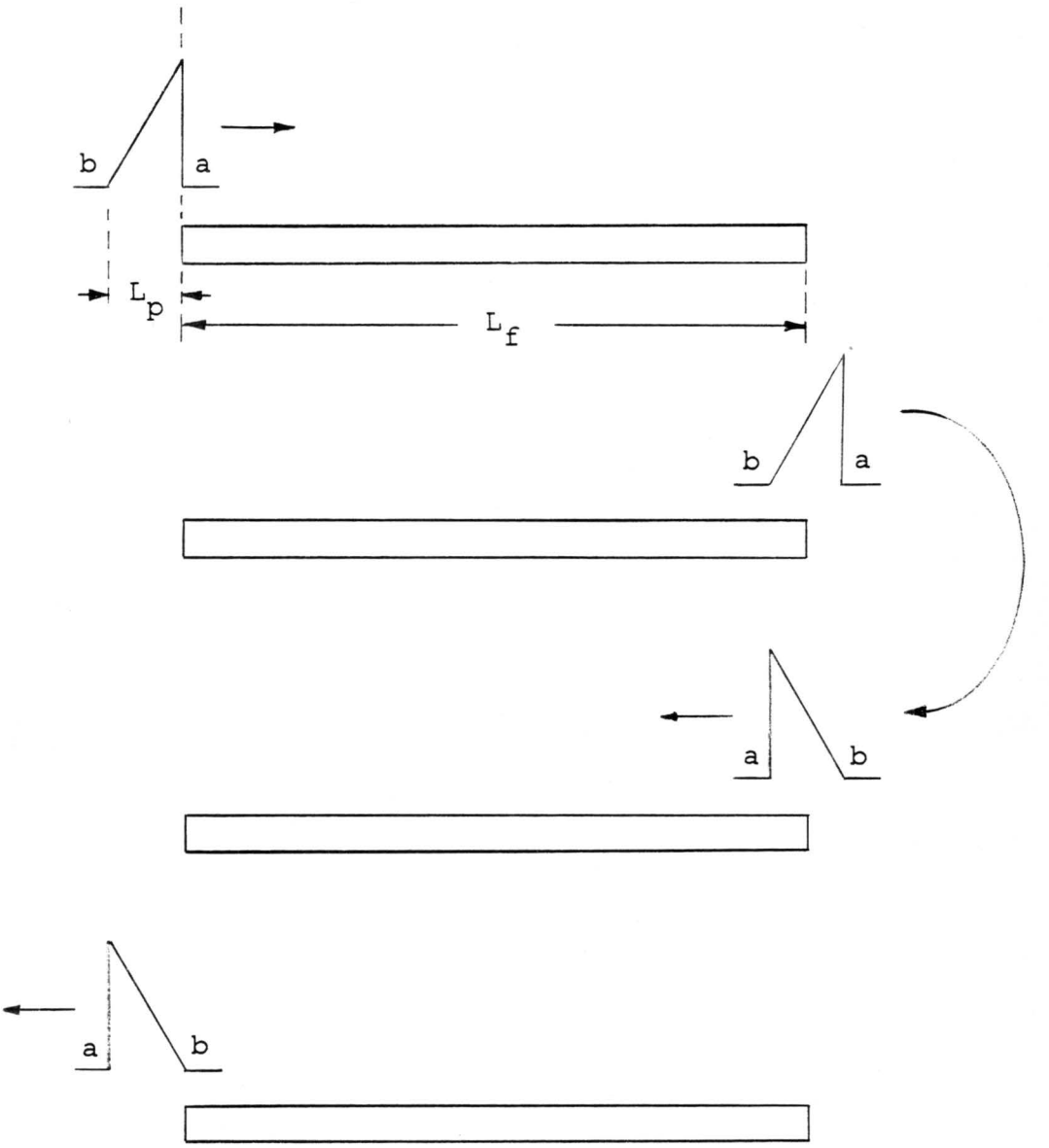

Figure 3.19: Total Distance Travelled by the Backscattered Pulse

A small discrete model is shown in Figure 3.20. A pulse four meters long (corresponding to 20 nsec in time) is broken into segments, one segment or unit per meter. The length of the pulse in segments, L_p, is then 1 seg/m * 4 m = 4 segments, where the ith segment is given a value P_i to contain the average optical intensity within that segment of the pulse.

The pulse enters from the left a five meter long fiber, also divided into one segment per meter, so that $L_f = 5$. Associated with the fiber at each point is the reflection and absorption coefficients. For simplicity, the absorption is neglected for the moment. Thus, the jth segment of the fiber has a reflection coefficient of F_j. The pulse moves through the fiber in steps, where the value k counts the number of steps at any given time.

At each step in time, the ith segment of the optical pulse interacts with the jth segment of the fiber in a multiplicative fashion. At the next step, the product $P_i * F_j$ begins to travel back towards the front end of the fiber. The forward travelling optical pulse segment is then reduced to $P_i\nabla$, where $P_i\nabla = P_i - P_i * F_j$. Meanwhile, the (i+1)th segment has entered the fiber and is itself interacting with the jth fiber segment.

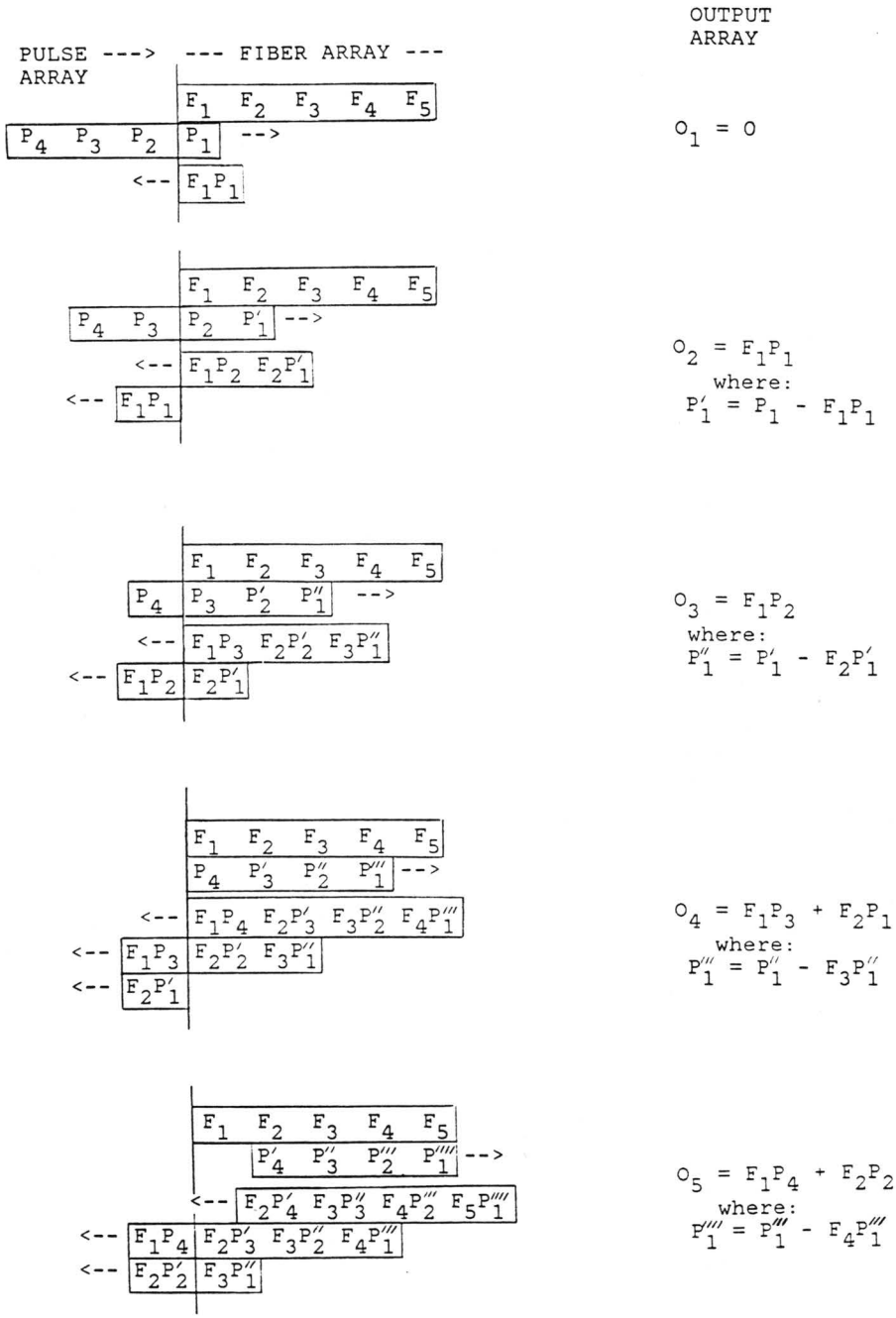

Figure 3.20: OTDR Discrete Model

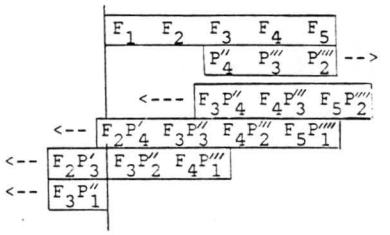

$O_6 = F_2P_3 + F_3P_1$

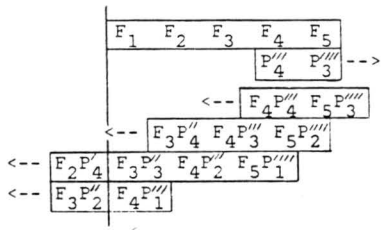

$O_7 = F_2P_4 + F_3P_2$

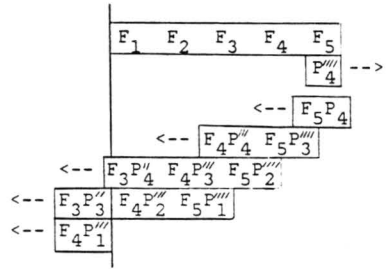

$O_8 = F_3P_3 + F_4P_1$

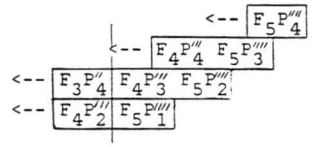

$O_9 = F_3P_4 + F_4P_2$

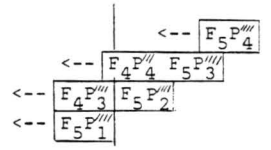

$O_{10} = F_4P_3 + F_5P_1$

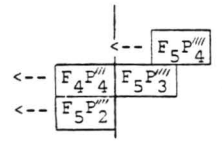

$O_{11} = F_4P_4 + F_5P_2$

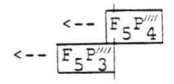

$O_{12} = F_5P_3$

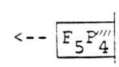

$O_{13} = F_5P_4$

OTDR Discrete Model (Continued)

As the stepping continues, the backscattered intensities eventually emerge from the front end of the fiber. These intensities are stored in an output array named O, which is indexed by the number of the step, k. The values of O_k are shown to the right in the figure.

The ideas presented in this modified convolution model provide the basis of the OTDR simulator program. In addition, the program allows for the inclusion of both the intrinsic absorption of the fiber, as well as high absorption regions, say due to fabrication defects. A listing of the program, and a more detailed discussion of the algorithm appear in Appendix 1.

The modified convolution of a 2 meter long optical pulse (square) and a 90 meter fiber, neglecting scattering loss, absorption, and the large reflection from the far end, produces the output shown in Figure 3.21. The major difference between this and the output of a straight convolution of Figure 3.22 is the length of the output vector, well known to be simply $L_f + L_p$ in the latter case. When scattering, including the far end reflection, and intrinsic absorption are included, an output such as in Figure 3.23 appears. In this and subsequent figures, the position for each discrete reflection along the fiber appears on the horizontal axis, rather than the total distance travelled by the optical pulse (the length of the output vector).

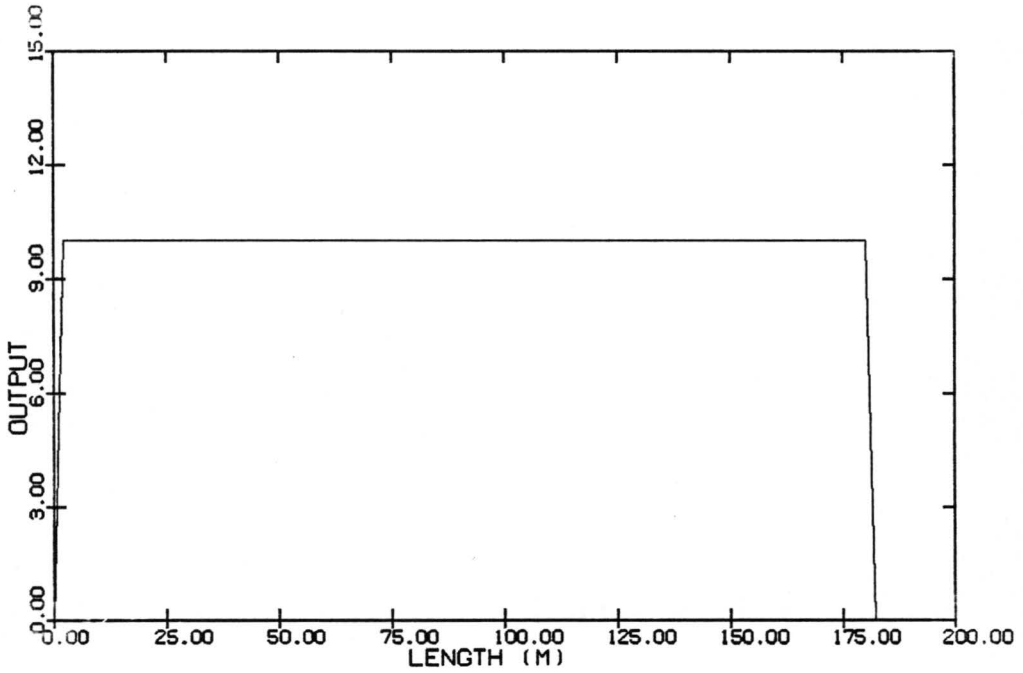

Figure 3.21: Modified Convolution of a 2m Pulse and a 90m Fiber

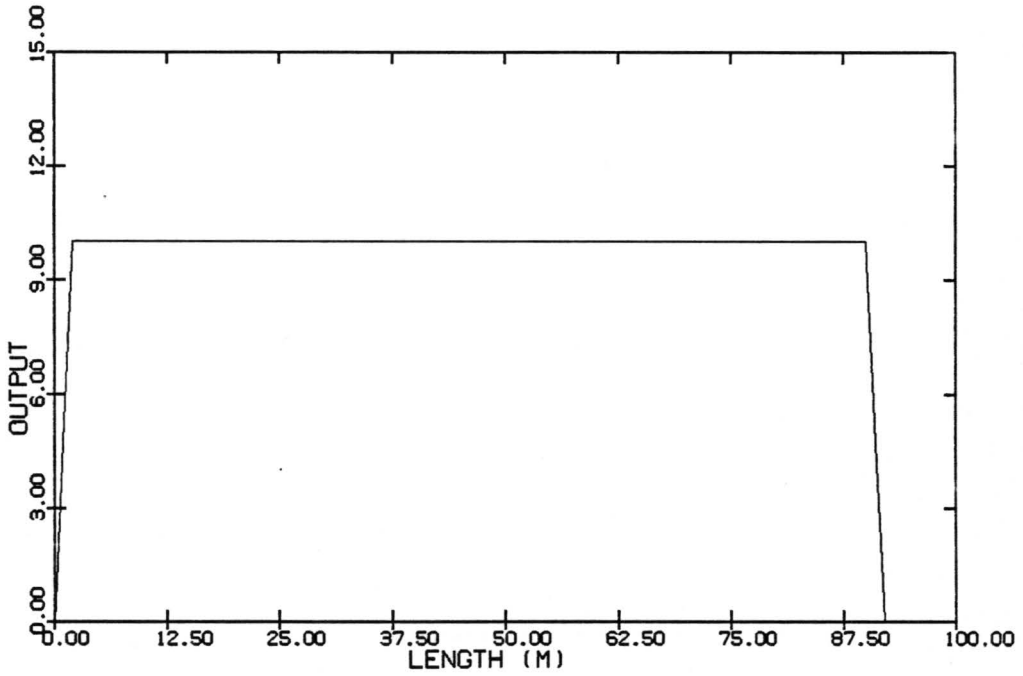

Figure 3.22: Straight Convolution of a 2m and a 90m Rectangle

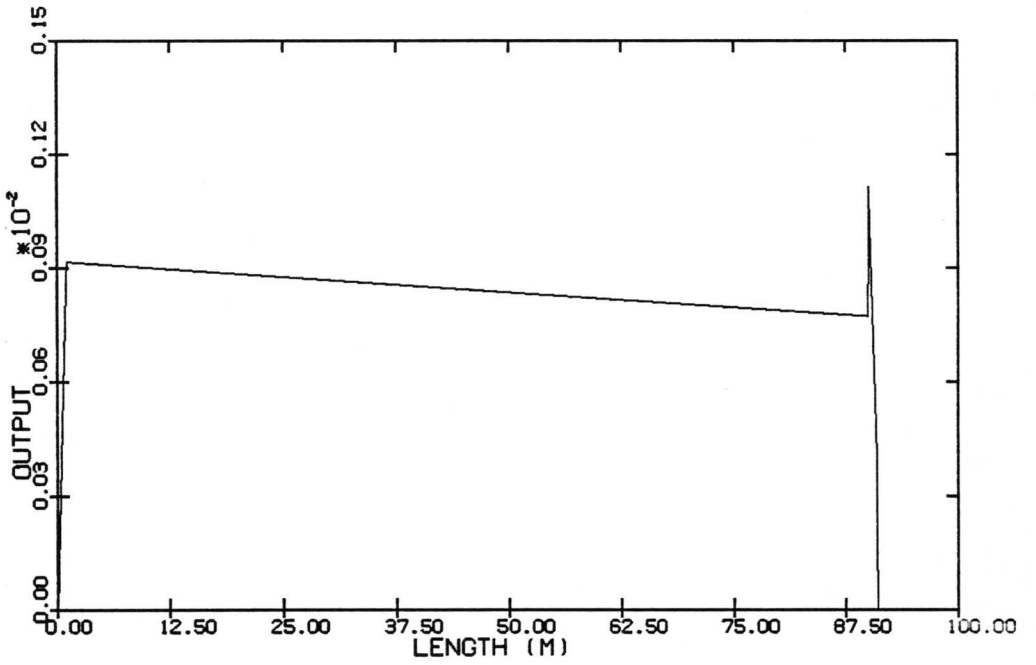

Figure 3.23: MODCON Including Scattering and Absorption

In practice, curves such as Figure 3.23 are rarely observed. Because the backscattered signal of interest is generally a small one, a significant amount of noise is often introduced. Noise can be first simulated using a pseudo-random number generator, and then added to the MODCON output to give a plot such as shown in Figure 3.24. In this case, the noise factor is relatively low, corresponding to a strong output signal. This could be generated by using a high power laser and a fiber demonstrating a large backscattering coefficient. Figure 3.25 exemplifies the high noise output expected when a low power source or low loss fiber is used.

Consider now the presence of a single microbend sensor, located 40m along the length of the fiber and extending for ten meters. If a uniform pressure is exerted along the length of the sensor, an output such as seen in Figure 3.26 may result. The change in slope between 40 and 50m is basically caused by the increased scattering coefficient along this length, due to local index changes and radiative losses. It is this slope which provides information regarding the amplitude of the applied load. Analysis of this portion will be taken up in the next section. Finally, a more realistic situation appears in Figure 3.27, where a modest amount of noise has been added.

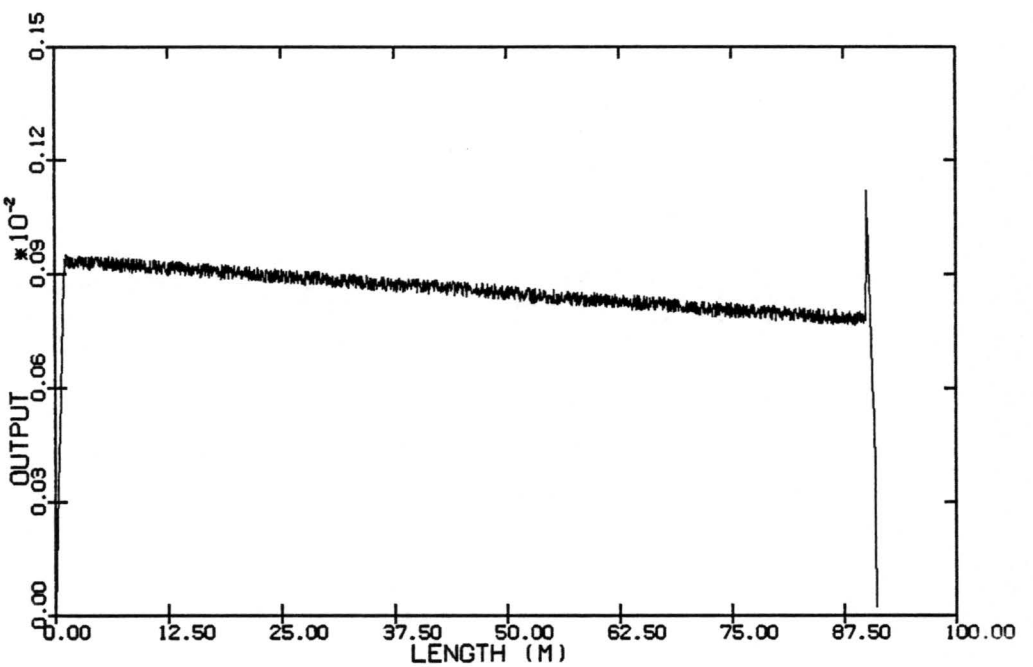

Figure 3.24: Plot of Previous, Including a Low Noise Factor

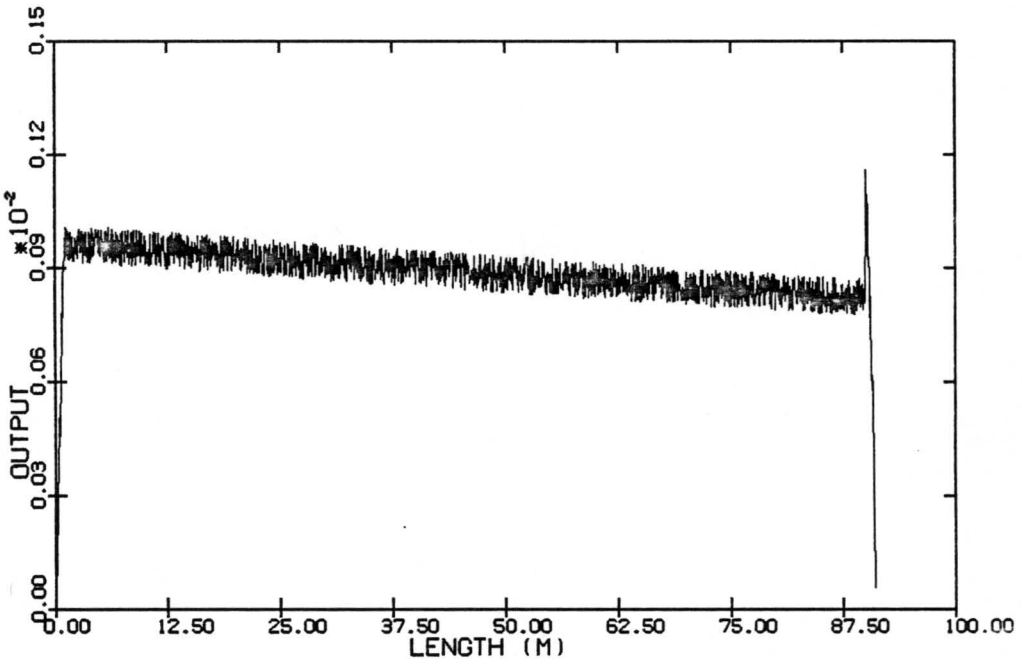

Figure 3.25: Plot of Previous, Including a High Noise Factor

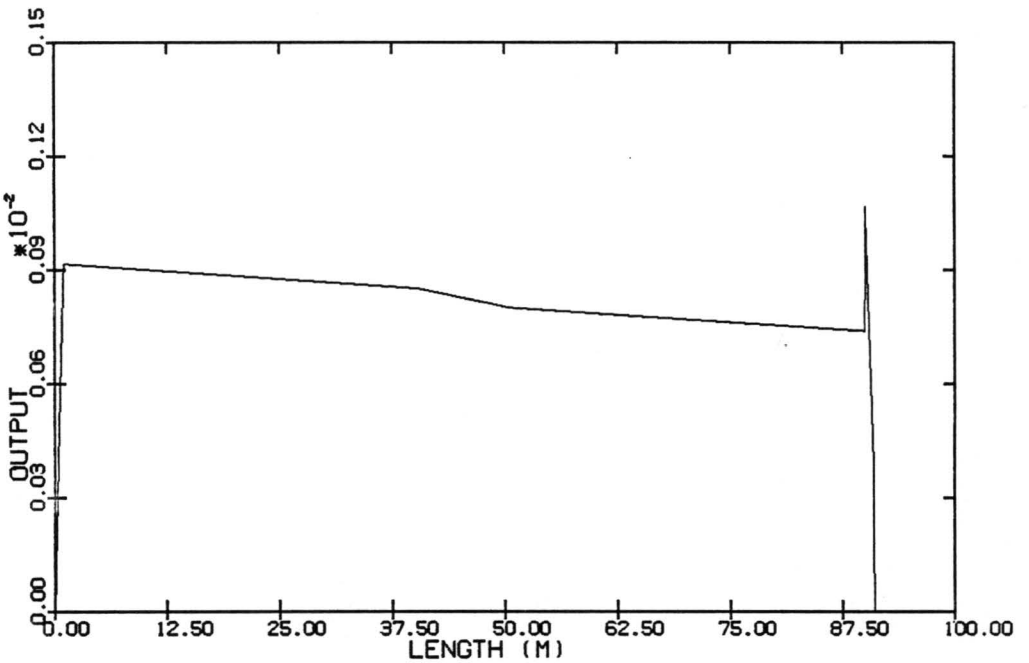

Figure 3.26: Plot of a 90m Fiber with High Loss from 40 to 50m

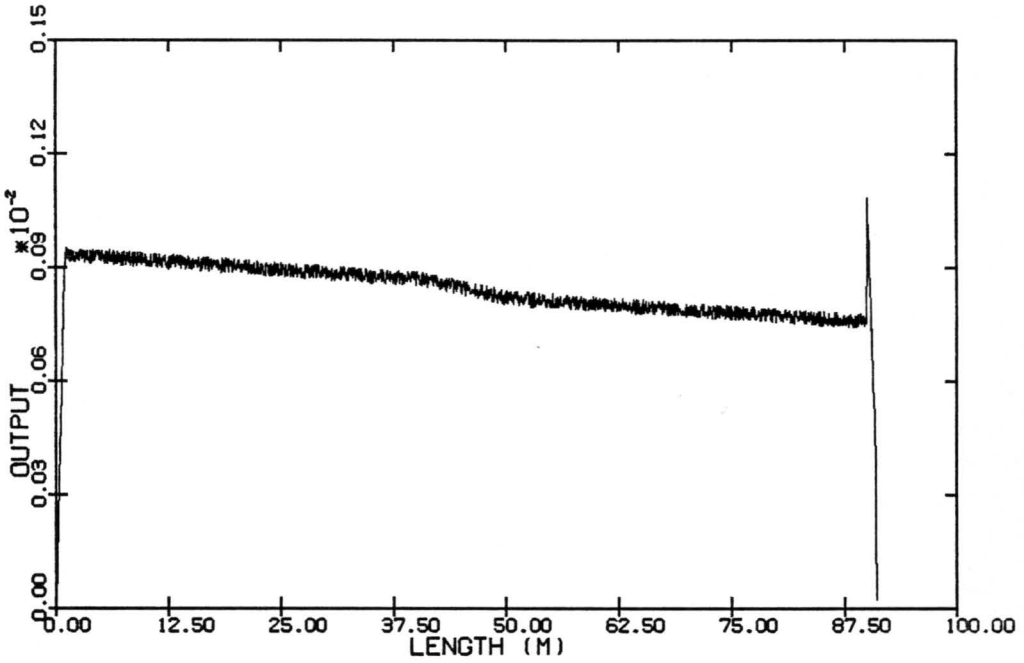

Figure 3.27: Plot of Previous, Including Noise

As a next step, three bending sensors are included, each 0.5m in length. They are modeled at 30, 50, and 70 meters, and each have a different load applied uniformly across the sensor. This begins to approximate the situation described by Martin and Ives, as mentioned in Section 3.2. The output expected for one situation is depicted in Figure 3.28, while Figure 3.29 is the same situation with noise included.

Finally, the continuous distribution of strain is modelled. It is imagined that the fiber is imbedded in a large composite panel, and that a heavy load is applied 45m along its length. A maximum bending, therefore a maximum attenuation and a maximum slope, is expected to occur at 45m. Moreover, less severe bending, attenuation, and slope values are expected in regions adjacent to the position of the applied load. The OTDR output should then resemble Figure 3.30. As before, Figure 3.31 results when the noise characteristic is added.

3.5.2 Data Analysis - The First Derivative

In the previous model, data is generated which simulates the operation of an OTDR system. Although it may be considered imperfect due to the discrete nature of the model, in fact it is not too far from a real situation. The reason for this is that most research-grade OTDR units actually

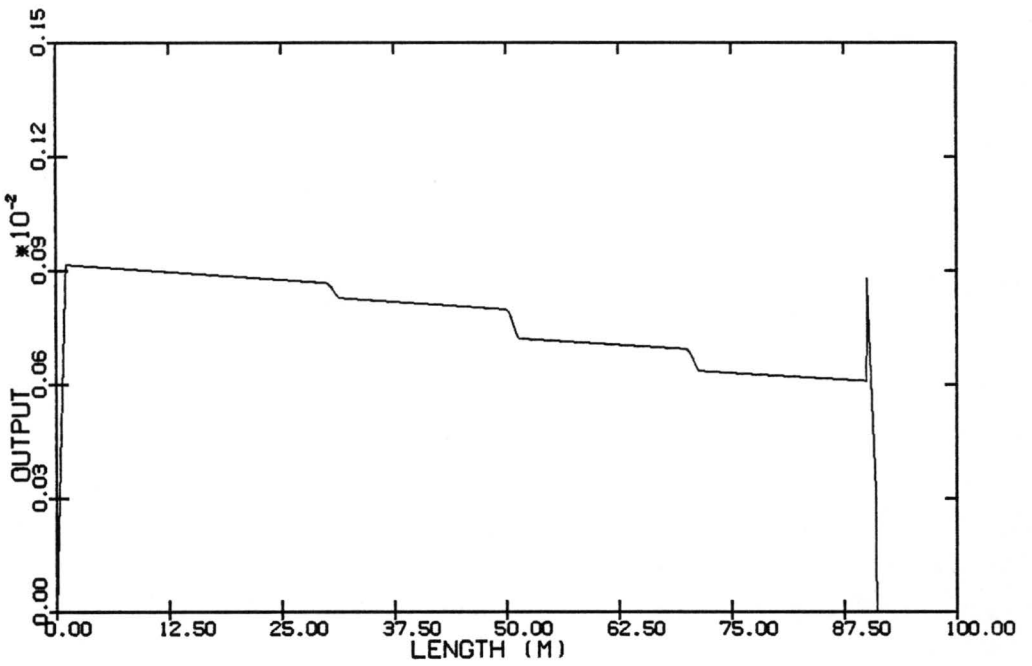

Figure 3.28: MODCON of a Fiber having 3 Microbend Sensors

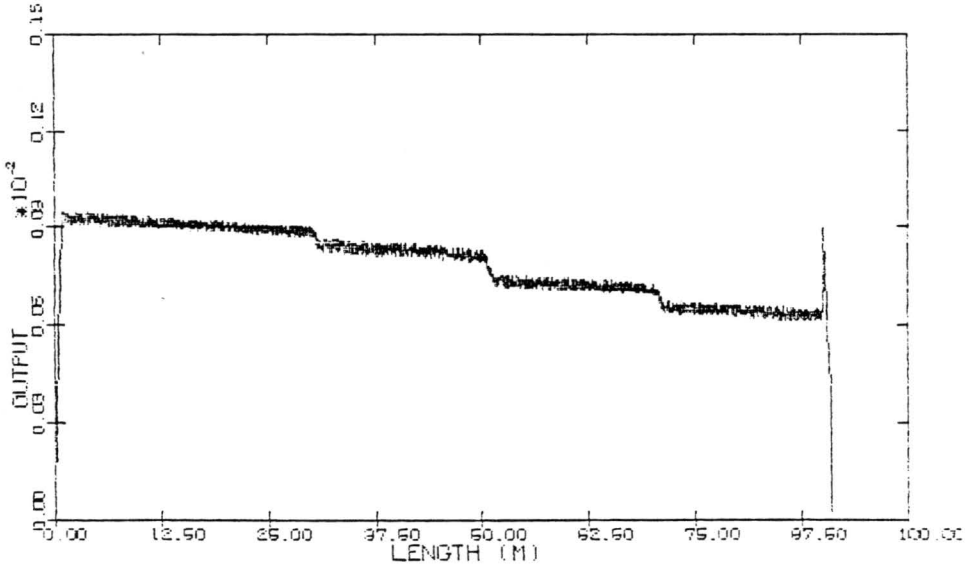

Figure 3.29: Plot of Previous, Including Noise

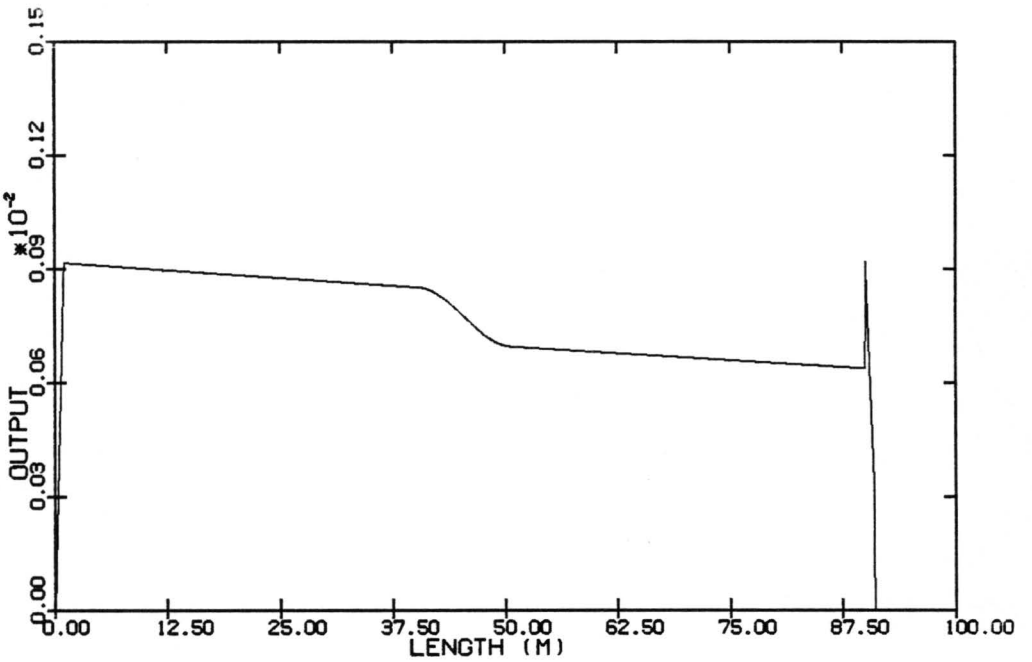

Figure 3.30: MODCON of 10 Meters of Continuous Strain

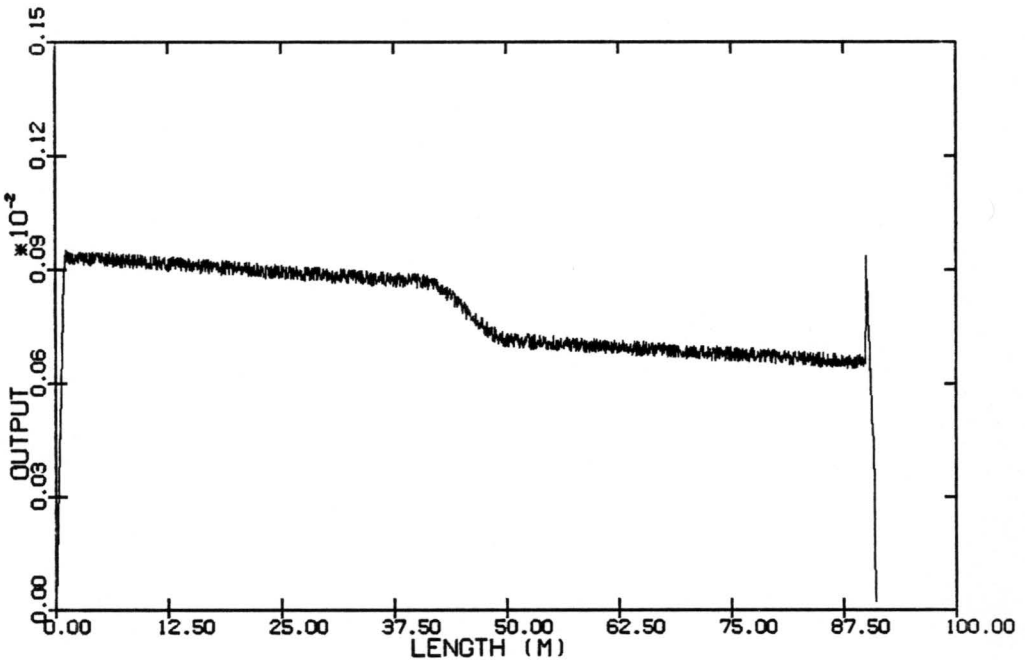

Figure 3.31: Plot of Previous, Including Noise

convert incoming analog data to digital quantities for signal processing and storage. What is sought at this point is a program to aid in the analysis of the data. As alluded to many times earlier, sudden changes in the backscattered profile are the primary indicators of perturbations along the fiber. Accordingly, a program which reads in the digital OTDR signature and yields its first derivative was formulated. The listing of SLOPE, as it is called, appears in Appendix 2, along with a discussion of its features. The merit of using the program as a signal processing tool can be seen through the use of several examples.

First, consider the reasonably large slope changes which appear in Figure 3.26. The five points of sudden difference are marked A - E. If the first derivative is computed, amplified (for scale reasons mostly), and plotted on a scale which includes all the data, Figure 3.32 results. It can be seen from this plot that the sharp changes occurring at points A, D, and E of Figure 3.26 completely overwhelm the more subtle changes occurring at points B and C.

Looking more closely, the beginning and ending discontinuities occur only during the time that the optical pulse is entering and exiting the fiber. Thus, the first and last L_f values of the slope array are zeroed. This is directly applicable to a practical situation, because front end Ray-

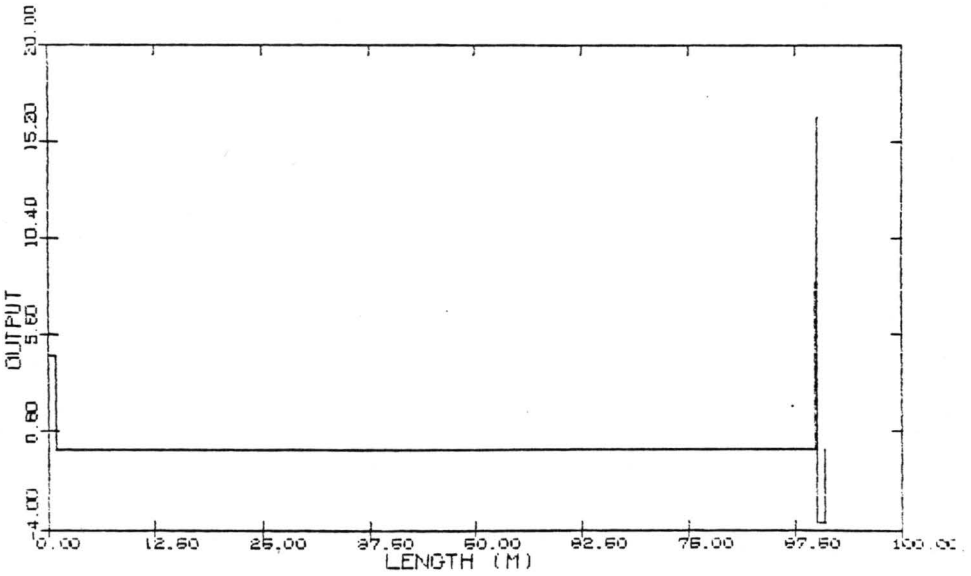

Figure 3.32: 1st Derivative, Showing the Need to Supress the Ends

leigh scattering and back end reflections tend to swamp the wanted signal and reduce the dynamic range in that case as well. With this qualification in place, the same input data yields Figure 3.33. Note that the slope has a constant negative value in the regions before and after the microbend sensor, and a constant but significantly higher negative value within the sensor, corresponding to the earlier stipulation that the pressure was applied uniformly over the range of the sensor.

If the OTDR characteristic from the three sensors, seen in Figure 3.28, is sent to SLOPE, the expected result occurs: three downward-directed spikes, one at 30m, one at 50m, and one at 70m. To see the benefit of SLOPE, however, consider the case where the bending amplitude in the three sensors is very definite, but small. In this example, the attenuation of the unperturbed fiber is 4dB/km, while at 30, 50, and 70m, the attenuation is 20, 40, and 30 dB/km, respectively. The resulting output is shown in Figure 3.34. Although the attenuation at the sensors is significantly different than the norm, slope changes are nearly impossible to discern from the backscattered profile. However, when the first derivative is computed and amplified, the bending position and amplitude can be clearly identified, as seen in Figure 3.35.

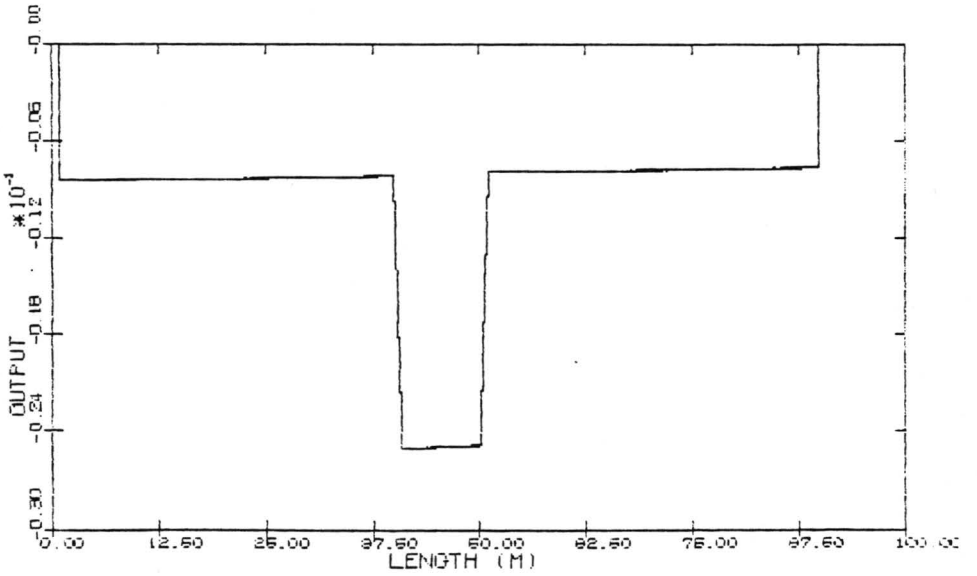

Figure 3.33: 1st Derivative with Supressed End Effects

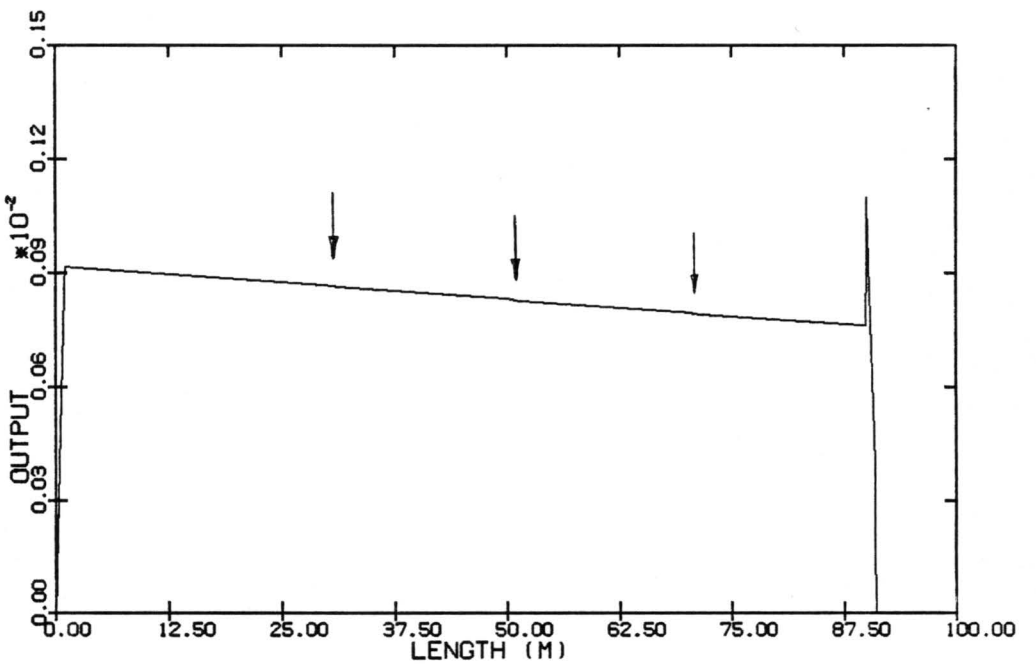

Figure 3.34: MODCON with Three Small-Amplitude Microbend Sensors

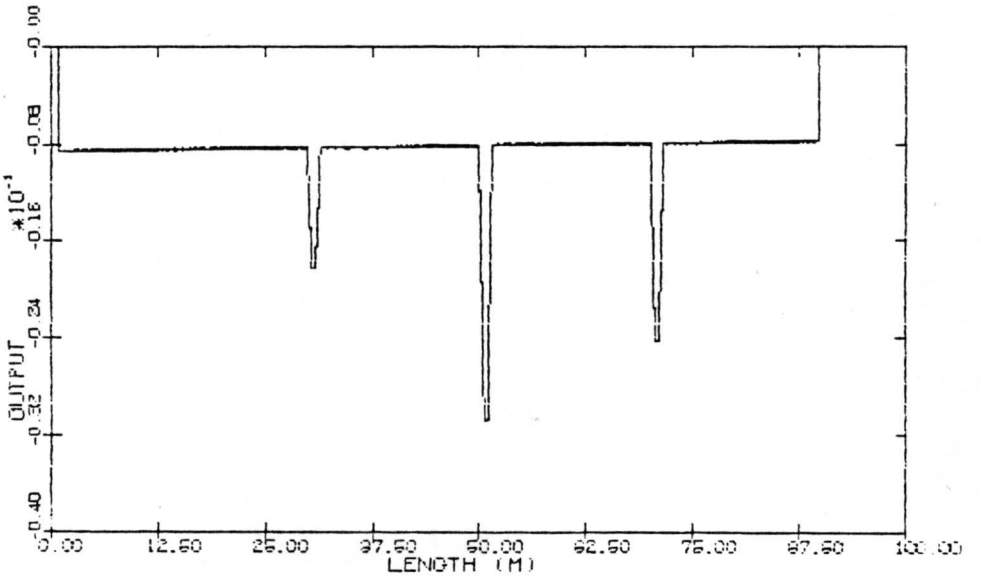

Figure 3.35: 1st Derivative of the Previous

Next, the continuously distributed sensor case is considered. Looking again at Figure 3.30, one may note that it is difficult to say precisely where the slope changes its direction, and therefore where the pressure was applied. In Figure 3.36 however, the first derivative is seen to show this point quite clearly.

Until this point, nothing has been said about the slopes of curves containing noise values. Because the derivative program compares adjacent points to find the slope between them ($\Delta y/\Delta x$), noise in the system can have a catastrophic effect on the calculation. As an example, Figure 3.37 shows the slope of Figure 3.31; obviously any useful data in this plot is deeply buried in noise. It should be mentioned that though this is a computer simulation, the same problem would be encountered if the digitization of a normal OTDR signature were to be processed by computing the first derivative.

The way to solve the noise problem on the computer is the same way as it is done in practical OTDR measurements. That is, several samples are generated and then averaged together to give a synthesized waveform. How many samples must be added together to obtain a reasonably smooth curve (by whatever definition of "reasonably smooth" that applies), is partly dependent on how noisy the sample was to begin with and how truly *random* the noise source is.

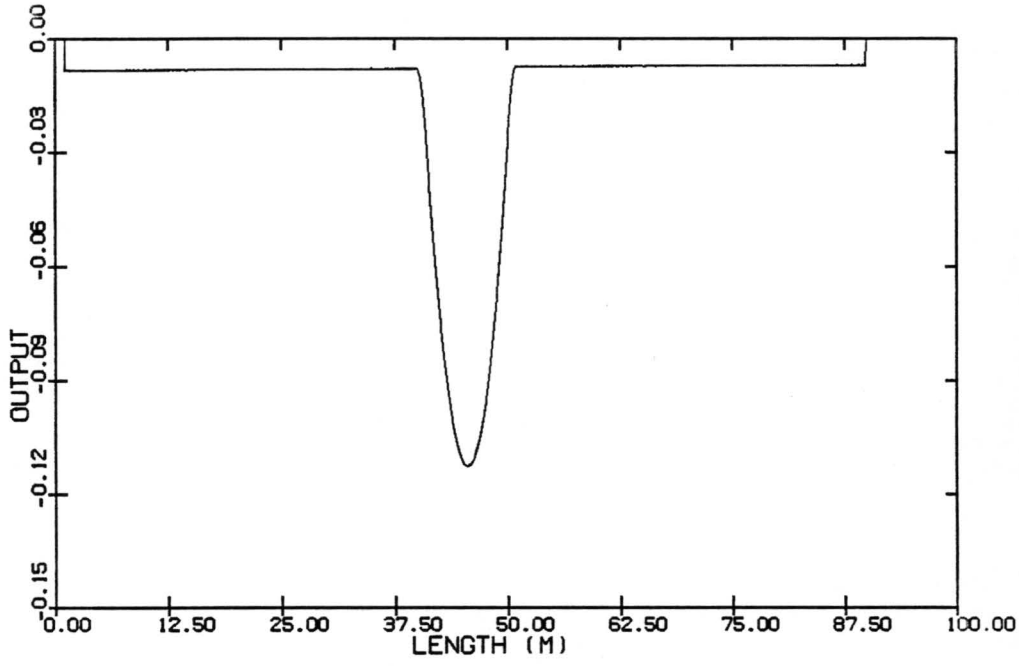

Figure 3.36: 1st Derivative of Continuous Strain Distribution

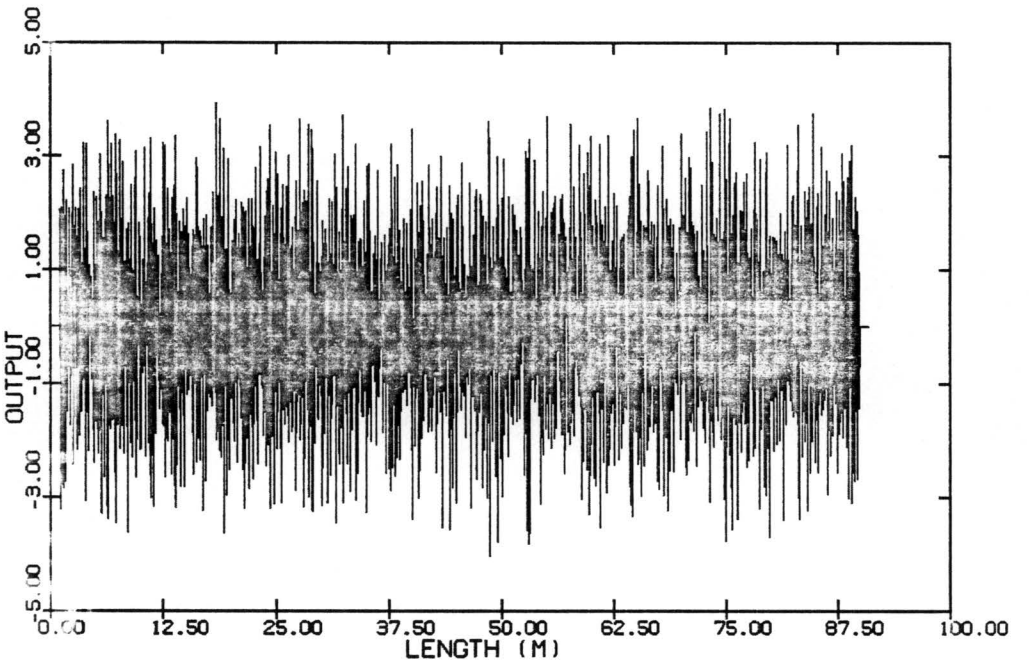

Figure 3.37: 1st Derivative of Signal Containing Noise

As an example, the synthesis of 25 waveforms, each similar to that in Figure 3.31, can be seen in Figure 3.38, as well as the first derivative of the synthesis. While it is apparent that 25 samples is quite sufficient to obtain a smooth OTDR profile, the slope of the data barely shows the expected dip centered at 45m. The outputs from a similar computation for 150 and 250 averaged waveforms appear in Figure 3.39 and Figure 3.40, respectively. Again, the resolution of the backscattered wave is insignificantly increased, but the first derivative is noticeably enhanced. It should be noted however, that while this practice of digital smoothing is frequently carried out in actual situations, the time necessary to perform the computations limits the systems ability to gather and process dynamic data.

3.6 CONCLUSIONS

The imbedding of optical fibers in composite materials has been proposed as a method for nondestructive evaluation of the host composite. Transmission or no transmission of light through an imbedded fiber can be used as a simple break monitor, while OTDR in the imbedded fiber potentially provides both position and amplitude information about a perturbing force.

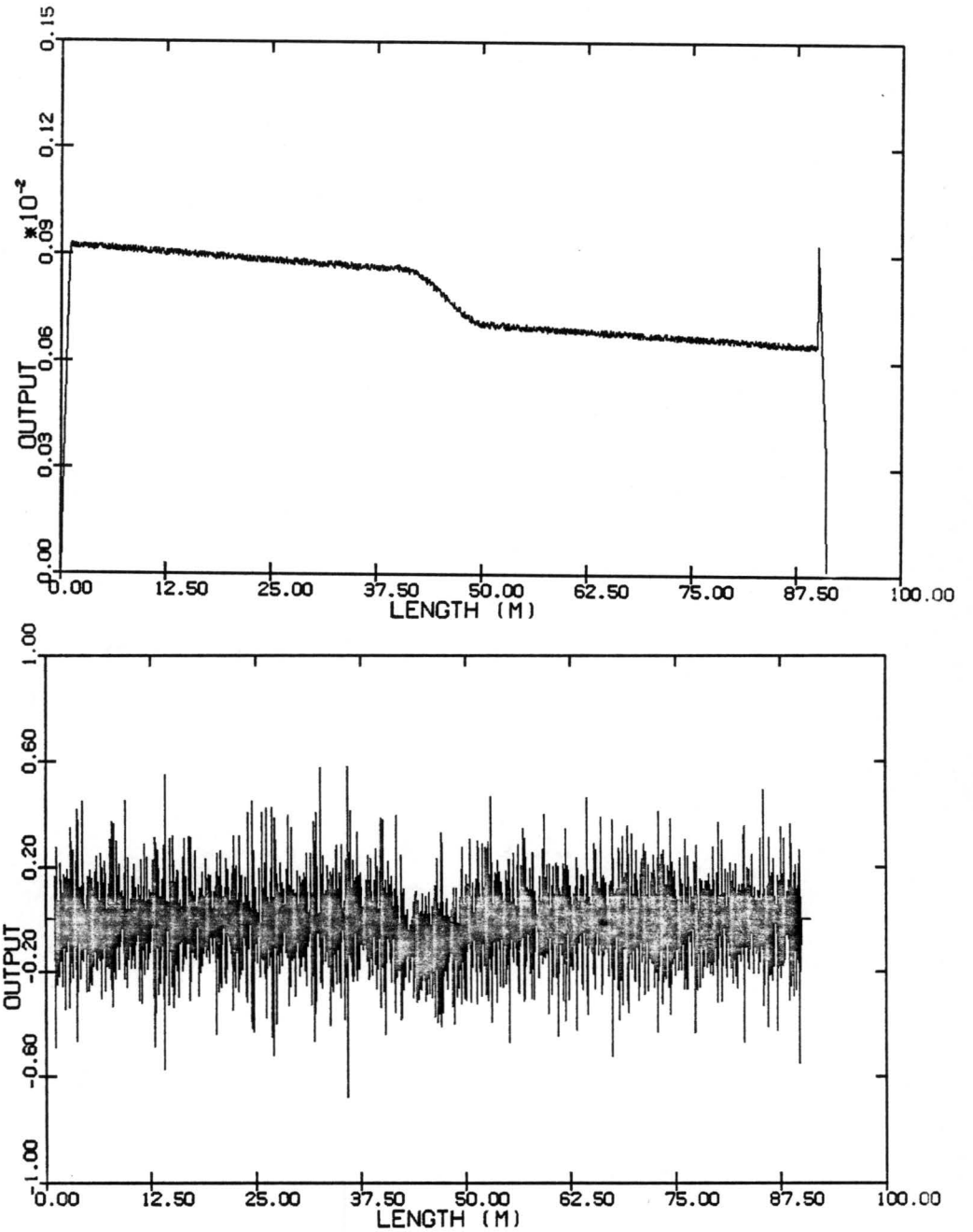

Figure 3.38: Signal Averaged 25 Times and Associated Slope

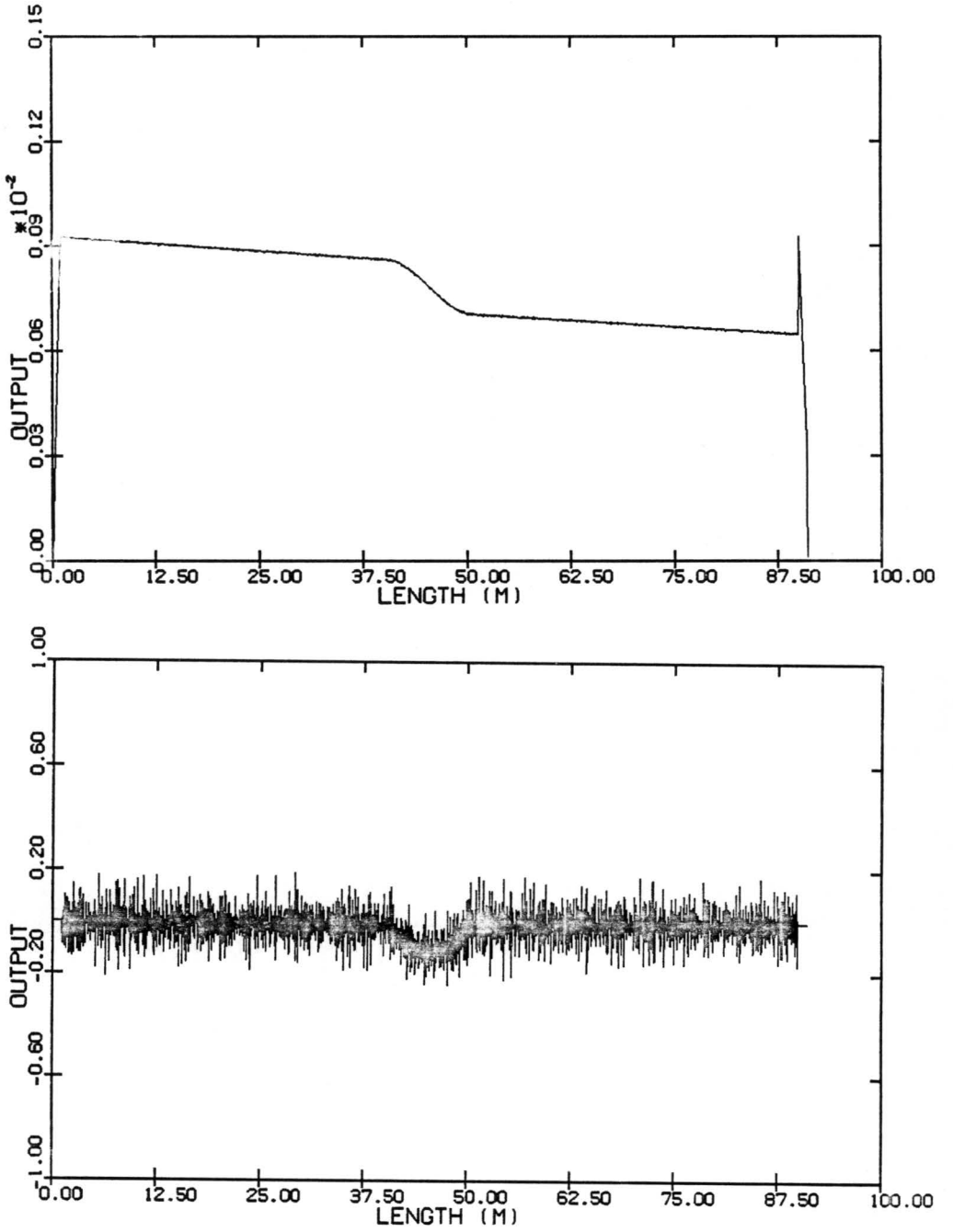

Figure 3.39: Signal Averaged 150 Times and Associated Slope

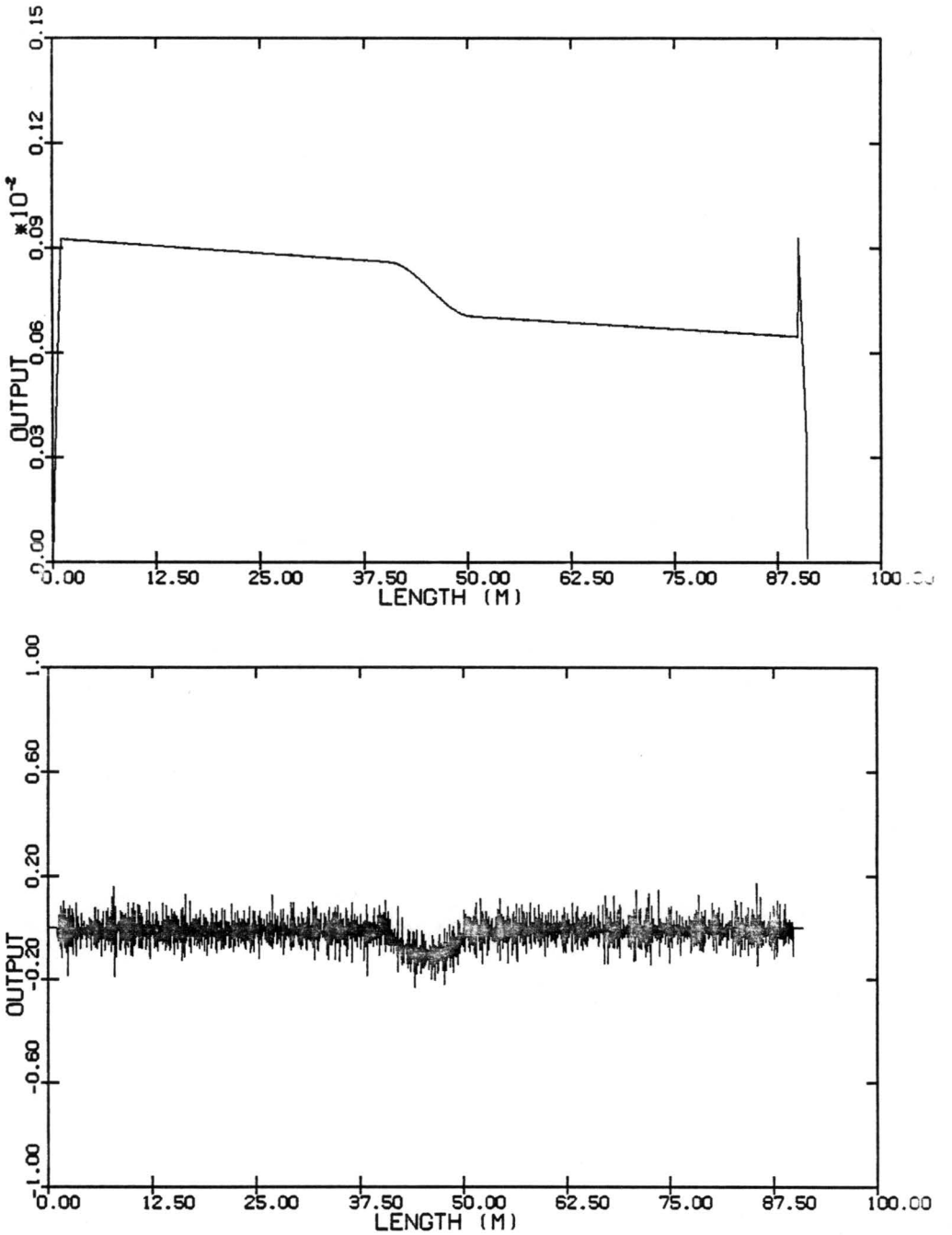

Figure 3.40: Signal Averaged 250 Times and Associated Slope

Fundamental properties of the test method, such as the position resolution and the dynamic range, can be calculated directly for a given system. However, at this point, relatively little is known about the complex optical/mechanical interaction between the optical fiber, the fiber jacket, the epoxy matrix, and the composite fibers. In addition, few quantitative tests have been performed to determine how the introduction of an optical fiber would affect the mechanical integrity of the composite sample.

The tests proposed and carried out to answer some of these questions were met with only limited success. The main reason for this is thought to be unfamiliarity with appropriate test procedures. Thus, while not as much as hoped was learned from the tests, a basic knowledge was gained regarding sample fabrication and test procedures, as well as some mechanical properties of fibers in composites. Also, the computer simulation of the OTDR concept, and the associated slope program, both served to stimulate the understanding of the proposed method, in addition to being potentially useful signal processing aids. Perhaps most importantly, the many issues involved in this effort were clearly isolated, providing direction for future efforts.

Chapter IV

SENSOR DESIGNS - CONCEPTS AND MEASUREMENTS

Because optical fiber sensor technology is still young, many relatively simple concepts remain to be proven, and a host of applications have yet to be realized. This of course gives the field an air of excitement and expectation: countless meaningful experiments and useful devices can be conceived, built, and tested with ease, relative to some other technologies. In this chapter, just a few of the many ideas and preliminary measurements which have arisen during the course of this research will be presented.

In the first section, the effects of microbending are further discussed, and the data for some early experiments are reported. The second section presents the design for a fiber optic-based position encoder, while the third section reports a passive, wavelength division multiplexing scheme for use with fiber optic sensor arrays. In the fourth section, the design for an optical chopper for both general and fiber optic applications is presented, and its merits considered. Most of the work discussed in this chapter was developed in cooperation with the Inland Motor, Fiber Optic Systems Laboratory in Radford, Virginia.

4.1 MICROBENDING ANALYSIS

Using microbending effects in fiber optic sensor design was mentioned in Chapter 2, and formed the foundation of the method discussed in Chapter 3. In this section, a slightly more thorough, although by no means complete, treatment of microbending will be presented. After several paragraphs of background information, the results of two bending experiments are reported. The use of concentric core optical fiber in microbending sensors is discussed next, while the concluding section contains a first design of a microbending test assembly.

4.1.1 Background

In the last thirteen years, a plethora of theoretical analysis has emerged regarding the effects of microbending in optical fibers, notably from several authors at Bell Telephone Laboratories [66 - 71]. However, empirical studies have been difficult to correlate to the theories, partly because the theories disagree from each other at points, and because certain assumptions were made at various points in their formulation for the sake of simplification. Therefore, efforts at constructing practical microbend sensors usually do not rely heavily on theoretical results.

Most experimental data presented in the literature concentrates on the microbending characteristics in a particular case, aimed at a particular application. Despite the need, until recently, few quantitative results attempted to address microbending in general terms. An important exception was work done by Fields, who appears to have been the first to present data on loss as a function of the deformation period, Λ [72]. His results, reproduced in Figure 4.1, show a strong peak for parabolic index fiber, and step-like curve for step index fiber. This observation is attributed to the coherent mode-coupling process predicted by theory for a system having uniform mode spacing and critical deformation period of

$$\Lambda_c = 2\pi a/\sqrt{2\Delta}.$$

Here a is the fiber core radius and Δ is the maximum relative index difference between core (at the fiber axis) and cladding of the fiber.

This result is now well known, and has been confirmed by several researchers [11, 73, 74]. In one case, it is shown that for a nearly sine-shaped deformation such as seen in Figure 4.2a, having periodicity $n\Lambda_c$ (n=2,3,...), a similar optical loss peak occurs as with Λ_c. This is substantiated by the author's findings, shown in Figure 4.2b.

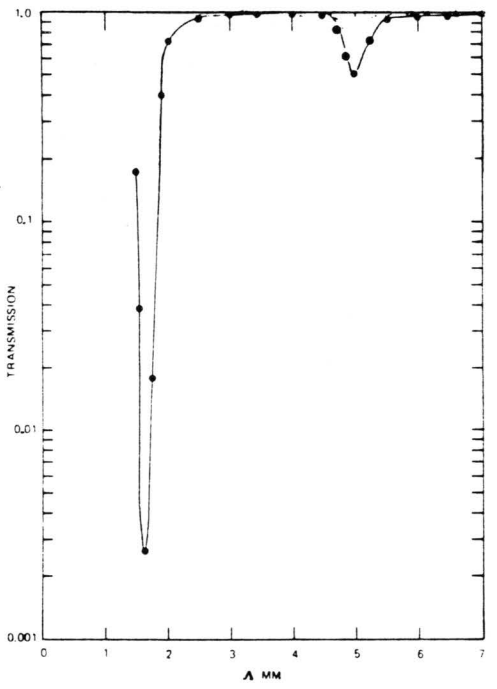

(a) Transmission of the parobolic-profile fiber.

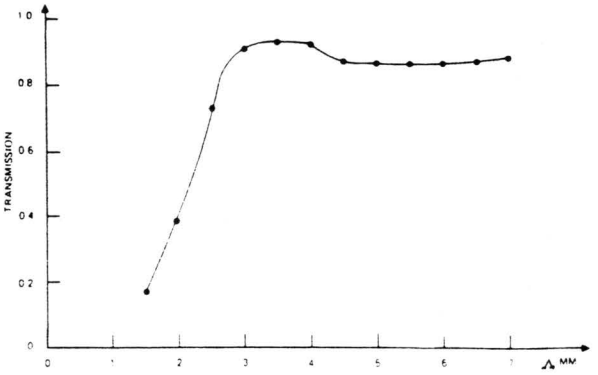

(b) Transmission of the step-profile fiber.

Figure 4.1: Microbending Transmission Dependence on Distortion Period (after [72])

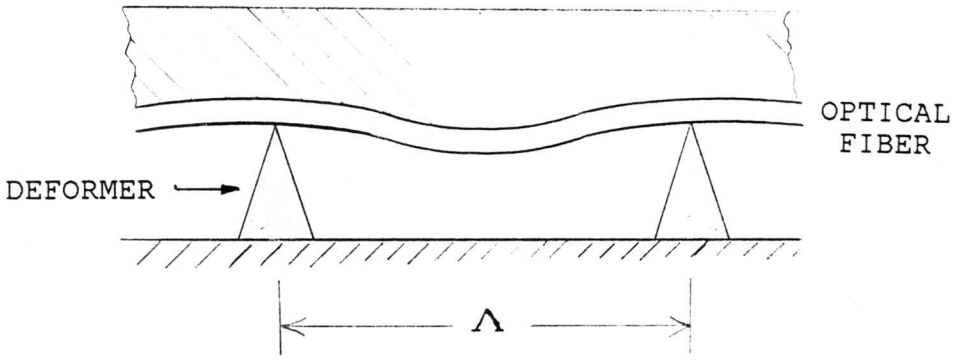

(a)

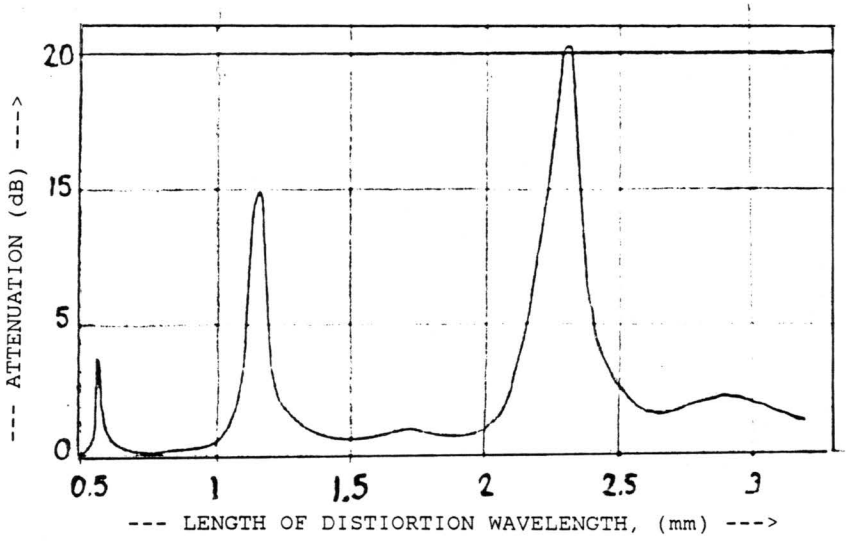

(b)

Figure 4.2: Microbending Attenuation Dependence on Distortion Period (after [74])

In addition to the deformation periodicity, it is rather obvious that the deformation amplitude contributes to the microbending loss. This forms the basis upon which most bending sensors rest. As will be shown, the loss response to amplitude is generally nonlinear, but for multimode fibers, it is at least monotonic.

Another parameter which plays an important role in microbend sensors is the radius of curvature of the fiber. In most theoretical approaches, the fiber is assigned the shape of a sinusoid of known period and amplitude, which thus fixes the bending radius. In practical terms, however, this shape is difficult to achieve, and now is rarely attempted. Rather, an approach such as previously shown in Figure 4.2a is usually taken. In this case, the shape can be described by

$$EI(\partial^4 y/\partial^4 x) = -Cy \qquad (4.2)$$

where E is the Young's modulus and I is the moment of inertia of the fiber, and C is a constant depending on the elasticity of the surrounding medium [74].

4.1.2 A First Experiment

In this section, an early demonstration of microbending pressure sensitivity is reported. Though somewhat elementary, it was instructive in showing what trends in data to ex-

pect, as well as what kind of problems might arise. The experiment also generated several questions which would need to be answered before practical sensors could be reliably built.

A quick demonstration of bending loss is often accomplished by pressing the fiber into a hole tapped in the optical bench. An attempt to quantify this observation was made using the set-up of Figure 4.3a. A Corning graded index Fiber with a thin polymeric buffer was laid across a washer, and rigidly fixed about one inch on either side of it. A plunger loaded with known weights pressed the fiber into the washer, bending it at the inside corners of the washer and the bottom corners of the plunger. Laser light was injected into the fiber using a roughly NA-matching microscope objective lens.

Only nominal control was gained as to exactly where the plunger touched down, rendering the actual fiber deformation uncertain. Configurations such as pictured in Figure 4.3b were all observed. As many as nine measurements were taken and averaged to determine each point, applying first the plunger and then the weight. An attempt was made to center the plunger each time, especially if the plunger-only response did not return to the set level.

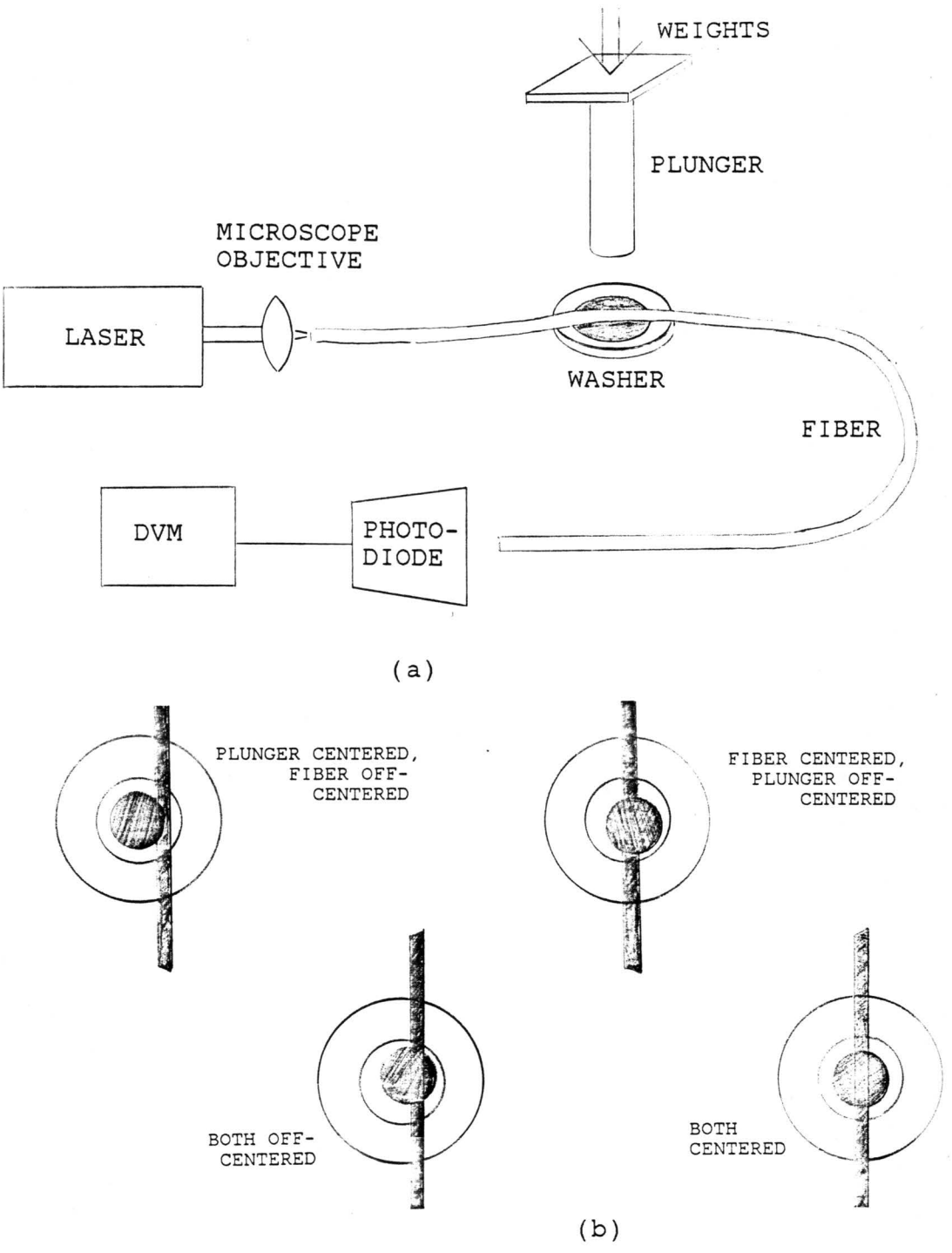

Figure 4.3: Layout and Configurations for the First Experiment

Figure 4.4 shows the resulting transmitted signal versus applied load. The loss in decibels versus applied load appears in Figure 4.5. Clearly the response is nonlinear, as expected from theory. However, despite the relative crudeness of the experiment, and with little effort to optimize the effect, measurable sensitivity to a 5 gram bending weight was observed with tolerable SNR.

It was concluded that while microbending is easily observed and even calibrated, optimization of the effect requires a) more understanding of the stress-strain parameters of the fiber, b) more control of the mechanical aspects of the sensor, and c) the "proper" choice of optical fiber. This was later found to have been expressed by Giallorenzi, *et al*, in terms of a modulation index,

$$Q = (dT/dx)/(dx/dp) \qquad (4.3)$$

Here, T is the fiber transmission and x is the amount of fiber deformation, and p is the bending pressure applied [4].

The first term in (4.3) depends on the intrinsic sensitivity of the optical fiber to microbending losses. Since this can change from fiber to fiber, depending on design, a knowledge of the opto-mechanical relationship for various fibers is crucial. The second term of (4.3) shows the modulation index dependence on the degree of deformation resulting from a given pressure. Clearly this is a function of

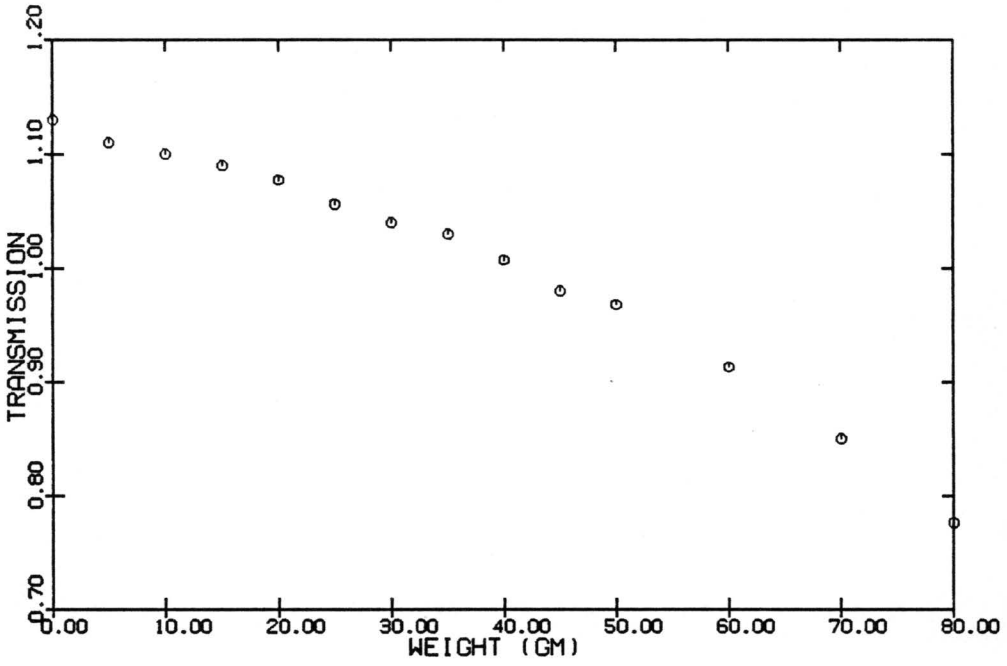

Figure 4.4: Transmitted Intensity versus Applied Weight

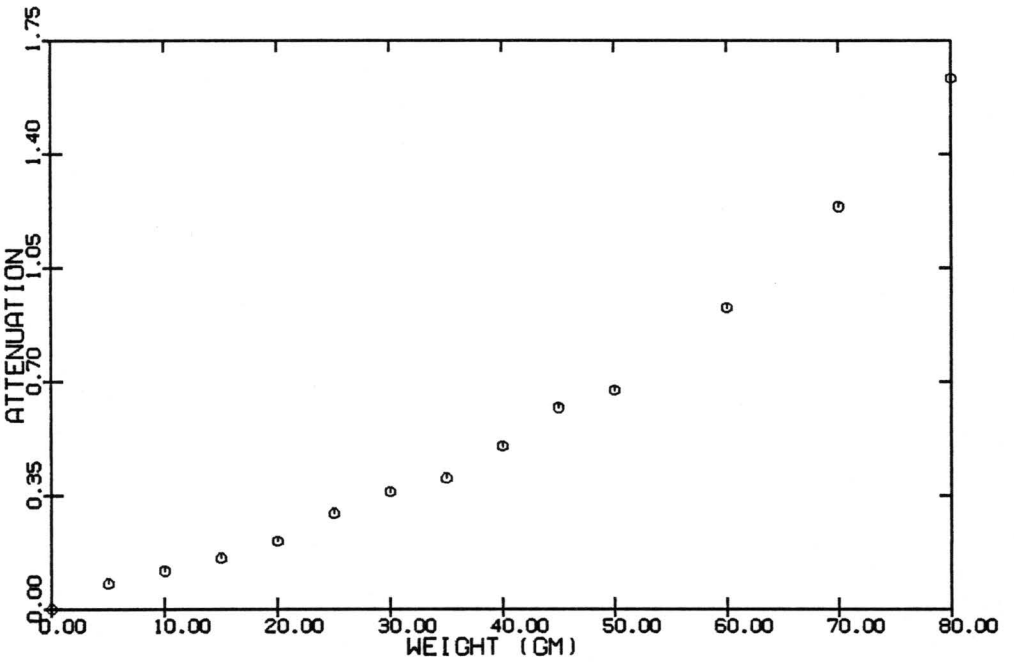

Figure 4.5: Attenuation in dB versus Applied Weight

the mechanical design of the sensor. Lagakos, *et al*, formulated this expression in terms of C_m, the mechanical compliance of the sensors, generally itself a complex function of the Young's modulus of the fiber, the bending period, the number of deformations, the fiber diameter, etc. [11]. The suspected need to better understand these parameters in each system is thus demonstrated.

4.1.3 A Second Experiment

In this section, an experiment initiated to examine constant-curvature bends is reported. The effects due to both the curvature radius and the degree of bend were isolated by means of a cylindrical rod whose diameter varied in steps, as shown in Figure 4.6. The same figure also shows the bending diameter when the fiber geometry is taken into account. The remainder of the set-up is only slightly more complex than in the previous experiment, as evident from Figure 4.7.

As before, light was launched into a Corning fiber with an NA-matching lens. After several meters of fiber, so that the modes were presumably scrambled enough to approximate equal mode power distribution, the fiber was firmly fixed on an elevated platform. From there the fiber was turned one, two, three, or four full turns around the rod at a given di-

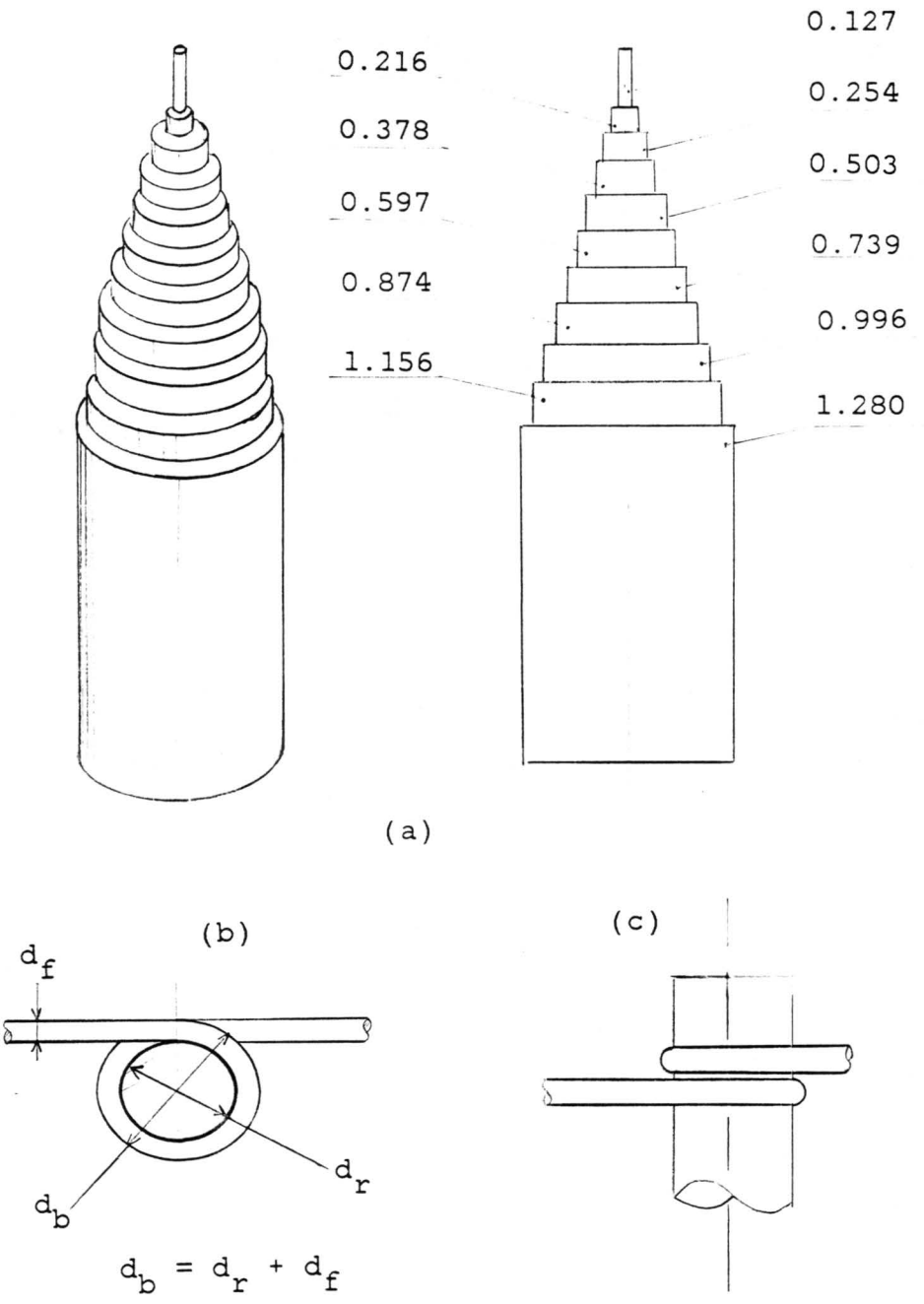

Figure 4.6: The Amplitude/Bending Radius Experiment, Bending Rod

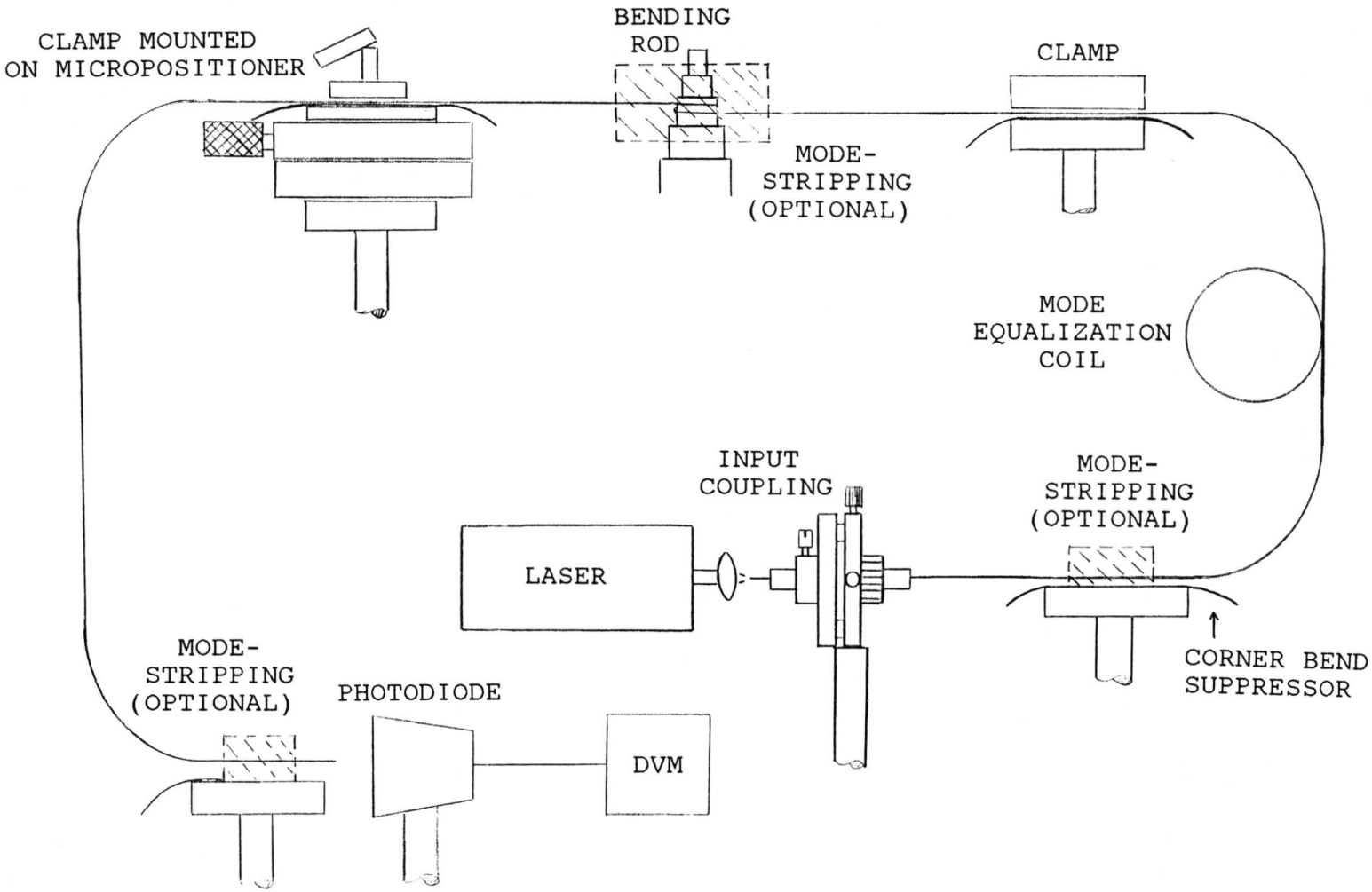

Figure 4.7: Amplitude/Bending Radius Experimental Setup

ameter, and clamped to a micropositioner stage. This allowed the tension on the fiber to be carefully increased until it was taut, but not significantly strained. Finally, the light output was detected by a large-area photodiode and displayed without amplification by a digital voltmeter.

The results of these measurements appear in the next two figures. In Figure 4.8, the transmitted intensity is plotted against the bending radius. The four curves correspond to the four cases of one, two, three, or four turns around the rod. The alternate way of displaying the data emphasizes the light output dependence on the number of turns. These curves, one for each bending radius, appear in Figure 4.9.

Some salient features of the experiment are as follows. First, no attempt was made to pursue the mode stripping options. This was partly done for convenience, and also because past experiments show that often little is gained by stripping at either end of this fiber. Probably stripping at the bending rod would produce significant effect, though mechanical solidity is sacrificed. That is, when the fiber jacket was removed, bending radii below about 0.5 cm were unattainable; the unprotected fiber would break. Despite these difficulties, the measurements will need to be repeated with stripping included.

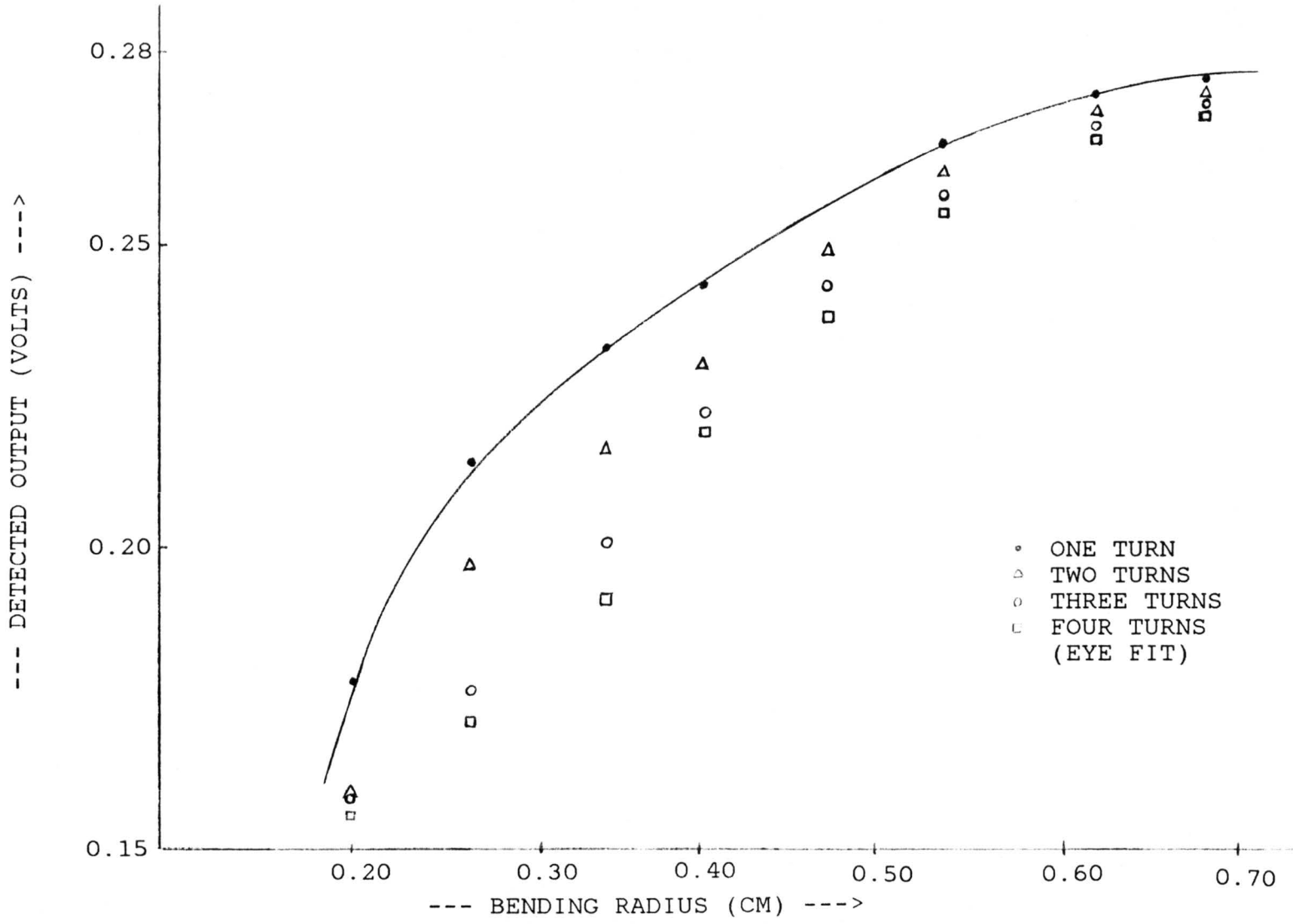

Figure 4.8: Optical Signal versus Fiber Bending Radius

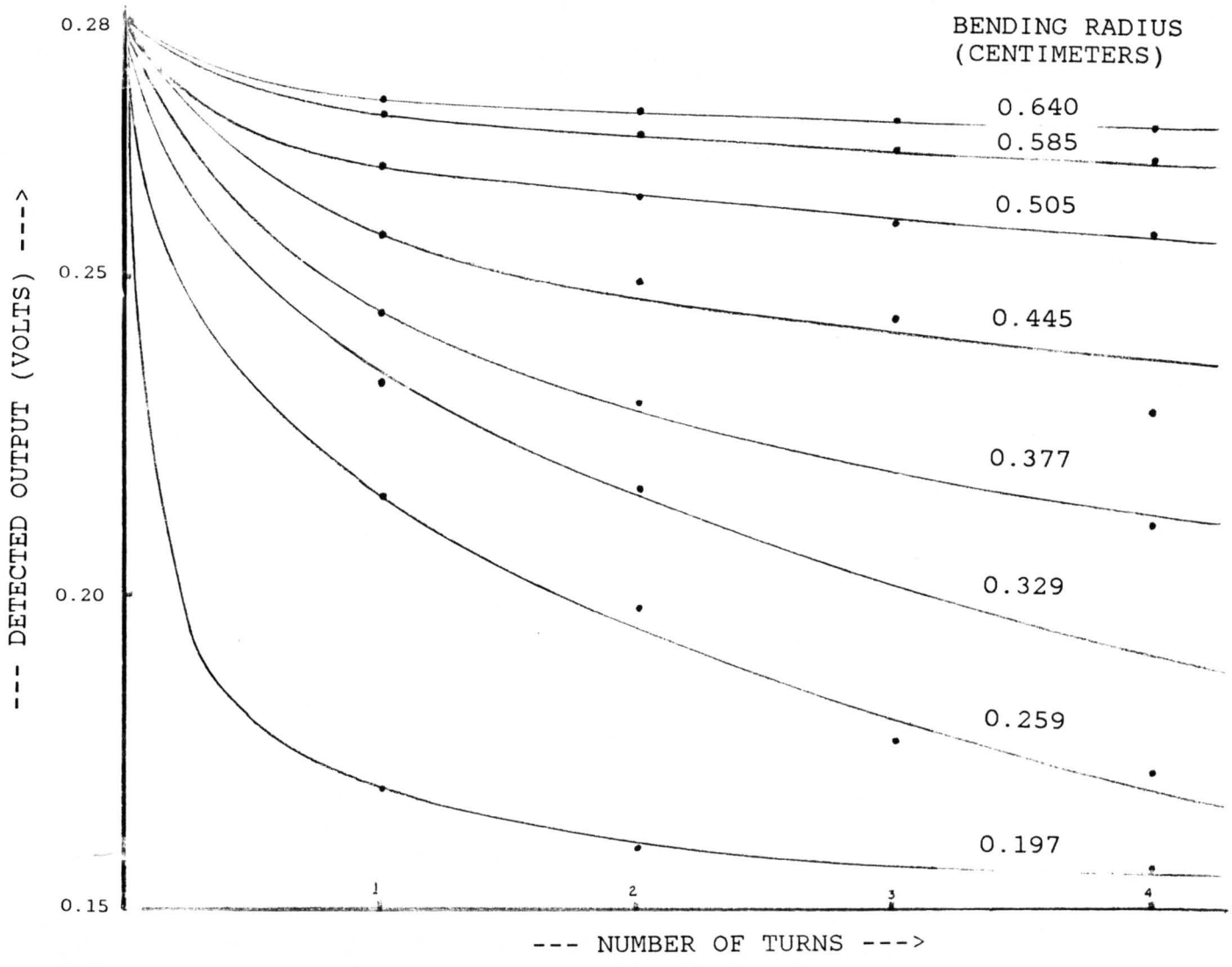

Figure 4.9: Detected Optical Signal versus the Number of Turns

It is interesting to note that the minimum obtainable bending radius for the jacketed fiber was 0.197 cm. However, this point of failure came after all the larger radii points, each with one to four turns, were measured. Also, in preliminary attempts, the fiber was seen to withstand radii of 0.127 cm with what appeared to be full recovery. These facts together confirm earlier suspicions that sizeable fatigue is experienced by fibers when subject to repeated bending. The extent to which this has been observed and documented is unknown, but it is potentially of great importance, especially where long term, full range cyclic operation of a microbending sensor is expected.

Second, the exact shape of the helical winding around the rod seemed to play a large part in the light output. In order to be consistent, the coils of fiber were always wrapped tightly against one another, as seen in Figure 4.6c. Also, care was taken to ensure that no sharp bends were introduced along the path of the fiber. In this case, the transmitted signal was generally quite stable, after an unexplained period of several seconds of settling down.

Finally, although no theoretical analysis was formulated for this exact bending geometry, it seems that the trends displayed by this experimental data are both real and repeatable. Furthermore, when time permits, theoretical treat-

ment should not be tremendously difficult since the fiber totally conformed to a simple, known geometry. Thus it is suspected that the fiber parameters such as the Young's modulus would not take an important role in the analysis.

4.1.4 Sensing with Concentric Core Optical Fiber

Concentric core optical fiber is suggested for use in microbending sensors. It has been observed that interesting and predictable far-field patterns result when concentric core fiber undergoes both sharp bending and axial strain. However, the full analysis of the loss mechanisms has not yet been completed.

A cross-section of the index profile for a typical concentric core fiber is pictured in Figure 4.10a. The inner core generally consists of a single index (step) raised above a depressed inner cladding. The index of the outer core generally lies slightly below that of the inner core, but above the cladding [75].

When laser light is lensed so as to inject it only into the outer core, a clearly identifiable output pattern results similar to the output of a normal multimode fiber. If, however, the fiber experiences a severe bend along its length, light is both scattered and mode-converted, giving rise to a broader radiation pattern. This pattern consists

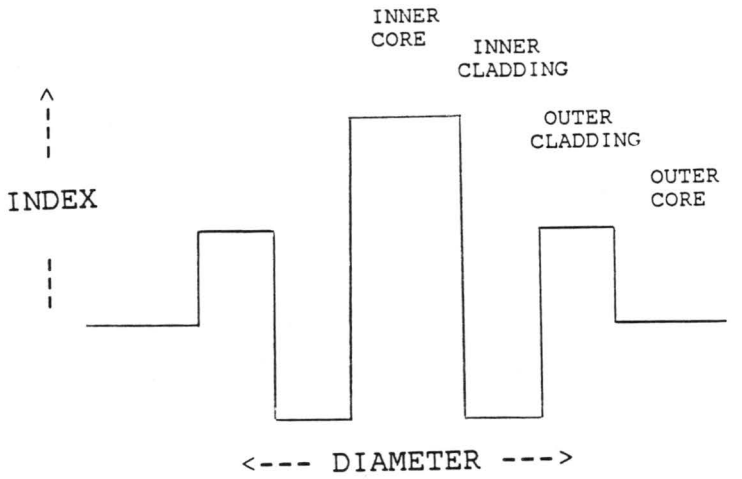

(a)

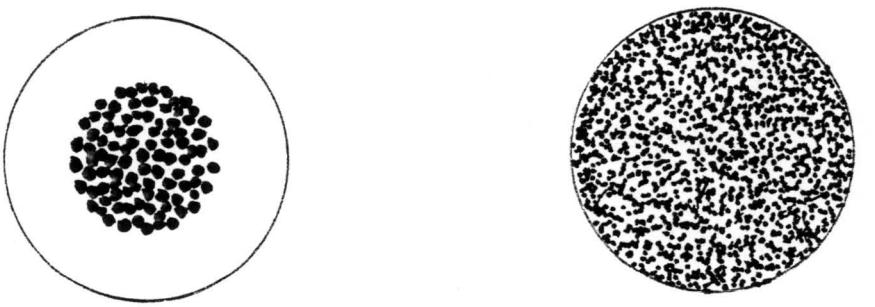

(b)

Figure 4.10: Concentric Core Fiber Index Profile and Far Field Pattern

of well-contained inner cladding modes, as well as the original inner core modes with decreased intensity. If the fiber length is short from the bend to the detector, the total power in the second case differs little from that of the first. Both these cases are sketched in Figure 4.10b.

The use of concentric core fiber for sensor applications displays two major advantages with respect to conventional graded index fiber. First, instead of relying on light *loss* as the sensing mechanisms, these new sensors depend on the effects of light *redistribution*. A similar idea has been pursued by Meltz, *et al*, whereby a fiber containing two cores, side by side in a single cladding, was made sensitive to temperature and pressure changes [76]. In their sensor, it was core cross-talk due to evanescent wave coupling which inferred bulk fiber changes. In this case however, light redistribution is caused by conventional radiative effects due to bending or scattering effects due to local refractive index differences.

The second main advantage of concentric core sensors is that they are ideally suited for use with a self-referencing detection scheme. That is, suppose that a two segment detector is fabricated in the form of a bull's eye pattern; the signal registered from the inner segment will be termed A, while that from the outer, ring-shaped segment is refer-

red to as B. The geometry can be arranged so that in the unperturbed state, A is at a maximum, while B is zero. As pressure-induced bending occurs, A drops, while B correspondingly increases.

The two signals are then processed electronically to yield (A-B)/(A+B). By referencing the difference signal with the sum signal, the system can tolerate uniform power fluctuations, say due to fiber misalignments, laser variations or degradation due to dirt entering the system. Thus this scheme displays a relatively high SNR, while retaining reasonable sensitivity.

An ideal representation of the signals, the sum, the difference, and their ratio is illustrated in the left column of Figure 4.11. Here, the transmission from both channels is represented as linear functions of the microbending perturbation. That is, the outputs, Y_A and Y_B can be written as

$$Y_A = m_1X + b_1 \qquad \text{and} \qquad Y_B = m_1X + b_1 \tag{4.4}$$

The difference term is then

$$Y_A - Y_B = (m_1 - m_2)Y_A + (b_1 - b_2) \tag{4.5}$$

while the sum term is

$$Y_A + Y_B = (m_1 + m_2)Y_A + (b_1 + b_2) \tag{4.6}$$

The final output is simply the quotient of these two expressions.

Now suppose that both Y_A and Y_B suffer a 50% degradation, such as seen in the two upper right graphs of Figure 4.11. Then

$$Y_A - Y_B = (1/2)(m_1 - m_2)Y_A + (b_1 - b_2) \tag{4.7}$$

and

$$Y_A + Y_B = (1/2)(m_1 + m_2)Y_A + (b_1 + b_2) \tag{4.8}$$

Clearly the quotient of these expressions exactly matches that of the undegraded case.

Of course neither detector response is actually expected to be linear, and the sum and difference quotient is only linear for special transmission function combinations. However, linearization of the final signal seems possible, given a judicious choice of superimposed gain functions. For example, if the output signal O is electronically modified to yield

$$O = (aA - bB)/(cA + dB) \tag{4.9}$$

where a, b, c, and d are variable gain terms which depend on A and B, nonlinearities might be overcome.

An attempt to measure the bending loss of a jacketed concentric core fiber was made. The fiber was bent around a single pin of radius 1.5 mm and loaded with a constant tension throughout the experiment. Two discrete photodiodes were positioned side by side, and their outputs were sent to the sum and difference circuit seen Figure 4.12. In this case the variable gains were all set to unity.

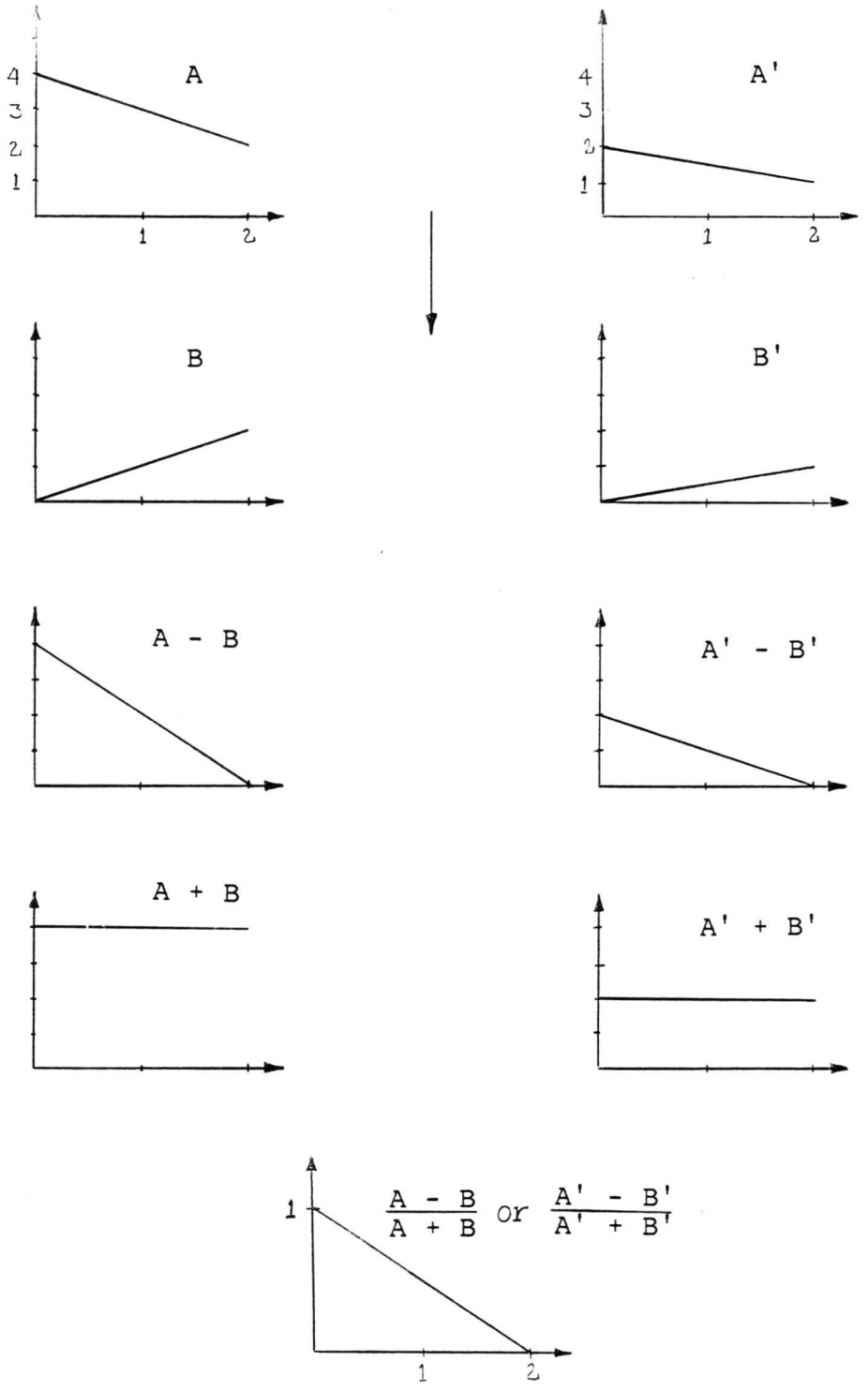

Figure 4.11: Demonstrating Immunity to Uniform Degradation

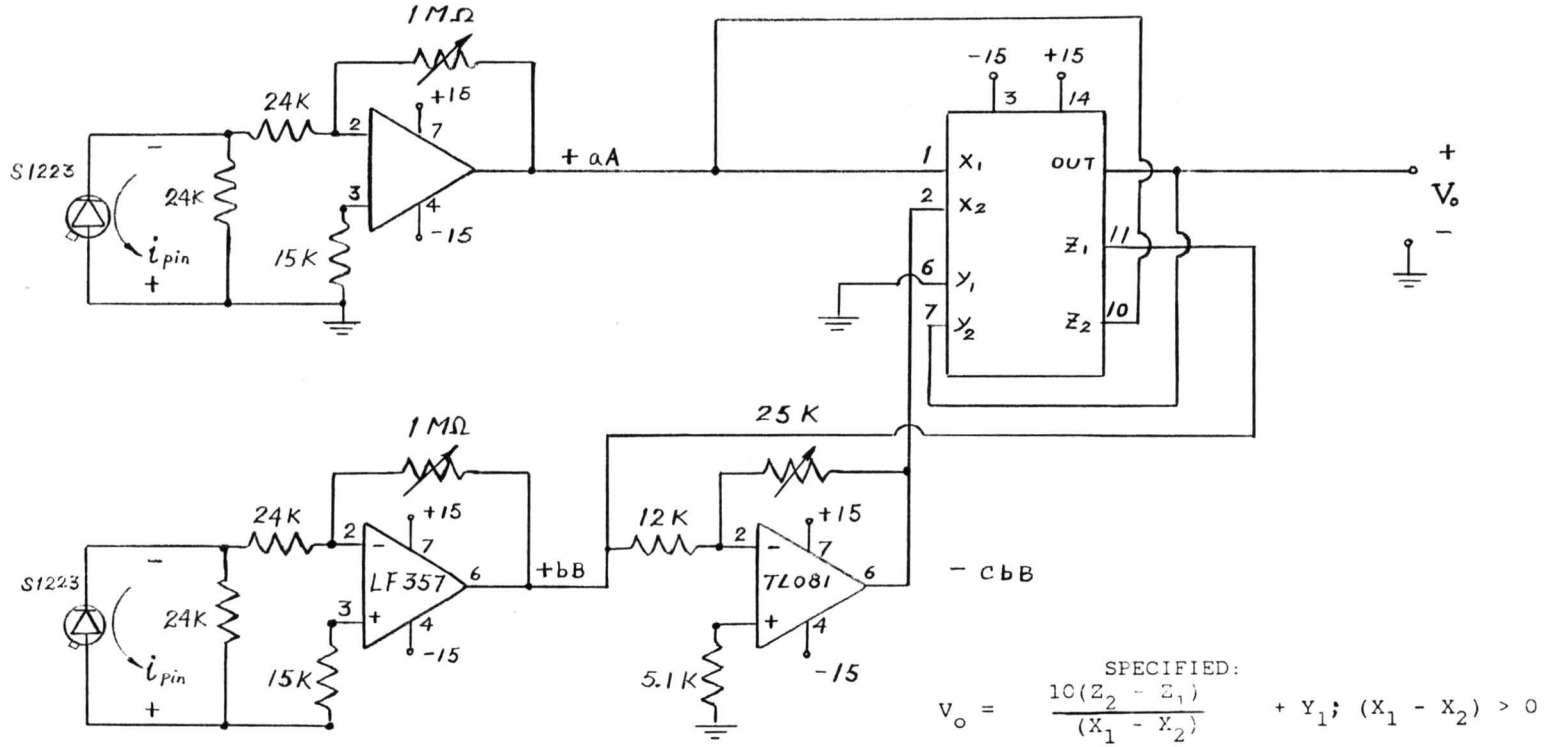

SPECIFIED:

$$V_o = \frac{10(Z_2 - Z_1)}{(X_1 - X_2)} + Y_1; \ (X_1 - X_2) > 0$$

HERE:

$$V_o = \frac{10(aA - bB)}{(aA + cbB)} + 0 \qquad \text{with } a,b = 10,\ c = 1$$

$$V_o = \frac{10(A - B)}{(A + B)}$$

Figure 4.12: Sum and Difference Circuit Using a Multiplier IC

The results of the measurement were rather inconclusive. Little if any signal change was observed for bending angles up to 90 degrees. It was determined that the bending radius was still too large to cause marked radiation loss. In addition, the processing circuit suffered from relatively large noise fluctuations, presumably due to the stacking of low performance amplifiers. Continuing efforts to analyze the theoretical properties of the fiber, as well as reformulate empirical studies, are underway.

4.1.5 A Bending Testing Assembly

From Equation (4.2), it can be seen that in many situations it is necessary to first determine the mechanical constants of the system, and then solve a differential equation to be able to describe the bending shape for a given amplitude. The situation can be simplified considerably if instead, the fiber is caused to completely conform to a structure whose shape is easily analyzed. If the deformer is properly designed, it should be possible to decouple the effects on bending loss due to period, amplitude, and radius curvature.

One of the first bending sensors to depart from the conventional corrugated plate design is described by Marvin and Ives [12]. It consists of a fiber threaded through a roller

chain, which forces it into a series of arcs of constant curvature connected by straight line segments, as seen in Figure 4.13. The main disadvantage of this scheme from a research point of view is its inflexibility; the radius of curvature is fixed, and the amplitude and period can not be changed independently.

The initial design of a more versatile bending test assembly has been completed. An overview of the apparatus is pictured in Figure 4.14. A brief description of its operation follows.

At the heart of the design are the bending pins. It was noticed early on that the sharper the bend in a fiber, the more loss it displayed. Thus it was decided to make a bending pin having four different curvature radii, as shown Figure 4.15, in order to test the loss dependence on curvature. After the flats are milled on the pin corners, a constant curvature can be approached by sanding the remaining edges with fine grit paper. The resulting corners are far sharper than could be obtained from practical cylindrical pins.

The pins are each mounted in a holder, and each holder in the main yoke. The distance between holders can be varied to alter the bending period, and the pins can be rotated in the holders to alter the radius curvature. The holders are clamped in place by turning screws against retaining shim

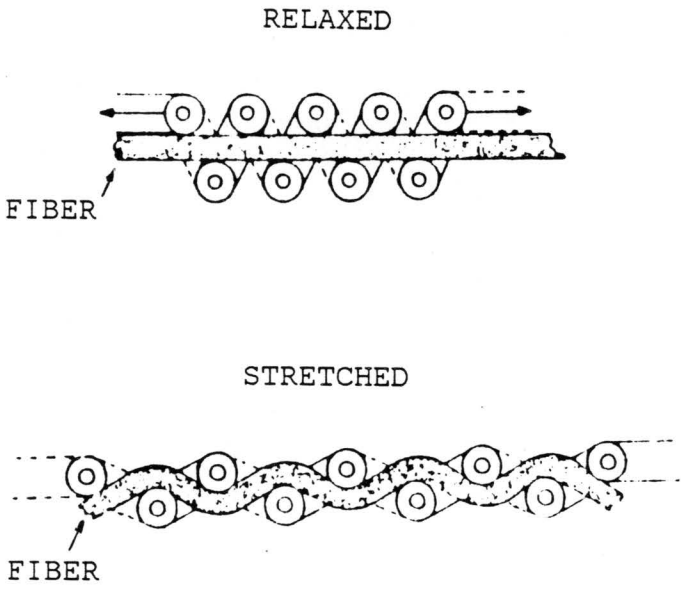

Figure 4.13: Roller Chain/Fiber Arrangement and Geometrical Analysis (after [12])

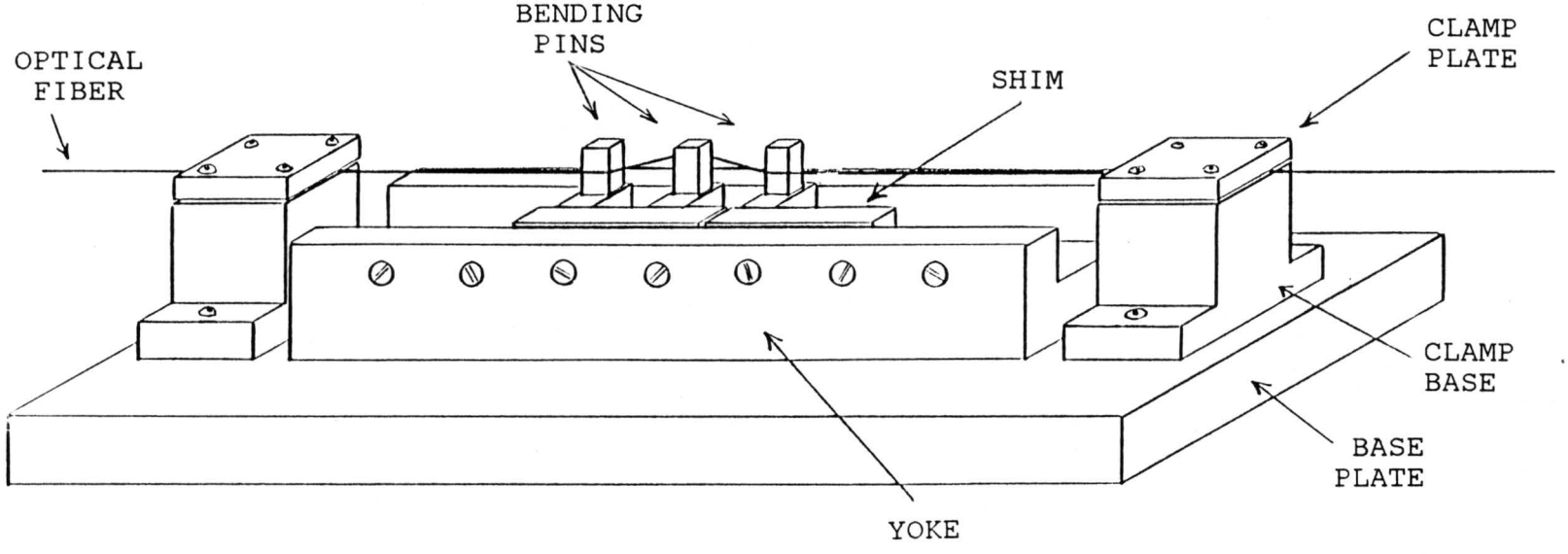

Figure 4.14: Optical Fiber Bending Assembly

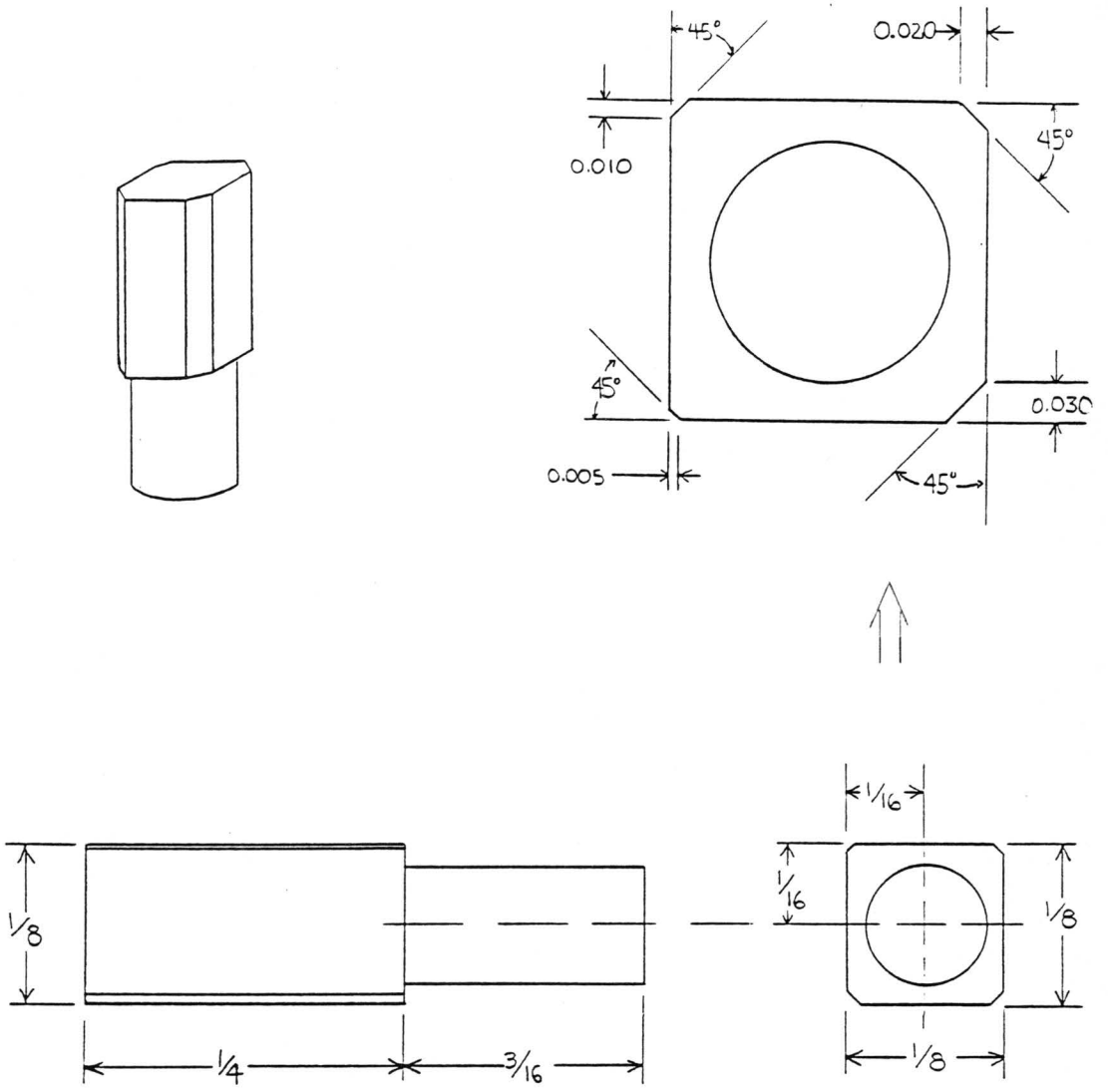

Figure 4.15: The Bending Pin Specifications

material. The amplitude of the bending can be altered by rotating holders with respect to each other as shown in Figure 4.16. Further variation can be obtained by changing the thickness and placement of smaller pieces shim. It should be noted that 90 degree bends are the maximum possible with the design.

Finally, the fiber is strung between the pins, pulled taut, and clamped. The assembly shown can accommodate up to 21 pins. Also, the clamping surfaces are to be provided with rubber padding to protect the fiber. Detailed drawings of the components appear in Appendix 3.

Since the time it was drawn, the design has undergone revision. For example, the far superior clamping fixture seen in Figure 4.7 has been decided upon. Also as in that set-up, the clamp should be mounted on a translation stage in order to be able to vary the fiber tension. It is further suggested that the pins merely be mounted as desired in a plate drilled in pegboard fashion. Though having certain disadvantages compared to this initial design, this would be quick and easy to fabricate.

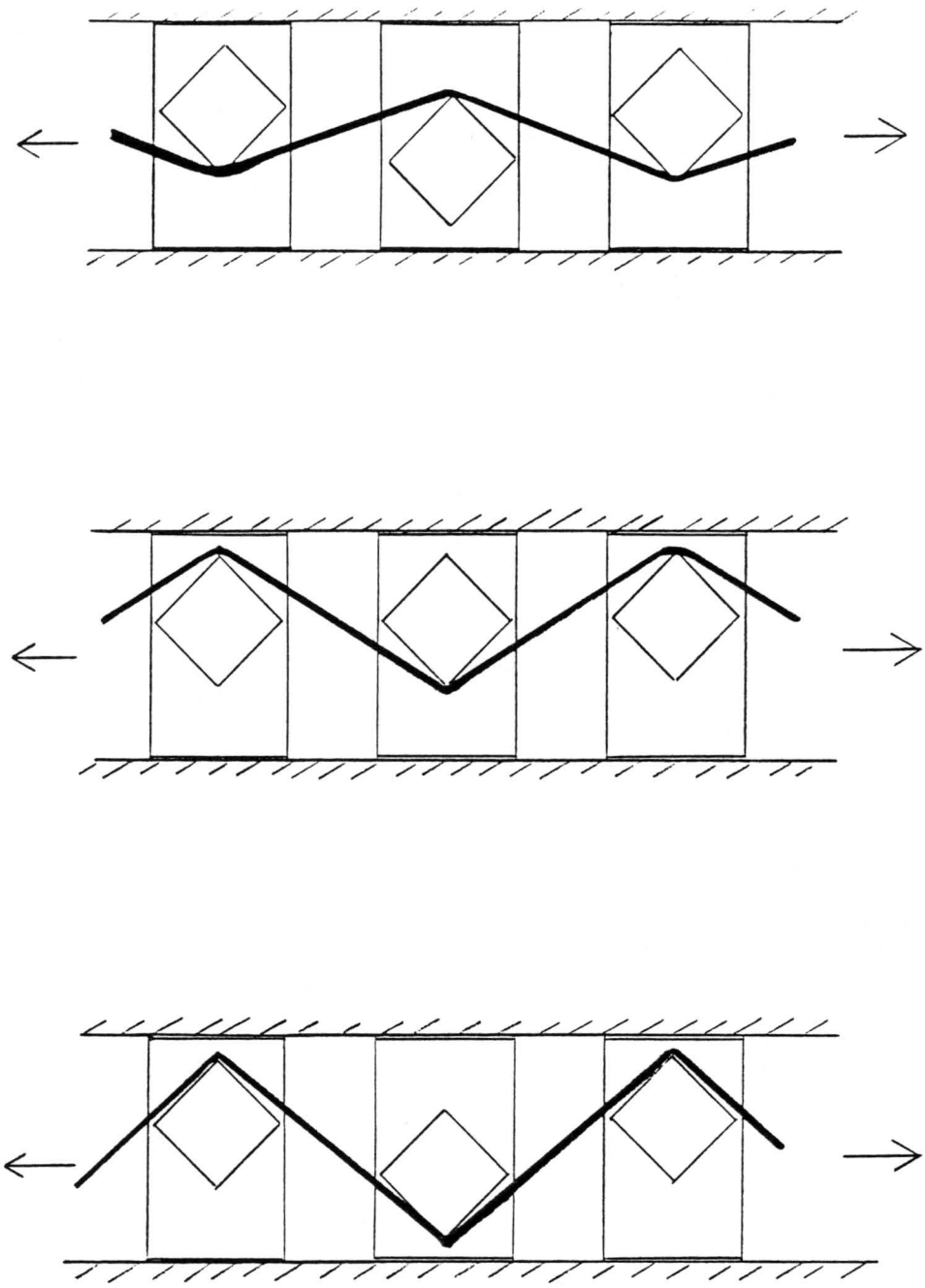

Figure 4.16: Some Immediate Bending Amplitude Possibilities

4.1.6 Conclusions

Though microbending sensors have been carefully studied by many authors, by no means is the field incapable of yielding new treasures to the serious hunter. In particular, correlation of experimental results with theoretical hypothesis has been only partially successful, and deserves more investigation. As well, new fiber types having more complicated index profiles are being fabricated. Many of these may prove most useful for sensor applications, though even preliminary tests and calculations have not been attempted in many cases.

Of primary interest is the ability to isolate microbending contributions due to the radius of curvature, the degree of bend, and the bending periodicity. The second experiment discussed above, as well as the bending test assembly presently being built, both represents attempts in that direction. This area of bending research will likely be the focus of future efforts. In addition, the use of concentric core fiber shows promise for use in sensitive and noise immune sensors.

4.2 DUAL BEAM FIBER OPTIC ENCODER

Position encoders which are insensitive to both EMI and mechanical noise sources are desired, especially for use in military environments. Also desired are encoders having high resolution, but which are opto-mechanically simple and have low parts counts. This section describes a general position encoder designed to meet these needs. The system is based on dual beam referencing through a continuous code plate. A computer simulation of the sensor provides the expected output waveshapes for various situations.

4.2.1 Background

Absolute position encoders operate in either a continuous fashion or in discrete steps. Discrete step encoders have the advantage of yielding binary outputs which are compatible with digital logic circuitry. An optical gray-coded wheel provides an example of such an encoder. Discrete encoders suffer the disadvantage of being limited in resolution, and requiring separate circuitry for each bit. The number of code bands directly determines both the number of positions that can be resolved and the complexity of the device.

Continuous encoders give an analog signal, the amplitude of which is a function of position. In optical technology,

such encoders are based on neutral density filters which vary their transmissions as a function of linear position or angle. Typically, an emitter-detector pair placed on either side of a continuous code plate or wheel can be used to monitor the position or rotation. If only a single pair is used, the system is susceptible to various types of non-random noise arising from misalignments or unwanted beam interruptions. Emitter-detector pairs are also prone to electromagnetic interference (EMI) when not fully shielded. Figure 4.17 depicts the basic layout of both the linear and the rotary encoder.

4.2.2 Description

For the sake of argument, consider a continuous code wheel used to measure rotational displacement. A thin film of opaque material is deposited on the surface of a glass wheel in such a way as to vary the transmission as a function of angle. The industry standard for film material is Inconel, an alloy of cobalt, indium, and iron, primarily chosen for its resilience and high reflectivity at typically employed wavelengths.

The electronic components necessary for light generation and sensor monitoring are housed in a shielded box remote from the code wheel, while light is piped to and from the

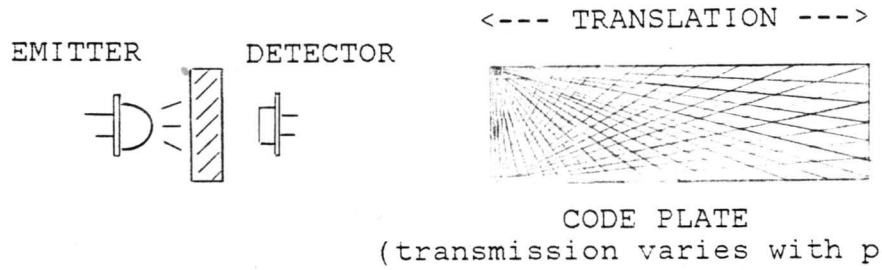

(a) LINEAR, CONTINUOUS

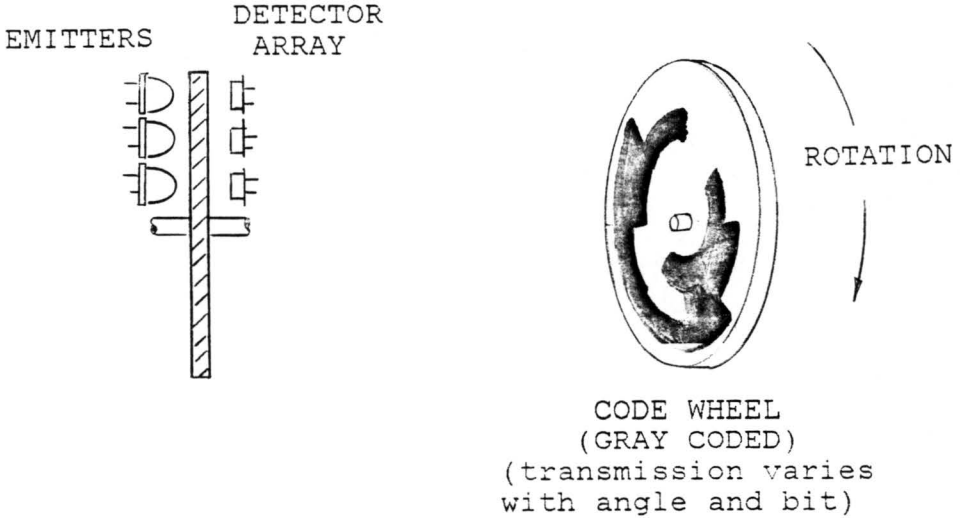

(b) ROTARY, BINARY

Figure 4.17: The Basic Linear and Rotary Encoder System Layout

wheel via optical fibers. This alleviates the EMI susceptibility of the transmission lines. At least two sending fibers, and most likely two additional return fibers are required.

Next, the fibers are lensed using graded index (GRIN) lenses which focus the light on the code disc. By placing similar lenses on the opposite side with their focal points at the wheel, the light can be fully collected and injected into the return fibers. Resolution of the wheel position is then theoretically limited to the beam waist diameter at the focal point. In one formulation, this is given by

$$d_o \approx \pi 1.22 df/2\lambda \qquad (4.10)$$

where d_o is the waist diameter, d is the lens diameter, f is the focal length of the lens and λ is the radiation wavelength. For the components used, this number is on the order of 0.06 μm, which is generally smaller than inclusions and other particle deformations in the film deposition. If this is the case, defocusing the beam or collimating can easily be accomplished to average over the beam area.

Reduction of opto-mechanical noise sensitivity is accomplished by means of the dual beam, sum and difference technique introduced in the last section. Two beams, located 180 degrees apart, traverse the wheel as described above. Each channel, again called A and B, is detected separately

and then signal processed to output (A-B)/(A+B). As before, this self-referencing format means that if transmission is degraded in either or both channels, the output signal suffers less amplitude loss and distortion than the signal through a single (unreferenced), degraded channel. In some cases, a single line degradation translates to a dc offset in the output signal rather than a signal distortion. If both lines are subject to the same attenuation, as is often the case, the output signal shows no change. This provides for a constant SNR over a wide operating range. The basic outline of this approach appears in Figure 4.18.

It was originally conceived that the above discussion would apply in full to a reflective scheme as well. Such a sensor would utilize a wheel whose reflectance varied with angle, and would employ directional couplers or beamsplitters to both send and receive the light on the same fiber. Upon closer examination however, it was determined that, due to the film deposition particulars, a surface whose reflectance varies predictably with position is difficult to realize [77]. This has been confirmed by experiment.

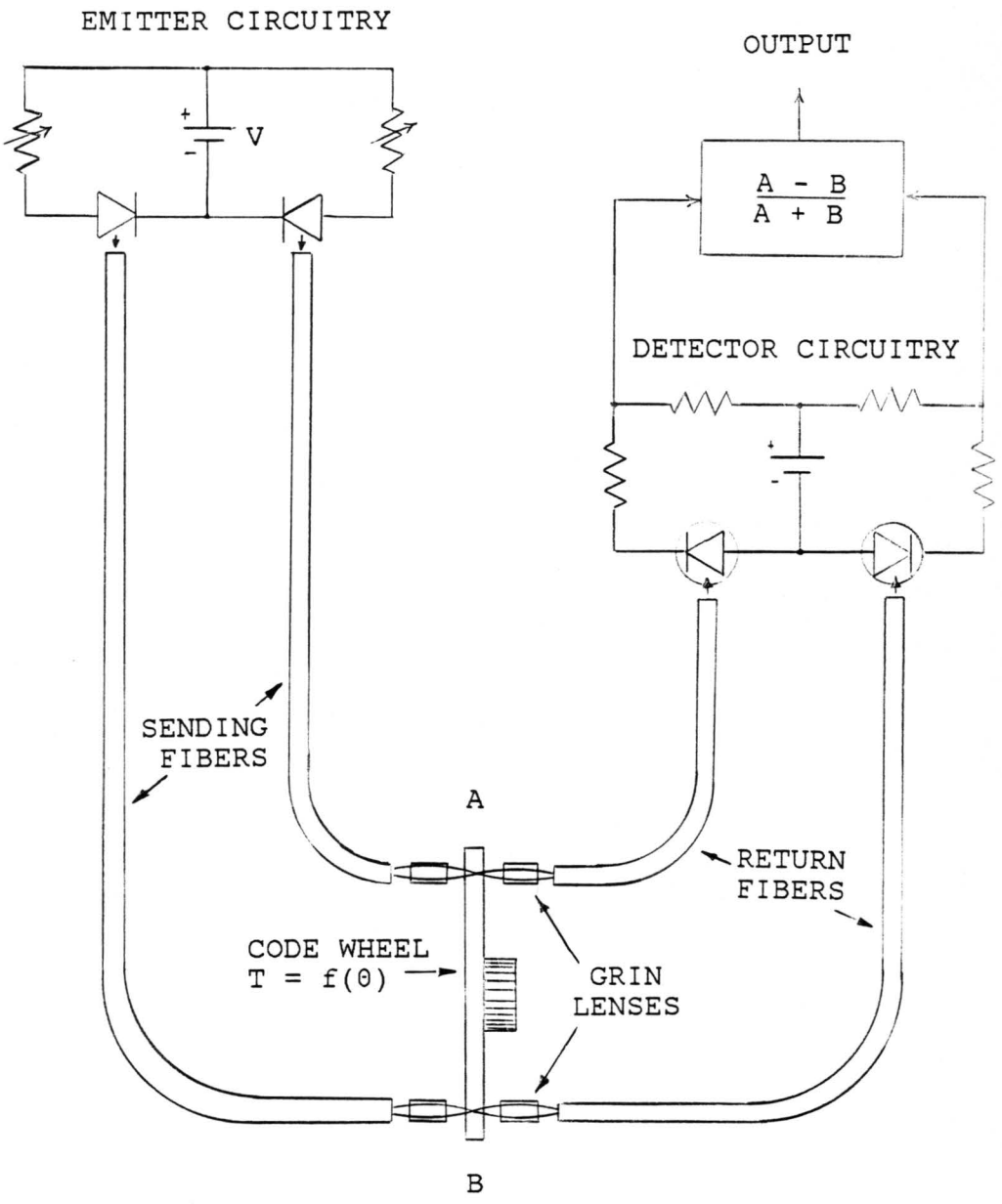

Figure 4.18: Schematic of the Dual Beam Encoder

4.2.3 Analysis

The expected signal output shape depends on two factors: the angular position of the two beams with respect to one another, and the code wheel transmission, T, as a function of angle, θ. Figure 4.19 shows the expected signal output when T is a linear function of θ and the angular difference between lines A and B is 180 degrees. When the angle is changed to 90 degrees, the asymmetric plot of Figure 4.20 results. Figure 4.21 shows a two-piece, linear transmission function and its corresponding linear signal output, assuming a 180 degree separation.

Suppose for a moment that the transmission of the previous figure is employed, and that the wheel has rotated 90 degrees from zero (1.57 radians). From the figure, an output of 0.50 units is expected if a single, unreferenced channel is used, and zero units if the dual beam system is used. If the signals returned from both channels are decreased by the same amounts (as is likely for certain types of perturbations), the sum and difference processor yields an output which is completely unchanged.

If only a single channel is degraded by a factor of 50%, say because of dirt or misalignment, the curves of Figure 4.22 result. Obviously the signal in the single channel is now half of the expected value. Because of the slope of the

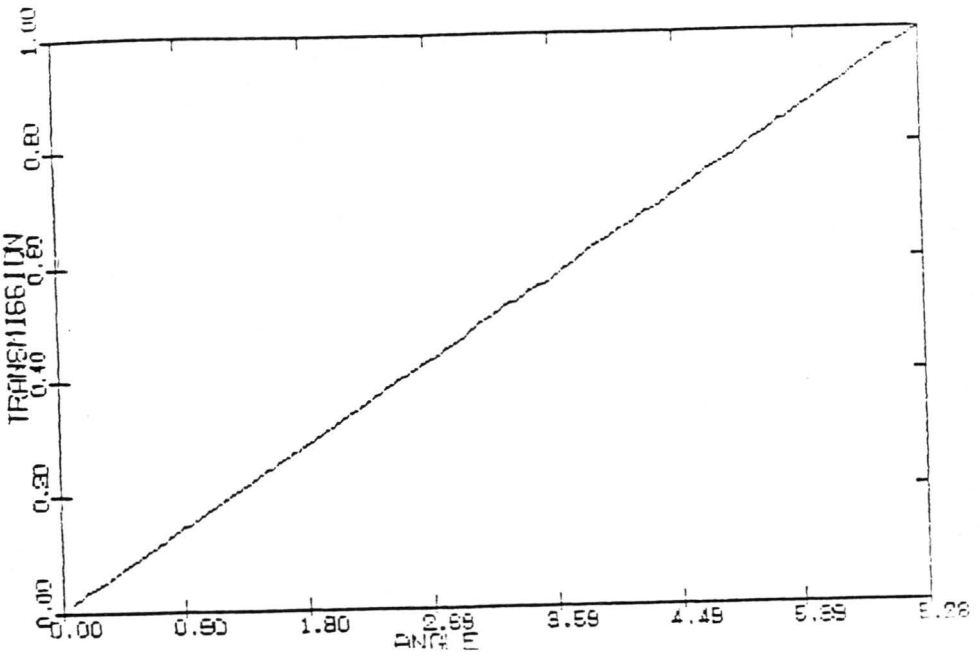

(a) Normalized Transmission vs. Angle (in Radians)

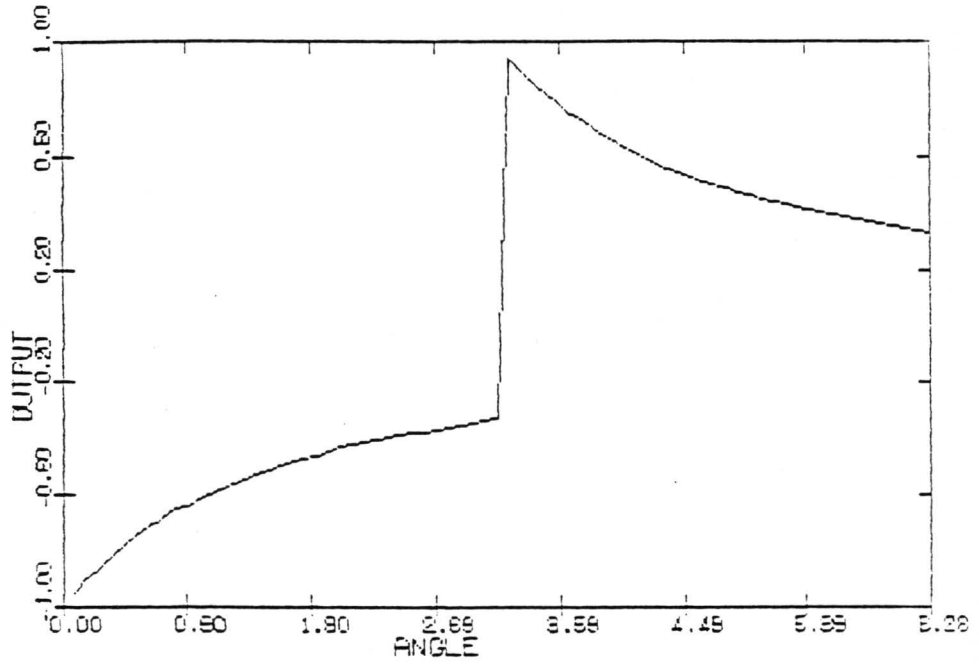

(b) Normalized Signal Output vs. Angle (in Radians)

Figure 4.19: Linear Transmission and Corresponding Output

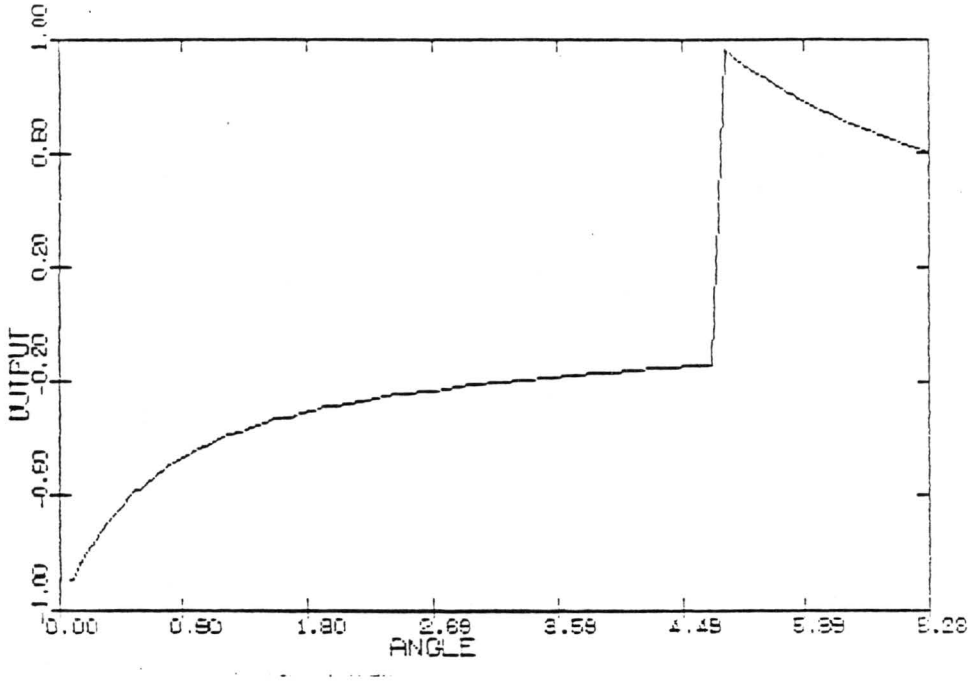

Figure 4.20: Asymmetric Signal Output for 90 Degree Beam Separation

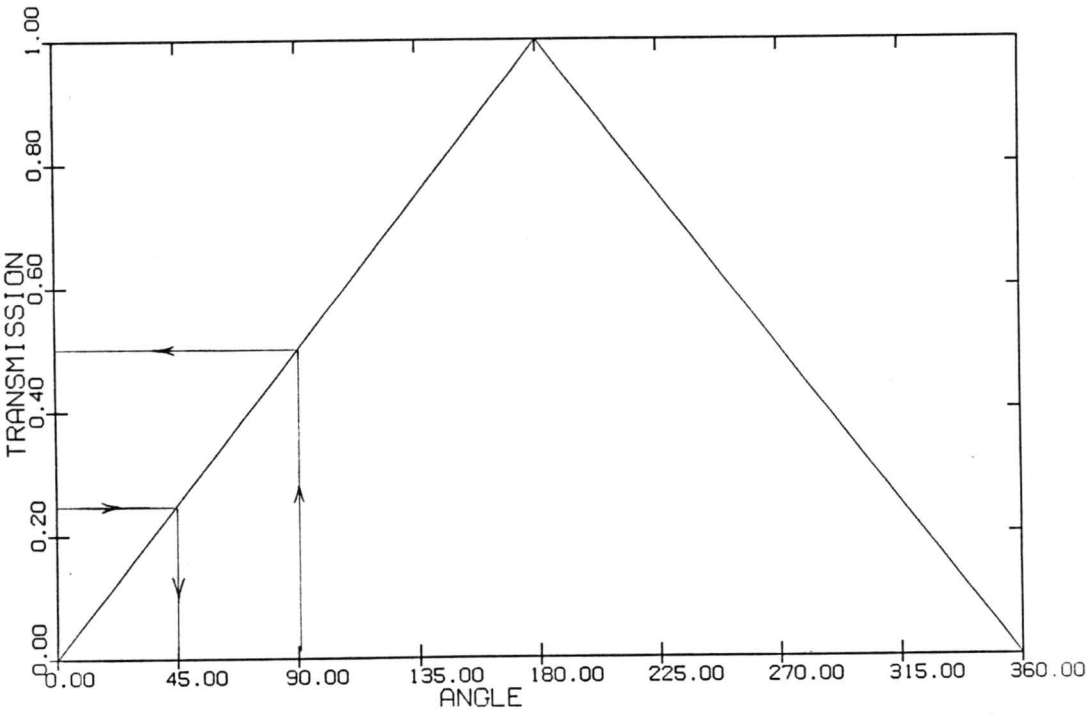

(a) Normalized Transmission vs. Angle (in Radians)

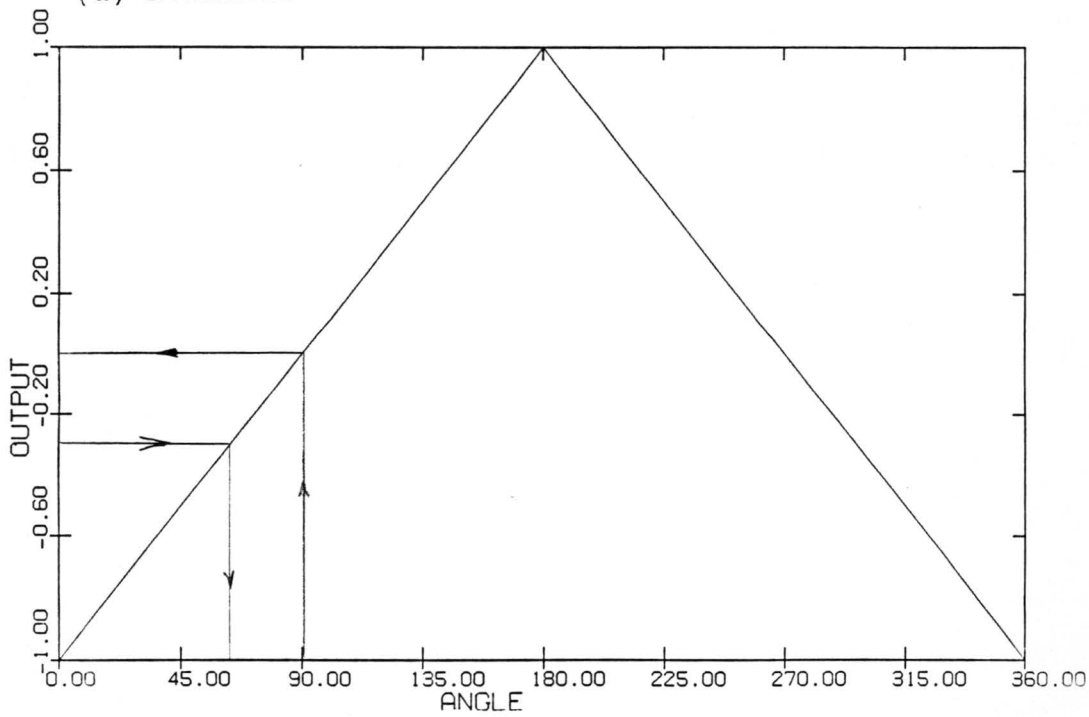

(b) Normalized Signal Output vs. Angle (in Radians)

Figure 4.21: Two-Piece Transmission and Corresponding Output

calibration curve (Figure 4.21a), the electronics indicate that the wheel position is half of what it really is, or 45 degrees; that is, the system shows 50% error.

In contrast, the dual beam curves yield an indicated angle of 60 degrees, an error of 33%. A plot of indicated angle error versus angle would be useful, though a plot of the difference between Figures 4.21b and 4.22b can give a general idea of the error trend, as seen in Figure 4.23. The fact that the output difference is a function of wheel angle is expected because of the nonlinear relationship of Figure 4.22b. The computer code used to generate these curves appear in Appendix 4.

It should be noted that by manipulating the geometry of the fiber lines, as well as the angular transmission function, an infinite number of signal waveforms is possible. The choice of function would clearly depend upon the specific application. One disadvantage of this scheme with respect to the single line system is the need for twice as many fibers, emitters, and detectors (or splitting optics). Another disadvantage can be understood by considering that if only the single line format were used, the wheel would be coded with a transmission curve such as Figure 4.19a. Being monotonic, one output infers one and only one angular position. On the other hand, with the dual beam system, the

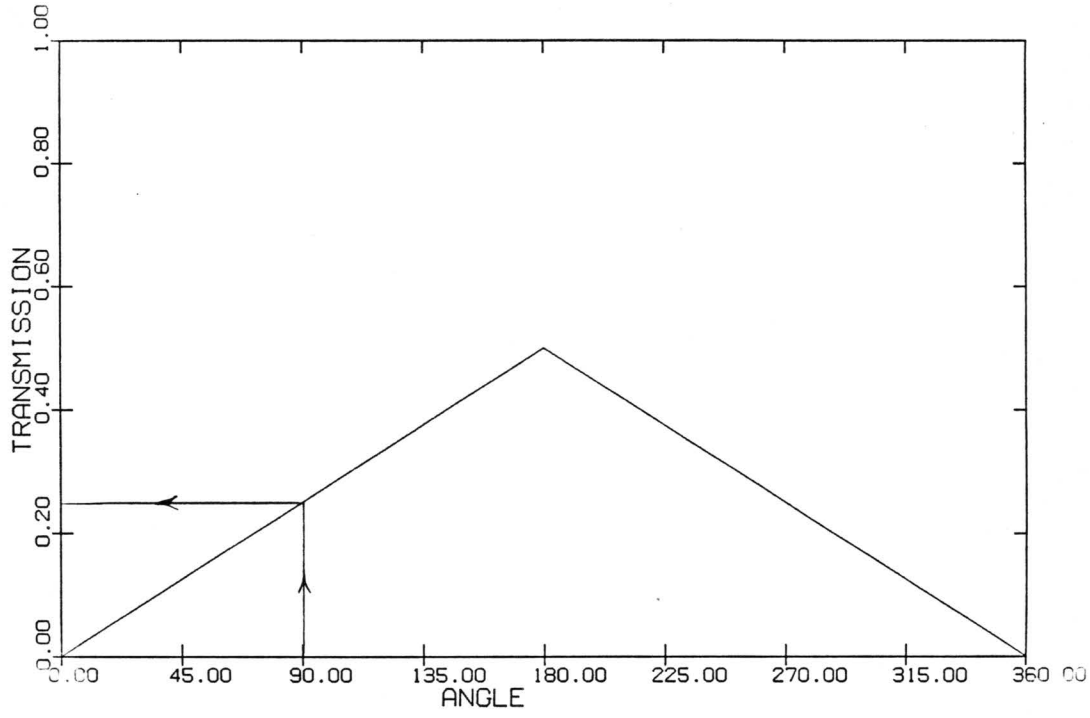

(a) Normalized Transmission vs. Angle (in Radians)

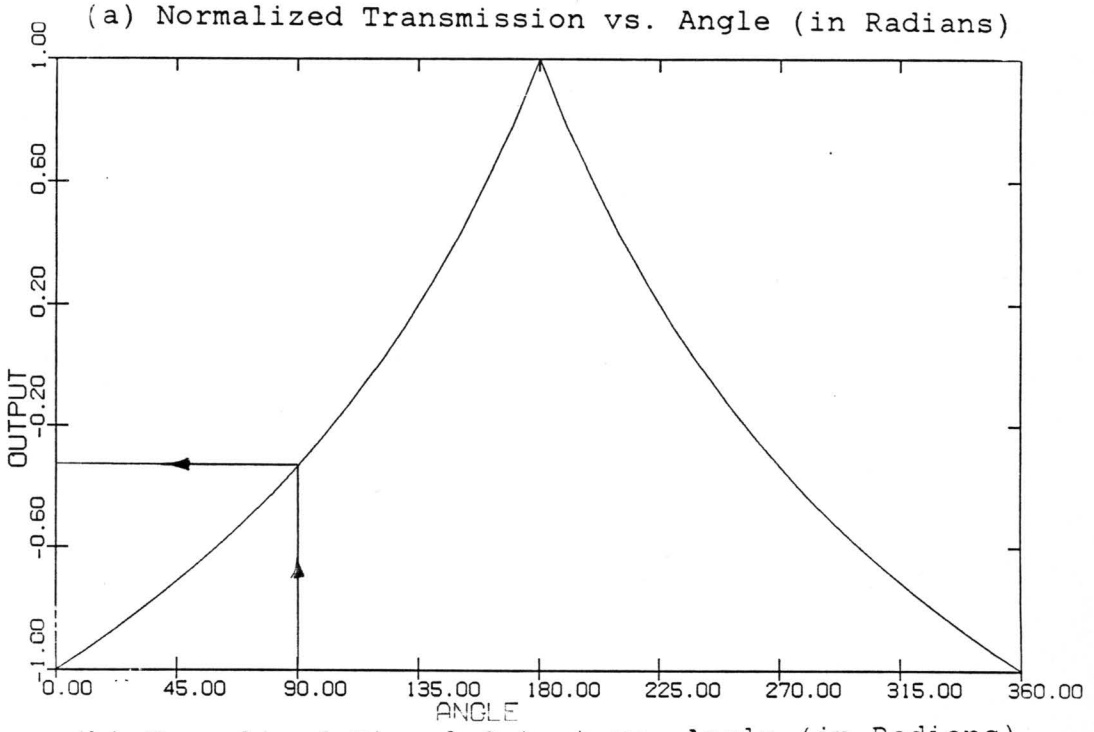

(b) Normalized Signal Output vs. Angle (in Radians)

Figure 4.22: Degraded Transmission and Corresponding Output

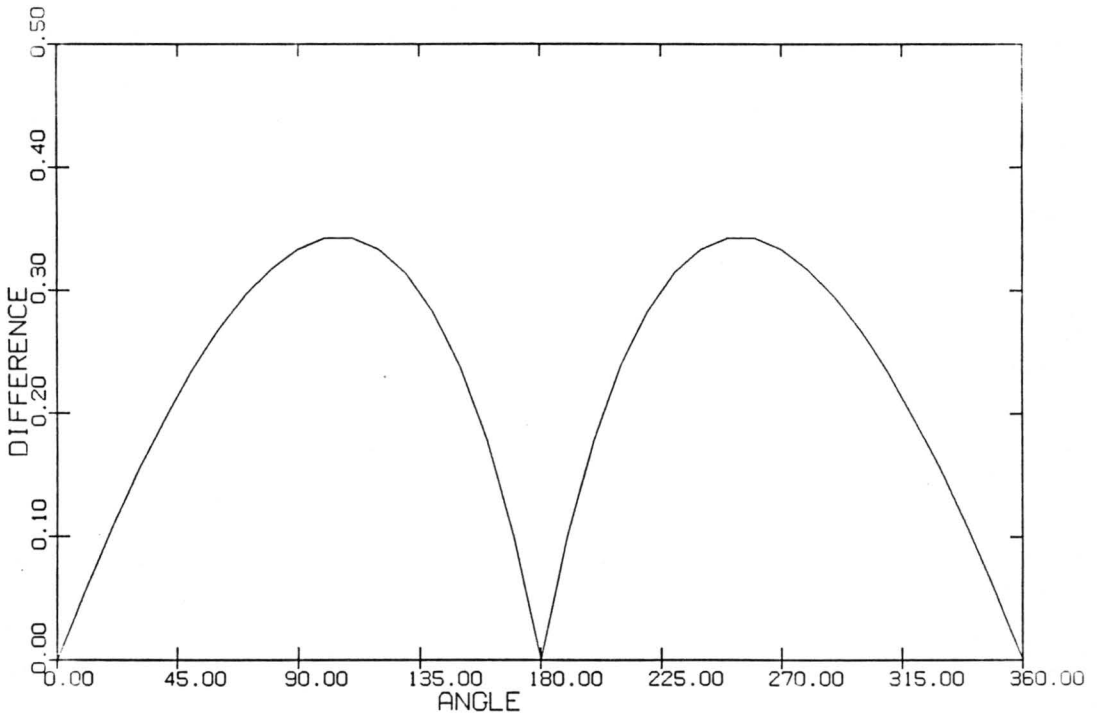

Figure 4.23: Error Trend for Degraded Channel Transmission

slope, as well as the output must be known in order to determine absolute position.

In conclusion, a dual beam, sum and difference technique can be applied to a fiber optic absolute position encoder. Such a set-up is completely unaffected by uniform signal degradation, and is more tolerant of random perturbations than its single transmission line counterpart. The price necessary for such noise insensitivity is added system complexity.

4.3 FIBER SENSORS AND WAVELENGTH DIVISION MULTIPLEXING

As fiber optic sensing technology becomes more complex, it is natural that multiplexing of signal channels would be desired. An obvious example occurring in a single sensor is provided in the previous section. In the analog approach to position encoding already presented, two channels of data are required. If a digital scheme were to be adopted by Gray coding the wheel, a number of channels would be required, depending on the necessary position resolution.

In addition to solitary sensor applications, a viable multiplexing format could be used to interrogate a number of discrete sensors in series along a single fiber. This is considered highly desirable, and the attractiveness increases in direct proportion to the distance between the sensor and its control unit. Although the use of wavelength division multiplexing (wdm) was proposed many years ago, it seems that multiplexing schemes have largely been performed in the time domain. A few examples of time domain multiplexing (tdm) systems, and a description of their wdm counterparts follow.

4.3.1 A Digital Position Encoder

A position encoder meeting the earlier description was developed at Sperry for use on military helicopters [1]. A simplified version of their system appears in Figure 4.24. In their system, a single line was first split into thirteen lines, each of which was brought up to the surface of a coded reflectance wheel. Although the authors show a star coupler as their power splitting device, the technology to produce it was not readily available at the time the system was developed. In fact, power splitting was accomplished by abutting thirteen 50 μm core fibers to a single 400 μm core fiber [78].

Time division multiplexing was performed by means of optical delay lines, as shown. This required the use of "delay bobbins," around which scores of meters of optical fiber were wound. Because each bit arriving to and from the code wheel experienced a different optical path length, a single pulse from the sending end generated a series of pulses (in time) in response.

Despite the theoretical advantages of their system over wdm or other schemes, documentation shows that the tdm approach was beleaguered with problems [78]. The delay bobbins were large and unwieldy, partially offsetting the small-size advantage of fiber optic sensors. Also, because

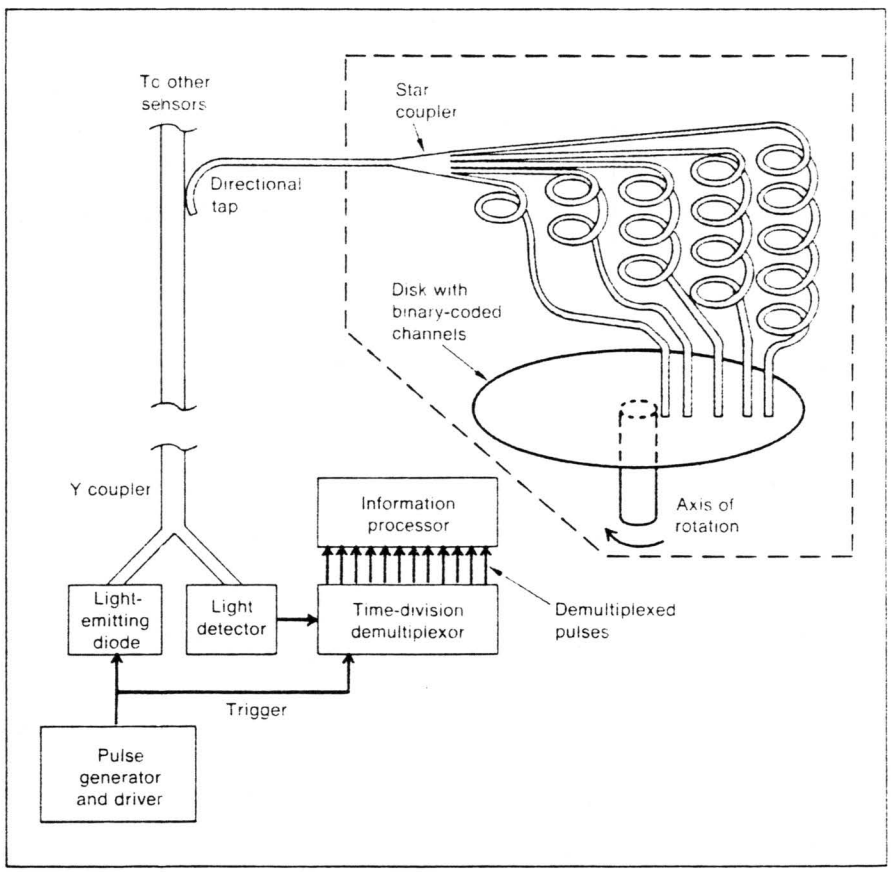

Figure 4.24: Time Division Multiplexed Position Encoder (after [1])

of varying fiber attenuation and power splitting ratios, signal intensities differed drastically from channel to channel. This presented serious difficulties at the receiving end, because a single detector was used to monitor all channels. Line to line uniformity was achieved by detuning all higher signals to the level of the lowest channel. It goes without saying that this is at best an inelegant approach.

The signal processing was not in itself a problem, but surely presented a complex task. The use of tdm required an extra timing-bit line, and the sampling rate was limited by the length of the delay lines and the speed of the electronics.

An alternate approach to the digital position encoder is being developed at Inland Motor. The system starts with a broadband source, as pictured in Figure 4.25. Similar to before, the light is split into twelve lines (directional couplers are now readily available), here of roughly equal lengths. Just prior to the wheel, each channel is filtered by a small, unique interference filter. Each wavelength is then modulated by the code pattern on the wheel and returned to the sending end. There, another star coupler splits the light again and a set of filters matching the first set decodes the output. A single photodiode detects the light from each channel.

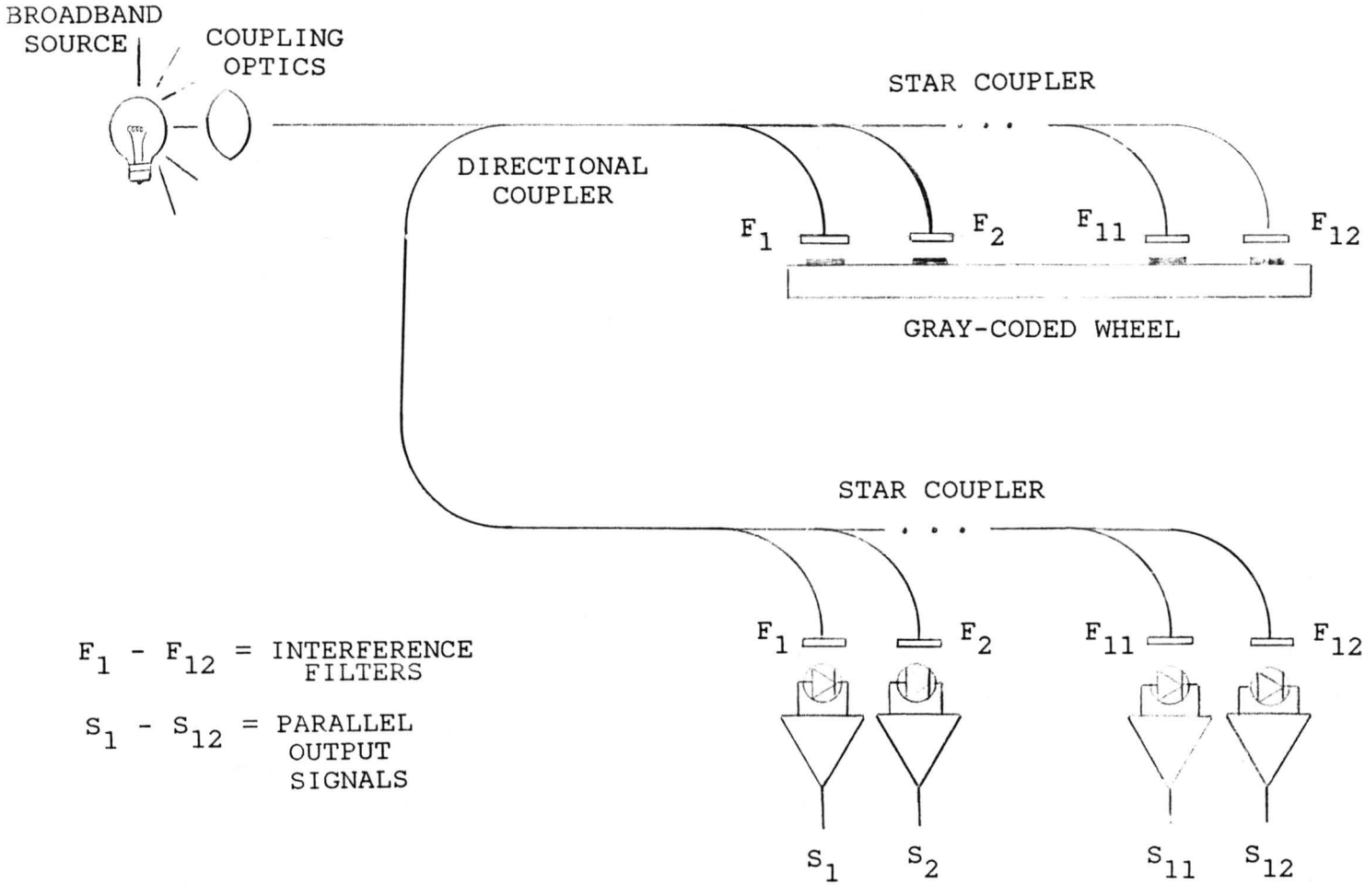

Figure 4.25: Wavelength Division Multiplexed Position Encoder

This system exhibits several advantages over the tdm approach. One is the lack of a need for troublesome delay lines. Another is that channel to channel signal variations are easily tolerated. Since each line is detected singly, differences can be compensated for by selective amplification rather than degradation. Also, the position sampling rate can be increased since detection is performed in parallel rather than in series. Finally, though several more photodiodes are required, these are now rather inexpensive, especially relative to the high-powered electronics required by the earlier design.

The system is not without disadvantages, however. The need for a second star coupler increases the system complexity and cost. This is true of the interference filters as well, though probably not prohibitively so; filter sets are easily obtained at low cost, and do not require special care or precision handling in assembly. Another disadvantage is that the signal intensity is split twelve ways twice, as opposed to only once in the tdm case. Whether this presents a problem depends on the input source power, the wavelengths relative to the fiber attenuation curve, and the Q of the optical filters. Work is presently underway to fully characterize the wdm system.

4.3.2 Sensor Arrays

Around the same time as the tdm encoder was reported, the authors at Sperry described a similar tdm system for multiplexing several sensors on a single line [8]. Reasonable system performance was noted for different sensors having roughly equal signal intensity changes. It is anticipated that the system would be intractable for sensors yielding significantly different signal strengths, in much the same way as their encoder was.

Another basically tdm approach has been described in detail in this report, namely OTDR. As noted earlier, several authors have suggested interrogating discrete sensors located along a single fiber using OTDR. Although calibration problems may require heavy computations such as deconvolution, this method does have promise.

Another method for passive multiplexing may be realized using wdm. A parallel approach can be taken, as in the case of the encoder, for an array of general transmissive sensors. Again a matched filter pair would be required for every sensor, as well as a detector. But, unlike with tdm, one signal may vary only slightly, while another may vary drastically; adjusting amplifier gains is all that is required to maintain a high SNR.

For the special case of microbending sensors, an interesting alternative arises. Equation (4.1) states and Figure 4.2 confirms that microbending attenuation is dependent upon the deformation period Λ_c of the fiber bender. However, the theory predicts that the attenuation also depends on the source wavelength λ. This functional dependence is often buried in β, the propagation wave number. Since λ is generally taken as a constant (single wavelength illumination assumed), its role in determining Λ_c is not reported.

Suppose now that a deformer D_1 is constructed having period Λ_1, yielding a maximum attenuation for light at λ_1. This is depicted in Figure 4.26. Another deformer of period Λ_2, D_2, causes maximum attenuation at λ_2. These two can be incorporated into a single fiber system such as seen in Figure 4.26. When broad band light is injected into the fiber, the deformers essentially act as band reject filters. That is, most wavelengths pass through the deformers unaltered, because Λ_1 and Λ_2 were chosen to effect only specific wavelengths λ_1 and λ_2.

At the outputs, single interference filters F_1 and F_2, corresponding to λ_1 and λ_2 follow a directional coupler. When a perturbation occurs at D_1, λ_1 is modulated independently of λ_2. Again the sensitivity of the detection can be tuned as needed. As many sensors as desired can be added to measure any effect which can be made to cause microbending.

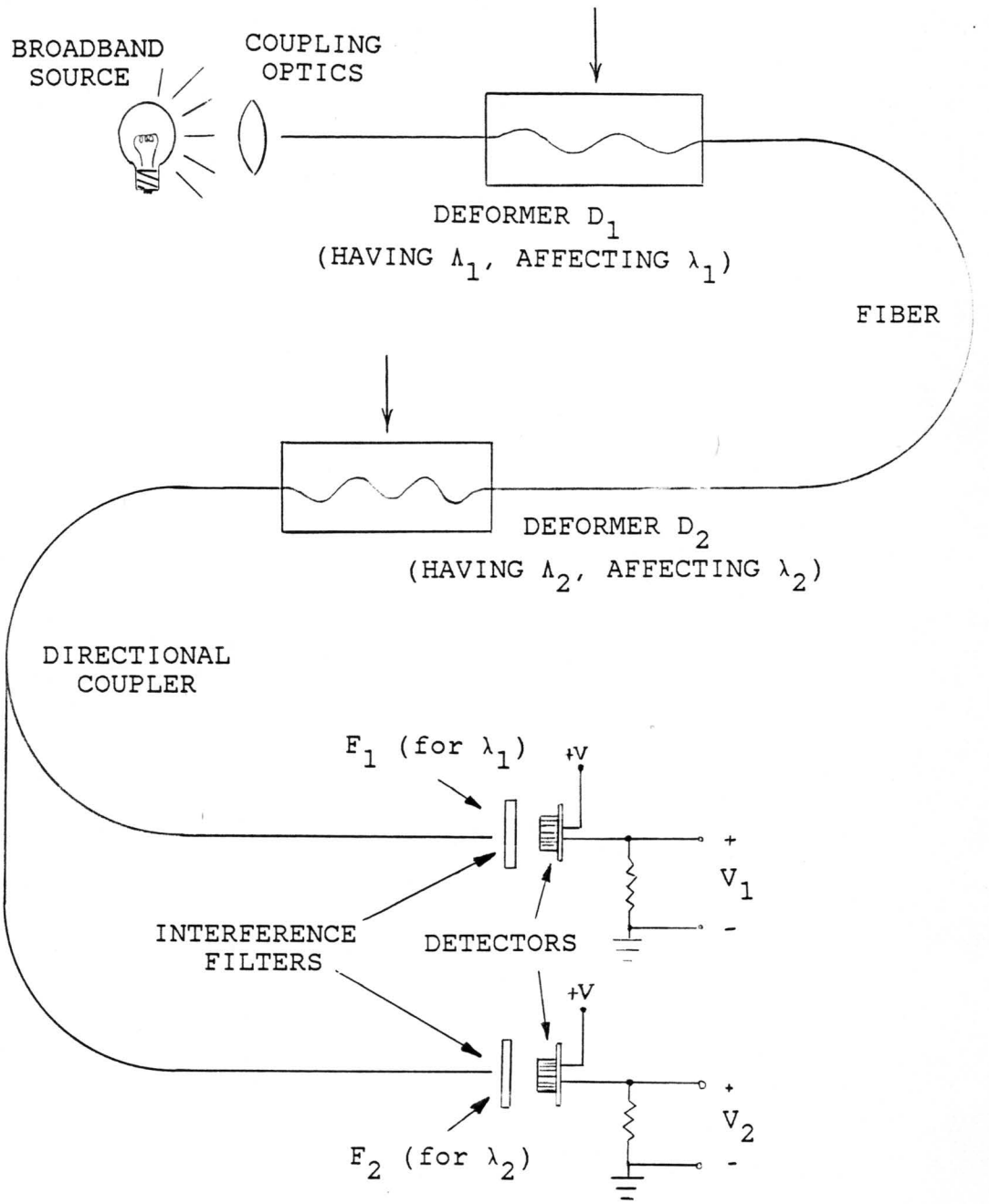

Figure 4.26: Microbend Sensing at Two Discrete Wavelengths

The obvious advantage to this format is that it requires only one interference filter and directional coupler. In addition, numerous configurations can be conceived which use interference filters in conjunction with tunable-period deformers. Increased flexibility of design characterizes this system. Moreover, stacking sensors in series on a single fiber becomes possible without the use of expensive and time intensive (noise averaging) OTDR.

The discrete sensor concept can also be extended to encompass distributed sensing applications. A simplified approach to this appears in Figure 4.27. As in the previous cases, broadband light enters the fiber, but here the fiber encounters only one continuous deformer, as shown. Position discrimination results from the fact that the deformation period changes along the length of the deformer. Thus, light of one wavelength is affected by the amount of microbending at one position, while another wavelength is affected by the microbending at another position.

Following the deformer, the light could be split into several channels using a star coupler, and filtered as in the previous examples. An alternate approach would be to disperse the light using a grating or a prism, as shown. An array of detectors could be used to sense the changes occurring at different wavelengths, which fall at different locations due to the dispersion.

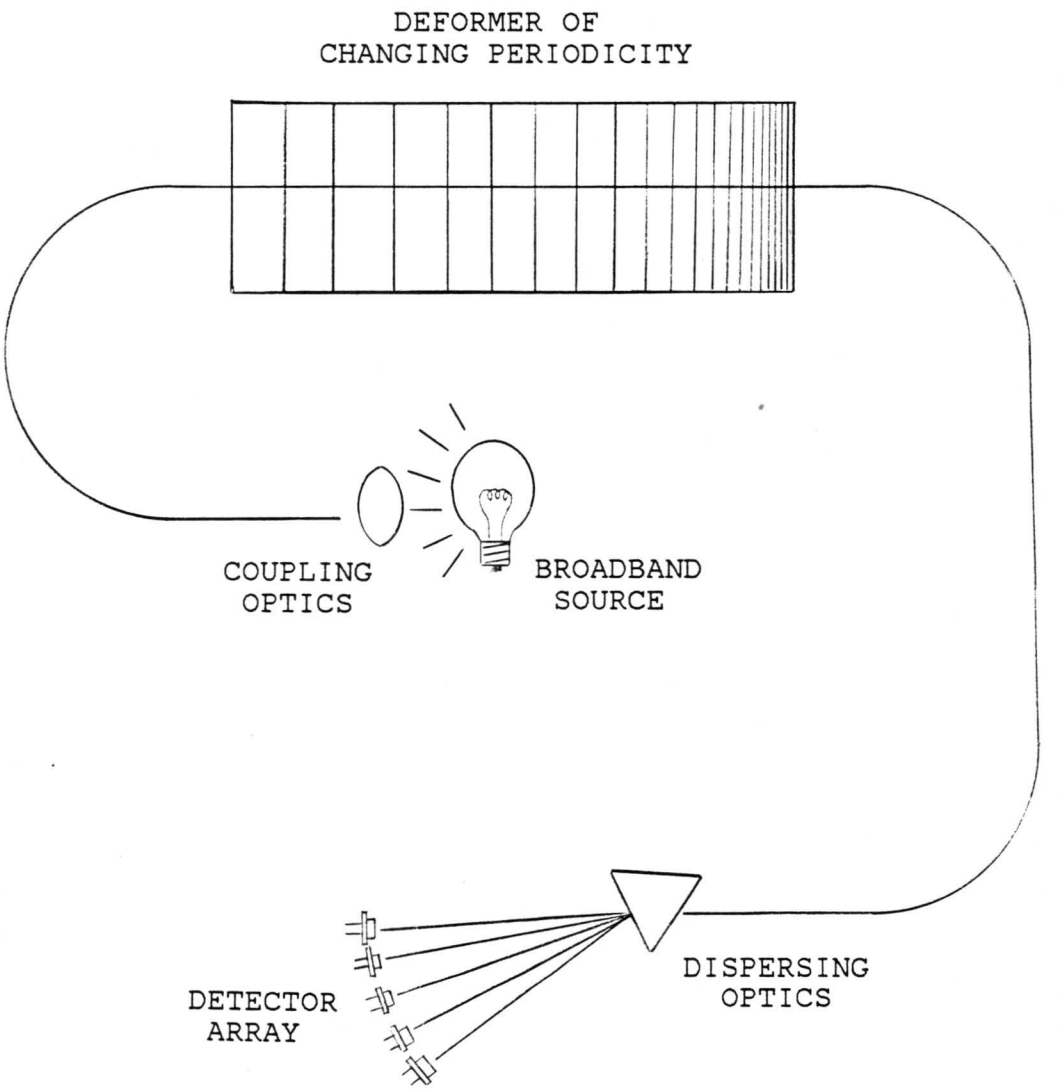

Figure 4.27: Distributed Sensing Using WDM

The resolution of the over-all system would depend in part on the deformation period range used, the type of grating used, and the geometry of the detector chip array. Preliminary results predict the resolution to be in the sub-millimeter range, representing a significant resolution over current OTDR methods. However, necessary theoretical and experimental work is presently underway to confirm the usefulness of this technique.

4.3.3 Conclusion

With the increased availability of low cost, high performance interference filters has come possibilities for wavelength sensing which were previously impractical. This can be used to advantage in both multiple-channel discrete sensors and in multiplexing an array of single sensors. Although many types of sensors are suitable for such wavelength division multiplexing, amplitude sensors seem to be most readily applicable. In particular, microbend sensors may show many advantages in wdm arrays, due to their intrinsic dependence on illumination wavelength.

4.4 A HIGH FREQUENCY CHOPPER/REFLECTOR

Modulation of gas laser light is typically desired for use in conjunction with a lock-in amplifier, and is often achieved by means of a light chopper. Generally, laser light interacts with some object or phenomenon to create a low amplitude optical signal. Because gas lasers are difficult to switch on and off at high frequencies, they are modulated with a light chopper. A noise-suppressed output results when both the chopping frequency and the detected signal are sent to the lock-in for processing.

4.4.1 Present and Ideal Designs

At present, choppers generally take one of two forms. One form, the resonant chopper, is basically a tuning fork which electromagnetically opens and closes an aperture at a fixed frequency. The other form is of rotating electro-mechanical design, consisting of an opaque wheel having a number of evenly spaced holes or slits tooled or etched in it. The wheel is directly coupled to a motor shaft; as the motor turns, light either passes through the openings in the wheel or is blocked. Both choppers yield square pulses of output light. A sketch of a rotating chopper wheel and motor assembly, made by Boston Electronics, appears in Figure 4.28a.

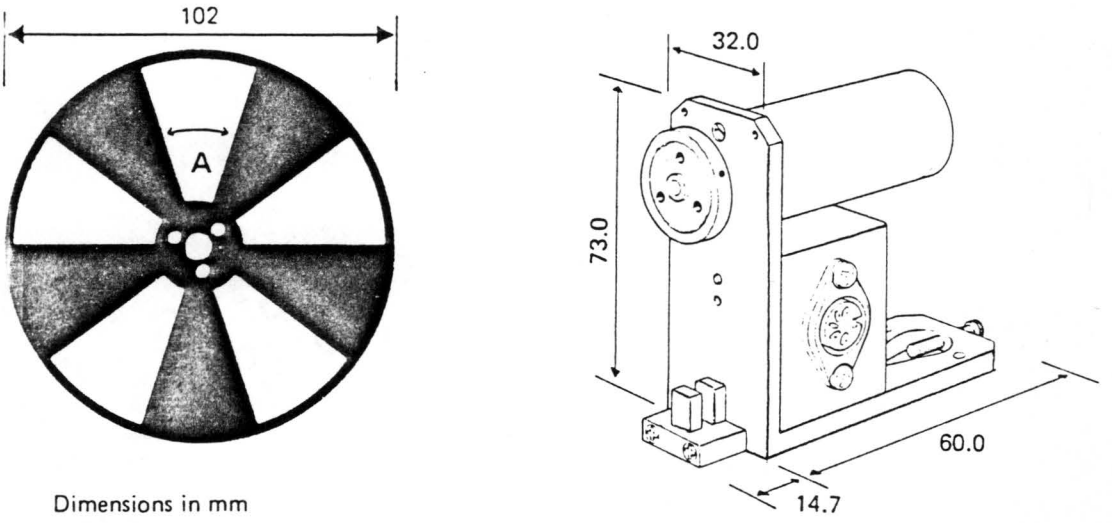

(a) Conventional Rotating Chopper (after [79])

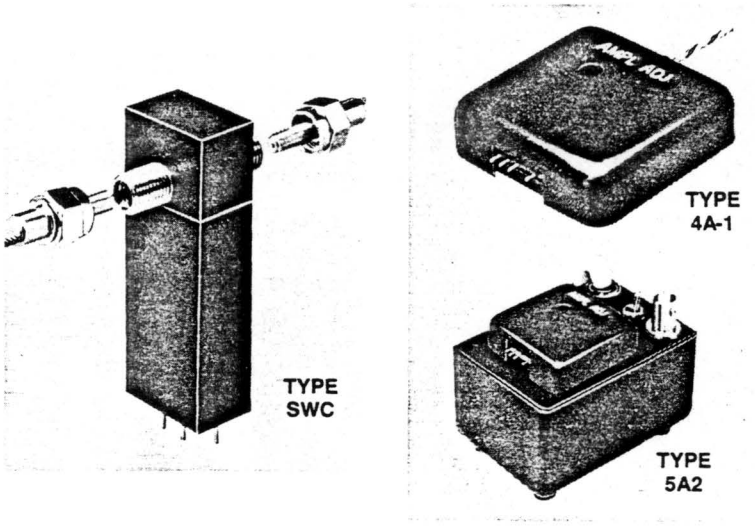

(b) Fiber Optic Resonant Chopper (after [80])

Figure 4.28: Representative Chopper Types

An "ideal" light chopper would include several features. Probably the most important of these would be a high operating frequency range, variable from tens of Hertz to hundreds of kiloHertz or higher. This would allow for traditional low frequency operations, as described above (usually ≈ 1 kHz). It would also allow for simulation of high frequency data transmission, especially suited for use with optical fibers.

Another highly desirable feature is small physical size. Besides the normal space/weight saving reasons, the small size is often necessary for certain focussed-beam experiments. The need for a chopper which permits close proximity of optics becomes even more apparent when dealing with such components as optical fibers and GRIN or other small lenses.

In addition to the features above, a chopper yielding variable waveshape outputs would be valuable. It could enhance the data signal simulation, as well as be a fruitful research tool for investigating the effects of different pulse shapes in different systems. Furthermore, a chopper which could also be used in a reflective mode would be useful in many types of experiments. In most cases the device could combine the operation of a chopper and a mirror in one package. Finally, a truly versatile chopper would include options to mount other optical components to it, thereby reducing optical set-up space and complexity.

The present light chopper market seems to suffer in all of the aforementioned areas. Typical frequency ranges are from a few hundred to a few thousand Hertz. At least one company offers a chopper which, for a sizeable cost, can be extended to reach 20 kHz [79]. This is still far short of the previously stated ideal.

The two ways of increasing the chopping frequency of a direct drive system are to either increase the motor speed, or increase the number of openings on the wheel. The desire for high motor speed is generally balanced by the size and weight criteria, and by the frequency stability considerations. Increasing the line (or hole) count also has certain bounds. If a wheel is not tooled with high precision and balance, it will become mechanically unstable at high rotation rates. Of course this will limit the upper frequency attainable. Aerodynamic instability also becomes more prominent at higher turn rates, further limiting frequency.

Another shortcoming in choppers available today is in the realm of physical size. Choppers rarely act as part of the signal-generating optical system; they merely function to modulate the signal of interest for use with a lock-in. As such, they are usually bulky, and therefore not particularly compatible with fiber optic sensor work. In this field, not only are the working dimensions usually small, but also the

chopper may actually play a role in generating the signal of interest.

Recently, a chopper compatible with optical fiber technology has been developed, as seen in Figure 4.28b [80]. It consists of of a small resonant chopper enclosed in a housing to which several small fibers are joined with SMA-type fiber connectors. Despite its compactness, this design has the clear disadvantages that it requires connectorized fibers for optical fiber work, is useable for more traditional chopping applications, and is operable at a single frequency only.

As far as the other ideal features are concerned, present technology seems to run totally dry. Apparently no attempts have been made to manufacture choppers yielding various types of intensity waveshapes. For a metal wheel having holes, balancing the wheel would probably require prohibitively expensive and frequency limiting optics mounted in the holes. Using choppers as reflectors is clearly possible with metal wheels by applying highly reflective paint. Of course the wheel geometry would play a role in the usefulness of this approach. These features, as well as including versatile mounting options, could surely be custom ordered, but no device today encompasses all or even many of the desired features.

4.4.2 Proposed Design

This section presents a chopper design intended to provide all the desirable features discussed above. The central component of the design is an opaque glass wheel with transparent areas etched away by a photolithographic process. The driving motor is housed in a small enclosure which also acts as mount for the wheel and the control elements. Several different options could be pursued, depending on the performance of prototype models. After discussing the initial design features, their merits and potential drawbacks will be raised, as well as suggestions for initial testing.

4.4.3 The Wheel

The advantages of an etched glass wheel are numerous. Because holes are not tooled or etched into the wheel, a quality glass wheel would be inherently balanced. Imbalances due to the layers of opaque film are considered negligible. This allows for stable high frequency rotations. Also, the absence of holes in the wheel allow it to be aerodynamically stable, again allowing for faster turning.

Another advantage of this wheel design follows from the fact that etching into a thin film is capable of producing a far higher line count than possible by machining or metal

etching the main structural member. This causes the available frequency range to soar and gives sharper on-off transitions as well. The higher line count also permits a smaller wheel to be used, thereby reducing the physical size of the housing and the driving motor, and therefore the cost.

As an example of the frequencies attainable, imagine a wheel with 1000 lines. This high line count requires a focussed beam of easily obtainable waist diameter. Directly coupling to the shaft of a motor turning at 6000 rpm (the standard maximum rate for presently used chopper motors), a frequency of 100kHz is possible.

These same high speeds are also attainable when large diameter beams are employed, if a Moire fringe approach is taken, as diagrammed in Figure 4.29. In this case, one wheel or piece of wheel is stationary, while a matched wheel rotates as before. This scheme requires the beam to be fairly well collimated. A special mount for holding a piece of a matched wheel very close to the rotating wheel is provided for in the design.

A further advantage of the etched glass wheel is that the opaque regions on the wheel are easily designed to be highly reflective. Thus the chopper can be used as a high speed reflector. This has particular application to retroreflec-

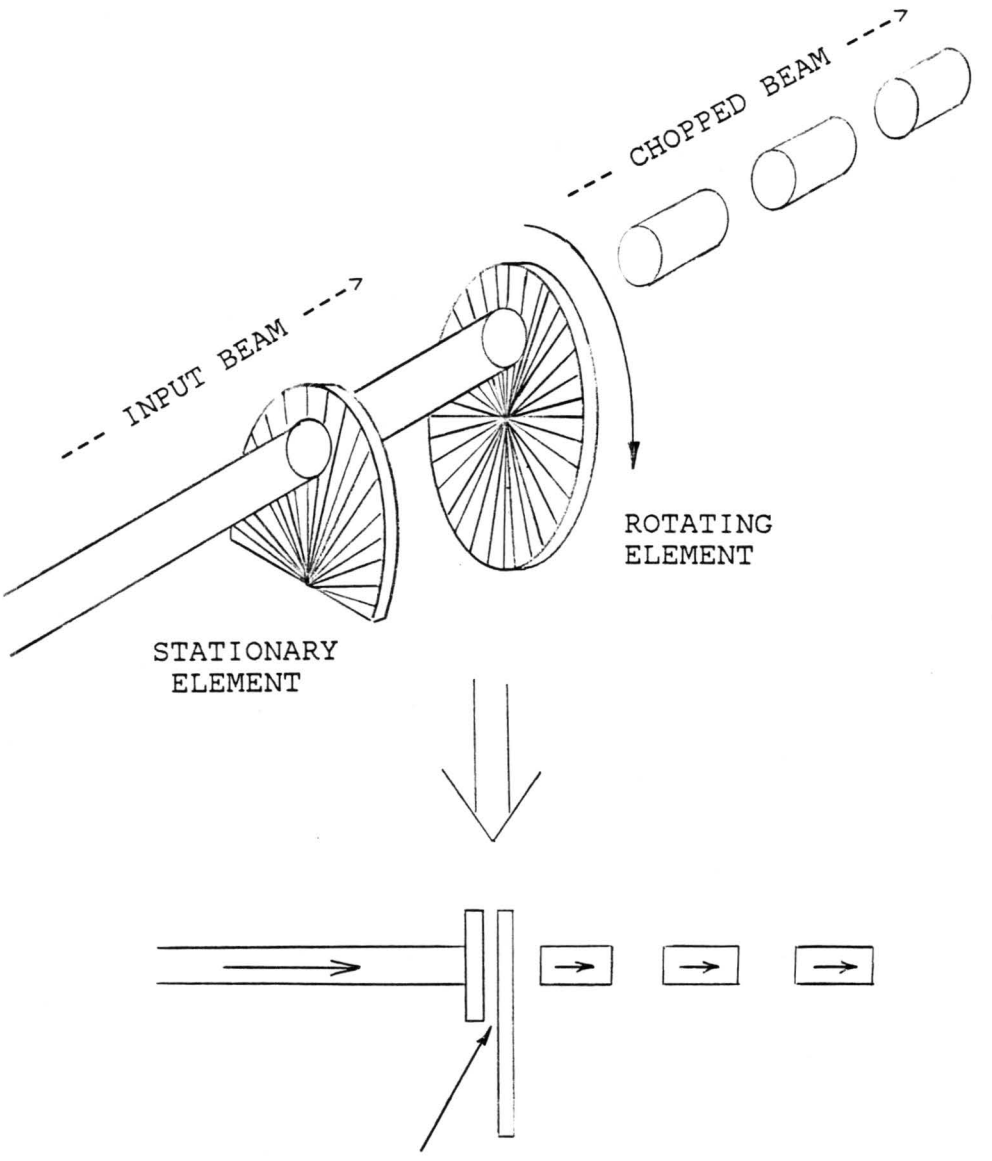

Figure 4.29: Moire Fringe Techniques

tive sensor design experiments. Also, this type of wheel easily allows for the possibility of various optical waveshapes by simply varying the photographic mask used to make the wheel. Several interchangeable wheels could accompany each chopper: a high frequency wheel (high line count), a low frequency wheel (low line count), and several waveshapes such as a sinusoid, triangle, sawtooth, low duty cycle pulse, or even a custom designed shape for special wave matching applications.

4.4.4 The Motor Coupling

In conventional choppers, the optical wheel is directly coupled to the drive shaft of the motor, necessarily requiring a relatively large lateral space for the assembly. In contrast, the present design calls for coupling the wheel and shaft by means of a beveled gear train. Figure 4.30 shows the wheel supported on a shaft between two bearings, and the motor mounted vertically. This allows for the use of a large, very high speed motor, without requiring a great deal of space, as well as introducing the possibility for speed increases due to advantageous gear ratioing.

An alternate design calls for a belt drive system. This would allow the motor to be displaced from the wheel, and thus again provides chopping in a small lateral space. This

is also illustrated in Figure 4.30. However, both methods require more study to determine the practical speed limits and motor power needs.

4.4.5 Additional Features

As with most chopper designs, an emitter-detector pair is used to monitor the operating frequency. Because of potentially high line counts, the emitter, an LED driven by a simple bias circuit, should be focussed at the wheel. This can be accomplished by shaping a plastic lens into the LED cap itself, or else with a GRIN lens. The pair is probably best mounted along a side wall of the enclosure.

In order to be able to replace the wheel, an upper panel is removable. If desired, a cap having two holes on opposite sides of the wheel could be fit over the top. As well as protecting the system from dust and damage, the cap could easily provide mounts for various types of optics. These might include lenses, neutral density or wavelength-selective filters, or beamsplitters.

In addition, a multi-terminal plug is provided for sending power to the motor and emitter-detector bias circuitry, as well as for receiving the detector output for feedback control. Of course a precision motor controller is required, as with a conventional chopper. A composite sketch of the preliminary design may be seen in Figure 4.32.

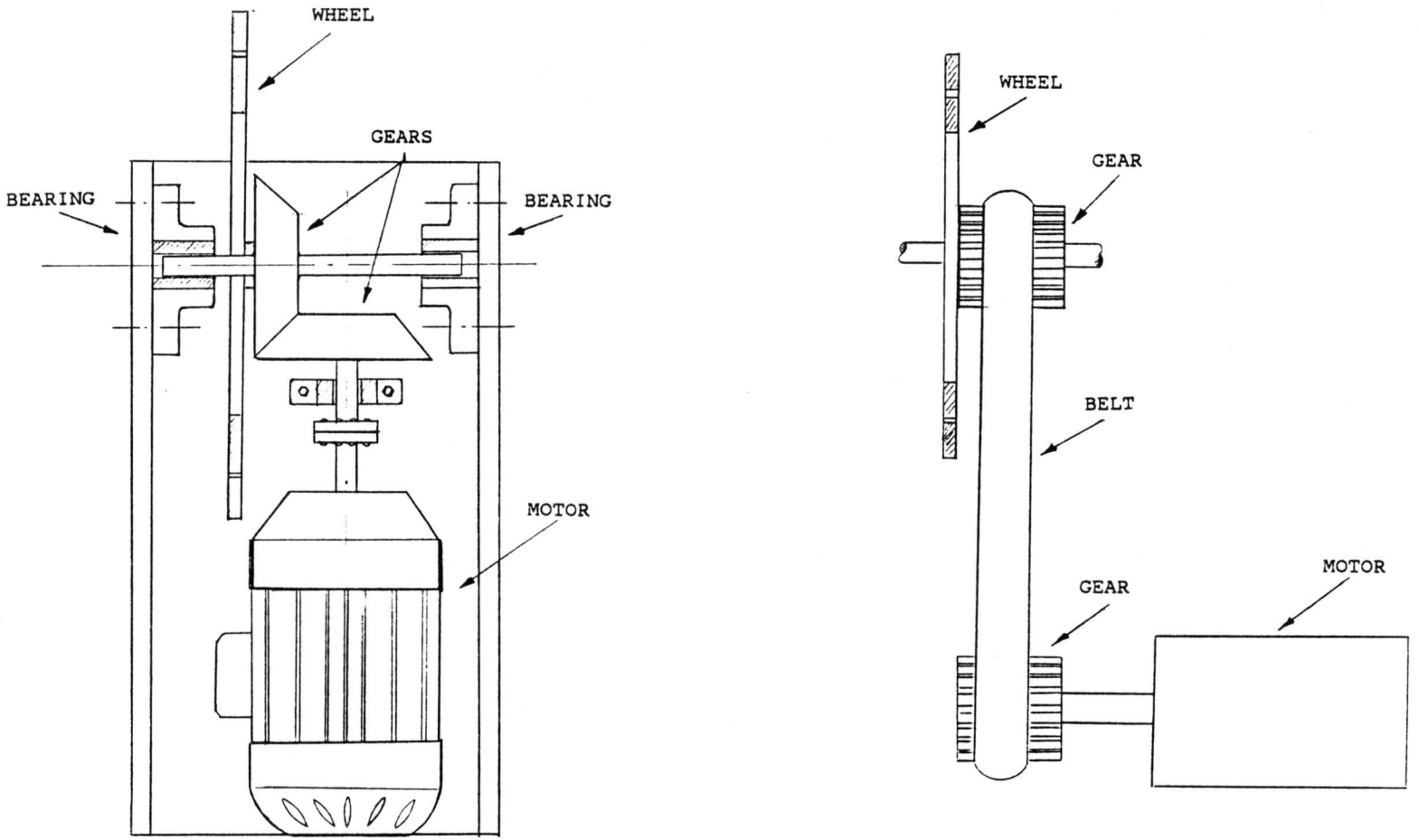

Figure 4.29: The Motor-Wheel Assembly

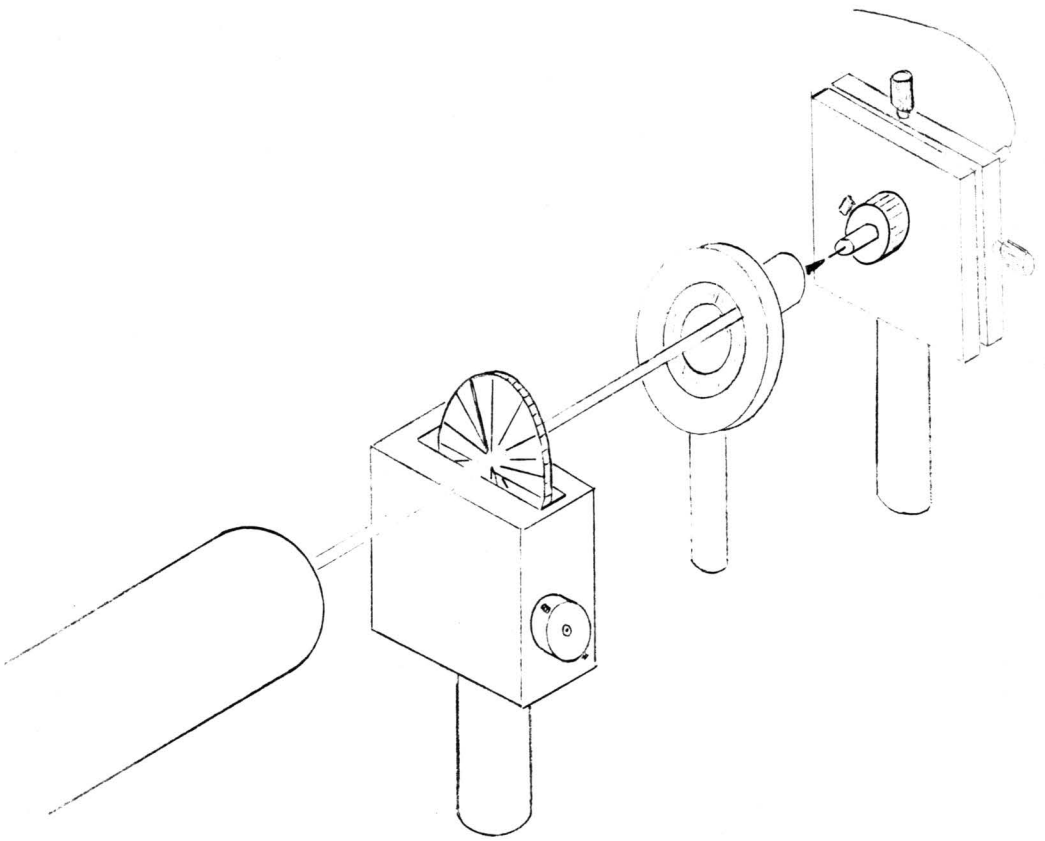

Figure 4.32: Composite Sketch

4.4.6 Discussion

The main advantage of the proposed system is its versatility. The operating frequency is variable by changing the motor speed, or even the gear ratio in the drive assembly. Further frequency control, as well as waveshape control is provided by using different wheels. By properly choosing the opaque material (probably Inconel), variable-speed reflectance measurements can be performed.

Also, because of the small size and possibility for mounting various bulk optics to the assembly, the chopper could be employed for many different applications, ranging from conventional use to fiber sensor design. Finally, it should be noted that many of the features can be changed to account for prohibitive cost or performance without compromising on all other areas. For example, most mechanical design changes would not affect the advantages gained through using a photo-etched glass wheel.

A highly flexible design is generally a complex one as well. This is perhaps the greatest disadvantage of the system, in that it would drive the manufacturing cost rather high. In particular, each wheel could be expected to cost upwards of $50, if obtained in small quantities. Another area of concern regards the ability of the mechanical gears to maintain high speeds reliably. If not, the wheel could

be mounted directly to the motor shaft without seriously jeopardizing the space savings if the motor is custom designed to provide as short a length as possible while retaining the necessary power.

In conclusion, the light chopper proposed herein possesses several novel features designed to fill gaps in the present sensor market. Though some questions remain as to the final cost and reliability of the system, it is expected that most problems can be overcome with minimal opto-mechanical testing. The drawing of final plans for the prototype model is presently underway.

4.5 CONCLUSIONS

It is recognized that the ideas presented in this chapter are but the tip of an immense iceberg, one which is in fact rapidly expanding. New fiber optic sensor applications range from using the fiber as a light guide only, to taking advantage of intrinsic opto-mechanical interactions. Effective realization of these novel techniques requires a clearer understanding of the propagation characteristics of light in both conventional and new fiber types, and for both the unperturbed and the perturbed cases.

Of particular interest are the effects of microbending an optical fiber. Despite the much erudition awarded this subject, a number of questions remain unanswered, especially with regard to correlating theory with practice. Also, with new fiber designs and application-oriented bending configurations, a great deal of the theoretical predictions need reformulation. In that light, the concentric core fiber mentioned in the first section both deserves and is receiving further attention.

Finally, work is required to render fiber sensors as practical alternatives to conventional sensors. Because of the unique advantage offered by EMP immunity, and because of the high cost of developing a new technology, fiber optic sensing is being driven primarily by the military market.

In order to retain the military interest, however, sensor packaging and related electronic subsystems need to be further developed, as well as the overall performance.

Appendix A

LISTING FOR OTDR SIMULATION PROGRAM

```
C$JOB
      REAL F(1500), P(1500), O(4000), A(1500), R(4000)
      REAL ANS, ATPKM1, ATPKM2, ATTEN1, ATTEN2, CCOUNT
      REAL FIBLEN, LENGTH, PULLEN, RFAC, TIME
      REAL*8 DSEED
      INTEGER AVG, COUNT, LF, LP, LO, PI, FI, OI
      INTEGER LPADD, KN, KEVOD, LPEVOD, SEGPM
C
C  FILEDEF 1 - TERMINAL, FOR DIRECT VIEWING ON THE SCREEN.
C  FILEDEF 3 - OUTPUT FILE <MODCON PLOTL> FOR DIRECT PLOTTING
C              OF MODCON RESULT WITH RESPECT TO LENGTH.
C  FILEDEF 4 - OUTPUT FILE <MODCON PLOTT> FOR DIRECT PLOTTING
C              OF MODCON RESULT WITH RESPECT TO TIME.
C  FILEDEF 6 - OUTPUT FILE <MODCON LISTING> FOR DIRECT ANALYSIS
C              MODCON RESULT.
C  FILEDEF 7 - OUTPUT FILE <MODCON READY>, WITH NECESSARY
C              PARAMETERS AND OUTPUT FOR SLOPE PROGRAM.
C
C  SET UP FIBER PARAMETERS:
      FIBLEN = 90.0
      PULLEN =  2.0
      SEGPM = 10
      RFAC = 0.00000
      DSEED = 1234567.
      LF = FIBLEN*SEGPM + 0.5
      LP = PULLEN*SEGPM + 0.5
      LO = 2*LF + LP
C
C  GENERATE FIBER ARRAYS
      CALL GENFIB (F,A,LF,SEGPM)
C
C  GENERATE PULSE PROFILE:
      CALL GPULSE(P,LP)
C
C  PERFORM MODIFIED CONVOLUTION:
      CALL CONVLV(F,P,A,O,LF,LP,LO)
C
C   USER DECIDES WHETHER OR NOT TO GENERATE A
C   NOISE ARRAY AND THE FACTOR:
      WRITE (1,50)
50    FORMAT ('TO GENERATE NOISE ARRAY, TYPE 1, ELSE TYPE 0')
      READ (1,*) ANS
      IF (ANS.NE.1.) GOTO 140
      WRITE (1,60)
60    FORMAT ('ENTER THE NOISE FACTOR')
      READ (1,*) RFAC
      WRITE (1,65)
65    FORMAT ('ENTER THE NUMBER OF CURVES TO AVG')
      READ (1,*) AVG
C
C   GENERATE NOISE ARRAY, ADD NOISE TO OUTPUT,
C   AVG TERMS TOGETHER:
      DO 130 J = 1,AVG
         CALL GGUBS (DSEED, LO, R)
         DO 120 NTEMP = 1, LO

            O(NTEMP) = O(NTEMP) + (R(NTEMP)*RFAC)/AVG
120      CONTINUE
130   CONTINUE
C
C  SEND THE NUMBER OF POINTS GENERATED TO SLOPE PROGRAM
C  SO IT WILL KNOW HOW MANY POINTS TO READ:
140   WRITE (7,145) LO
145   FORMAT (I5)
```

```
C
C  SEND SEGPM AND PULLEN TO SLOPE PROGRAM SO IT WILL
C  KNOW HOW MANY POINTS TO SUBTRACT OFF OF EITHER END
C  DUE TO INITIAL AND FAR END REFLECTIONS:
      WRITE (7,146) SEGPM, PULLEN
146   FORMAT (I5,6X,F4.1)
C
      DO 160 COUNT = 1,LO
C  THE UNITS FOR COUNT IS "SEGMENTS", SO CCOUNT HAS UNITS
C  OF "METERS"; CCOUNT IS THE LENGTH TRAVELED BY PULSE IN
C  METERS FOR A GIVEN OUTPUT:
         CCOUNT = FLOAT(COUNT)/SEGPM
         TIME = CCOUNT/2.0E8
         LENGTH = CCOUNT/2.0
         WRITE (3,156) LENGTH, O(COUNT)
         WRITE (4,155) TIME, O(COUNT)
         WRITE (7,156) LENGTH, O(COUNT)
155      FORMAT (F15.12,6X,F12.9)
156      FORMAT (F8.2,6X,F12.9)
160   CONTINUE
C
      WRITE (6,165)
165   FORMAT (///)
C
      STOP
      END
C
C
C
CF
      SUBROUTINE GENFIB(F,A,LF,SEGPM)
C
      REAL A(LF), F(LF)
      REAL ATPKM1, ATPKM2, ATTEN1, ATTEN2, SCATDB, SCATT
      INTEGER SEGPM
C
C  COMPUTE ATTENUATION AND SCATTERING COEFFICIENTS PER SEGMENT:
      ATPKM1 = 4.0
      ATTEN1 = 1.0 - 10.0**(-ATPKM1/(10000.0*SEGPM))
C  THE NEXT TWO WILL CREATE VERY HIGH ATTENUATION (300 DB/KM):
C      ATPKM2 = 300.0
C      ATTEN2 = 1.0 - 10.0**(-ATPKM2/(10000.0*SEGPM))
      SCATDB = 4.0
      SCATT = 10.0**(SCATDB/(10000.0*SEGPM)) - 1.0
C
C  ASSIGN REFLECTION AND SCATTERING COEFICIENTS:
C
      DO 1000 NTEMP = 1,LF
         F(NTEMP) = SCATT
1000  CONTINUE
C  ADDITIONAL COEFFICIENT FOR END REFLECTION:
      F(LF) = .0005
C
C  ASSIGN ATTENUATION COEFFICENTS:
C
      DO 3000 NTEMP = 1,LF
         A(NTEMP) = ATTEN1
3000  CONTINUE
C  ADDITIONAL ASSIGNMENTS FOR ABSORPING REGIONS:
C      DO 4000 NTEMP = 400,500
C         TEMP = FLOAT(NTEMP)
C         ATPKM2 = 104.0 - 0.04*(TEMP - 450.0)**2
C         ATTEN2 = 1.0 - 10.0**(-ATPKM2/(10000.0*SEGPM))
C         A(NTEMP) = ATTEN2
C4000  CONTINUE
C
      RETURN
      END
```

```
C
CCC
      SUBROUTINE GPULSE(P,LP)
C
      REAL P(LP)
C
C  ZERO PULSE PROFILE ARRAY:
C
      DO 1000 NTEMP = 1,LP
         P(NTEMP) = 0.
1000  CONTINUE
C
C  SET UP DESIRED PULSE PROFILE (VARIABLE), HERE, A RECTANGLE:
C
      DO 2000 NTEMP = 1,LP
         P(NTEMP) = 1.
2000  CONTINUE
C
C  IF PULSE SHAPE IS DEFINED WITH P(1) AS BEING THE
C  LEFT-MOST POINT, FIRST INDICIES MUST BE REVERSED
C  SO P(1) IS FIRST TO ENTER FIBER:
      DO 3000 NTEMP = 1,LP
         P(NTEMP) = P(LP + 1 - NTEMP)
3000  CONTINUE
C
      RETURN
      END
C
CCCC
      SUBROUTINE CONVLV (F, P, A, O, LF, LP, LO)
C
C  INPUT VARIABLES:
C     A       =  FIBER ATTENUATION PROFILE
C     F       =  FIBER REFLECTION PROFILE

C     LF      =  LENGTH OF FIBER IN TERMS OF SEGMENTS
C     LO      =  LENGTH OF OUTPUT IN TERMS OF SEGMENTS
C     LP      =  LENGHT OF PULSE IN TERMS OF SEGMENTS
C     P       =  PULSE PROFILE
C
C  OUTPUT VARIABLE:
C     O       =  OUTPUT ARRAY OF MODIFIED CONVOLUTION
C
C  VARIABLES USED WITHIN THIS SUBROUTINE:
C     FI      =  FIBER INDEX
C     K       =  STEP NUMBER
C     KN      =  NUMBER OF ITERATIONS REQUIRED FOR CONVOLUTION
C     ML      =  MULTIPLICATION LOOP LOWER LIMIT
C     MU      =  MULTIPLICATION LOOP UPPER LIMIT
C     NTEMP   =  TEMPORARY INTEGER VARIABLE
C     OI      =  OUTPUT INDEX
C     PI      =  PULSE INDEX
C     TEMP    =  TEMPORARY REAL VARABLE
C

      REAL F(LF), P(LP), O(LO), A(LF)
      INTEGER PI, FI, OI, KN, LPADD, COUNT, KEVOD, LPEVOD
C
C      WRITE (6,5010) LO
C5010  FORMAT (//,' THERE WILL BE LO-2 ITERATIONS; LO = ',I4,/)
C
      KN = LO - 1
      LPADD = LP + 1
      DIFF = LO - LP
      LOLESS = LO - 1
C
C   ZERO THE OUTPUT ARRAY:
C
      DO 5000 COUNT = 1,LO
          O(COUNT) = 0.0
5000  CONTINUE
C
```

```
C
      DO 1000 K = 2,KN
         ML = 1
         MU = LF
         PI = K - 1
         OI = K
C  LPEVOD IS 0 OR 1, DEPENDING ON WHETHER LP IS
C  EVEN OR ODD, RESPECTIVELY:
         LPEVOD = MOD(LP,2)
         IF (LPEVOD.EQ.1) GOTO 5100
C  KEVOD IS 0 OR 1, DEPENDING ON WHETHER K IS
C  EVEN OR ODD, RESPECTIVELY:
            KEVOD = MOD(K,2)
            IF (KEVOD.EQ.1) GOTO 4200
C  IF YOU ARE HERE, LP IS EVEN AND K IS EVEN:
               IF (K.GT.LPADD) ML = (K - LP + 2)/2
               IF (K.GT.LPADD) PI = LP - 1
               IF (K.LT.DIFF) MU = K/2
            GOTO 5300

C  IF YOU ARE HERE, LP IS EVEN AND K IS ODD:
4200           IF (K.GT.LPADD) ML = (K - LP + 1)/2
               IF (K.GT.LPADD) PI = LP
               IF (K.LT.DIFF) MU = (K - 1)/2
            GOTO 5300
C
5100        KEVOD = MOD(K,2)
            IF (KEVOD.EQ.1) GOTO 5200
C  IF YOU ARE HERE, LP IS ODD AND K IS EVEN:
               IF (K.GT.LPADD) ML = (K - LP + 1)/2
               IF (K.LT.DIFF) MU = K/2
               IF (K.GT.LPADD) PI = LP
            GOTO 5300
C  IF YOU ARE HERE, LP IS ODD AND K IS ODD:
5200           IF (K.GT.LPADD) ML = (K - LP + 2)/2
               IF (K.LT.DIFF) MU = (K - 1)/2
               IF (K.GT.LPADD) PI = LP - 1
5300  CONTINUE
C
C  THE MAIN MULTIPLICATION LOOP:
C
         DO 5400 COUNT = ML,MU
            FI = COUNT
C  MULTIPLY PULSE VALUE AND FIBER VALUE AT EACH POSITION:
            TEMP = F(FI)*P(PI)
C
C  ADD REFLECTED ENERGY TO BACKSCATTERED WAVE (OUTPUT):
            O(OI) = O(OI) + TEMP
C  SUBTRACT REFLECTED ENERGY FROM FORWARD TRAVELING PULSE:
            P(PI) = P(PI) - TEMP - A(FI)
            PI = PI - 2
5400     CONTINUE
1000  CONTINUE
C
C  CORRECT FOR ALIASING.  O(1) AND O(LO) ARE BOTH
C  LEFT WITH ZERO VALUE:
      DO 6000 NTEMP = 2,LOLESS
         O(NTEMP) = (O(NTEMP) + O(NTEMP+1))/2
6000  CONTINUE
C
      RETURN
      END
C$ENTRY
```

Appendix B

LISTING FOR SLOPE PROGRAM

```
C$JOB
      REAL O(2000), SLPX(1999), SLPY(1999), SKIP
      INTEGER I, J, K, LO, SEGPM, SKIPLO, SKIPHI, SLEN
C
C  FILEDEF 2 - INPUT FILE <MODCON READY> CONTAINING
C              ALL INPUT DATA.
C  FILEDEF 3 - OUTPUT FILE <SLOPE ENDS> CONTAINING
C              SLOPE OVER THE
C              ENTIRE LENGTH, INCLUDING THE ENDS.
C  FILEDEF 4 - OUTPUT FILE, <DERIV1 PLOT> AVAILABLE
C              FOR PLOTING THE FIRST DERIVATIVE OF
C              THE INPUT DATA.
C  FILEDEF 7 - OUTPUT FILE <GO1 READY> AVAILABLE FOR
C              READING BACK INTO <SLOPE WATFIV> FOR
C              COMPUTING THE SECOND DERIVATIVE.
C
      READ (2,100) LO
100   FORMAT (I5)
C
C  THE X VALUES OF THE SLOPE ARE HALF WAY BETWEEN
C  THE X COORDINATES OF THE O(I) VECTOR, NAMELY .5,
C  1.5, 2.5, ETC.  THIS MEANS THE LENGTH OF THE SLOPE
C  VECTOR IS ONE SHORTER THAN THE O VECTOR:
      SLEN = LO - 1
C
      READ (2,150) SEGPM, PULLEN
150   FORMAT (I5,6X,F4.1)
C
C  INITIALIZE SKIPLO AND SKIPHI.  THE INT( ) COMMAND
C  TRUNCATES SKIP IF IT'S A FRACTION (THE "SAFE" CASE):
      SKIP = SEGPM*PULLEN
      SKIPLO = INT(SKIP)
      SKIPHI = SLEN - INT(SKIP) - 2
C
C  READ IN THE DATA FROM ANOTHER FILE:
      DO 300 I = 1,LO
         READ (2,200) SLPX(I), O(I)
200      FORMAT (F8.2,6X,F12.9)
300   CONTINUE
C
C  WRITE SLEN, SEGPM, AND PULLEN TO AN FILE FOR
C  RERUNNING THE SLOPE PROGRAM:
      WRITE (7,600) SLEN
600   FORMAT (I5)
      WRITE (7,150) SEGPM, PULLEN
C
C  CALCULATE THE SLOPE AS THE DIFFERENCE BETWEEN
C  ADJACENT POINTS, STARTING BETWEEN THE FIRST AND
C  SECOND (FIRST POINT IS ALWAYS 0.00),
C  ALSO MAGNIFY BY A FACTOR OF 100,000:
C
      DO 500 K = 1,SLEN
         SLPY(K) = 100000.*(O(K+1) - O(K))
C         WRITE (3,700) SLPX(K), SLPY(K)
C         IF (ABS(SLPY(K)).GT.0.10) SLPY(K) = 0.0
          IF (K.LE.SKIPLO) SLPY(K) = 0.0
          IF (K.GE.SKIPHI) SLPY(K) = 0.0
          WRITE (4,700) SLPX(K), SLPY(K)
          WRITE (7,700) SLPX(K), SLPY(K)
700       FORMAT (F8.2,6X,F12.9)
500   CONTINUE
C
      STOP
      END
C$ENTRY
```

Appendix C

MICROBENDING TEST ASSEMBLY COMPONENTS

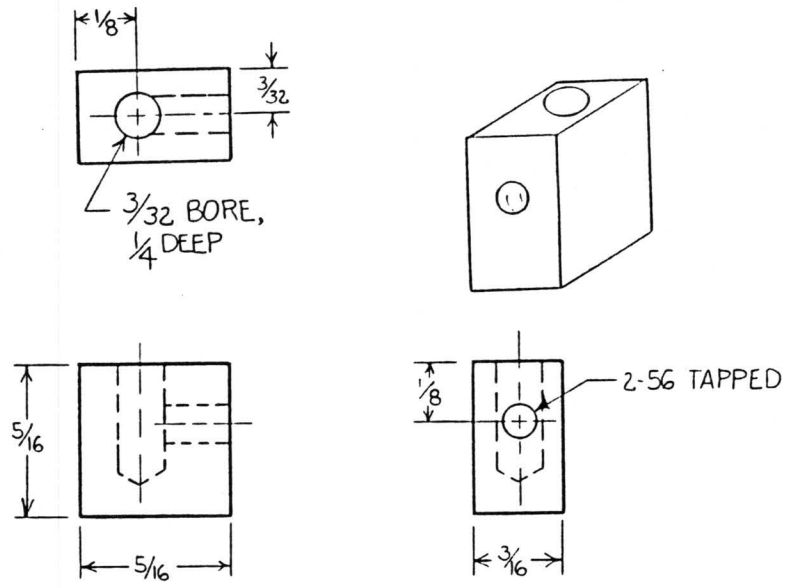

PIN MOUNT

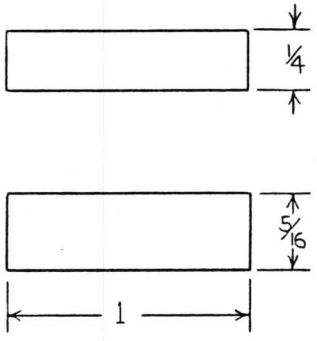

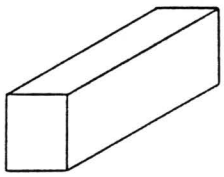

YOKE SHIM - FOUR NEEDED

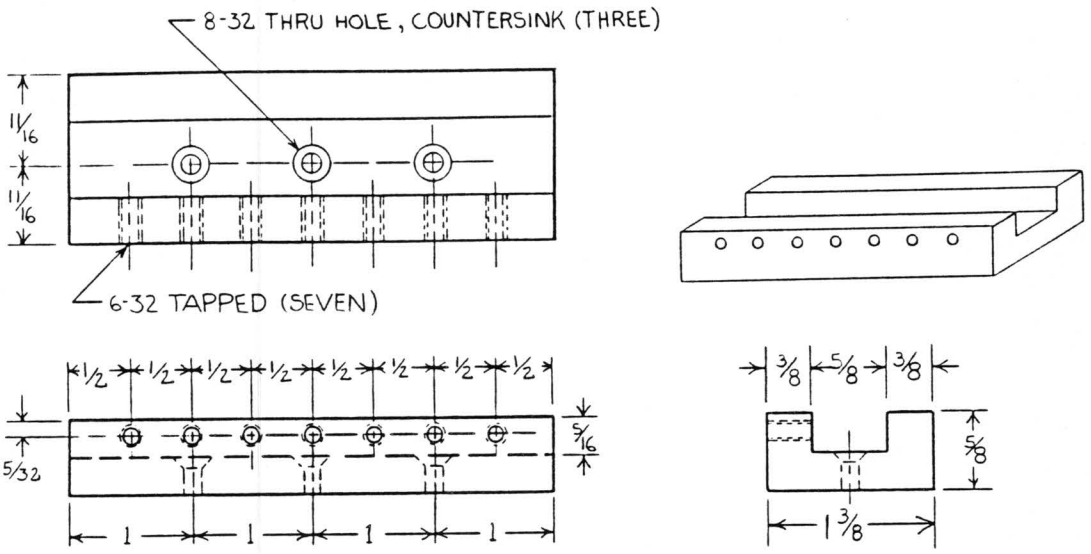

MAIN YOKE - ONE NEEDED

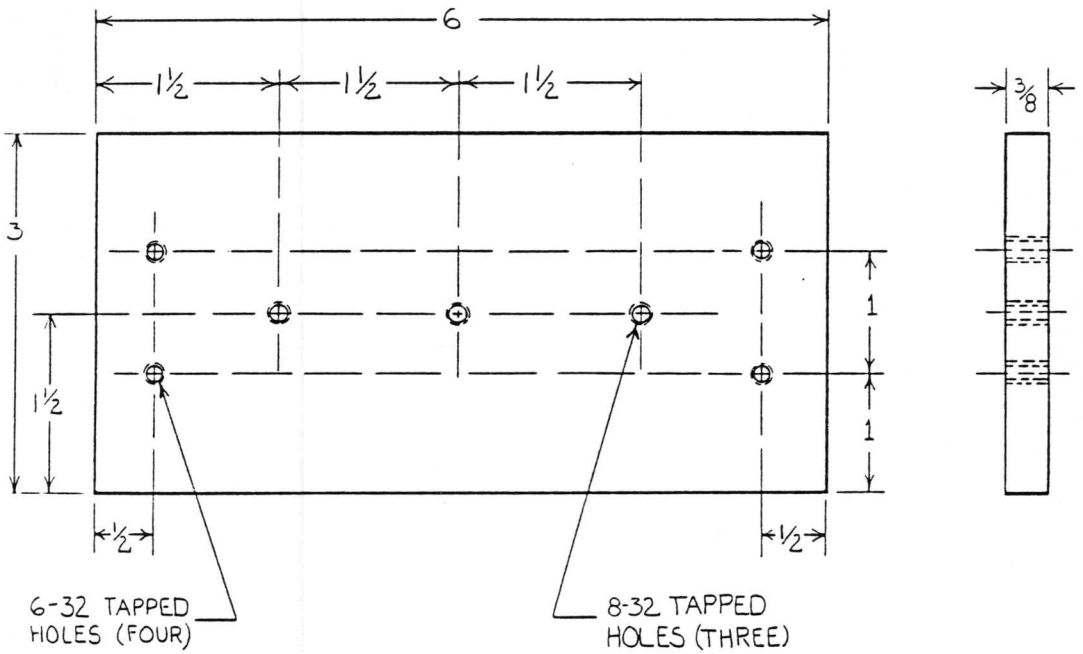

BASE PLATE - ONE NEEDED

Appendix D

LISTING FOR ENCODER SIMULATION PROGRAM

```
C$JOB
C
C   THIS PROGRAM CALCULATES THE DIFFERENCE/SUM QUOTIENT FOR
C   A DUAL BEAM FIBER OPTIC ENCODER, DESCRIBED IN THE TEXT.
C   THE SHAPE OF THE WHEEL TRANSMISSION AS A FUNCTION OF
C   ANGLE CAN VARY ACCORDING TO DESIRE.  THE CODE LISTED
C   WAS USED TO GENERATE THE TWO-PIECE LINEAR TRANSMISSION
C   CURVE SEEN IN FIGURE 4.21, AS WELL AS THE CORRESPONDING
C   CURVES OF FIGURES 4.22, AND 4.23.
C
      REAL ANGLE, PI, TWOPI, THETAA, THETAB, DELTHA
      REAL TA1, TB1, ERROR
      DIMENSION ANGSIG(360,2), ESIG(360)
      INTEGER ANG, ANS
C
C   AS THE WHEEL TURNS, ANGLE CHANGES.  THETAA IS THE
C   ANGLE OF THE "A" BEAM, IN RADIANS.  THETAB IS DISPLACED
C   FROM THETAA BY DELTHA. USUALLY, AS HERE, DELTHA 180
C   DEGREES (PI).  THE SINGLE-LINE TRANSMISSION (BEAM A)
C   IS REPRESENTED BY TA1, WHILE TB1 IS THE TRANSMISSION
C   OF BEAM B.  ERROR HOLDS THE DIFFERENCE BETWEEN THE
C   "PRESUMED" ANSWER AND THE RECEIVED RESULT IN THE EVENT
C   OF A DEGRADED CHANNEL.  THE DIFFERENCE/SUM OUTPUT IS
C   STORED, ALONG WITH EACH COORESPONDING ANGLE, IN THE TWO
C   DIMENSIONAL ARRAY ANGSIG.  THE SAME QUANTITIES FOR THE
C   CASE OF A DEGRADED CHANNEL ARE HELD IN A SIMILAR ARRAY
C   TERMED ESIG.  THE USER DECIDES ABOUT THE DEGRADATION TO
C   RUN; ALL ANSWERS FROM THE USER ARE STORED IN ANS.
C   FIRST, INITIALIZE THE CONSTANTS:
      PI = 3.1415926535
      TWOPI = 2.0*PI
      DELTHA = PI
C
C   THE MAIN LOOP.
      DO 600 ANG =  10,360,10
         ANGLE = FLOAT(ANG)
         THETAA = ANG*PI/180.0
         THETAB = DELTHA + THETAA
         IF (THETAB.GT.TWOPI) THETAB = THETAB - TWOPI
         IF (THETAA.LE.PI) TA1 = (THETAA/PI)
         IF (THETAA.GT.PI) TA1 = (2 - THETAA/PI)
         IF (THETAB.LE.PI) TB1 = (THETAB/PI)
         IF (THETAB.GT.PI) TB1 = (2 - THETAB/PI)
         ANGSIG(ANG,1) = ANGLE
         ANGSIG(ANG,2) = (TA1 - TB1)/(TA1 + TB1)
C
         WRITE (2,200) ANGLE, ANGSIG(ANG,2)
200      FORMAT (F5.1,6X,F8.3)
C
         WRITE (3,300) ANGLE, TA1
300      FORMAT (F5.1,6X,F8.3)
C
         WRITE (1,550) ANGSIG(ANG,1), THETAA, ANGSIG(ANG,2)
550      FORMAT (F5.1,6X,F5.3,6X,F8.3)
C
```

```
600   CONTINUE
C
      WRITE (1,650)
650   FORMAT ('RUN A DEGRADED CHANNEL? (1 = YES)')
      READ (1,*) ANS
      IF (ANS.NE.1.0) GOTO 825
C
      DO 800 ANG =  10,360,10
         ANGLE = FLOAT(ANG)
         THETAA = ANG*PI/180.0
         THETAB = DELTHA + THETAA
         IF (THETAB.GT.TWOPI) THETAB = THETAB - TWOPI
         IF (THETAA.LE.PI) TA1 = 0.50*(THETAA/PI)
         IF (THETAA.GT.PI) TA1 = 0.50*(2 - THETAA/PI)
         IF (THETAB.LE.PI) TB1 =       (THETAB/PI)
         IF (THETAB.GT.PI) TB1 =       (2 - THETAB/PI)
         ESIG(ANG) = (TA1 - TB1)/(TA1 + TB1)
C
         WRITE (1,555) ANGLE, THETAA, ESIG(ANG)
555      FORMAT (F5.1,6X,F5.3,6X,F8.3)
C
         WRITE (12,700) ANGLE, ESIG(ANG)
700      FORMAT (F5.1,6X,F8.3)
C
         WRITE (13,750) ANGLE, TA1
750      FORMAT (F5.1,6X,F8.3)
C
800   CONTINUE
C
825   WRITE (1,850)
850   FORMAT ('FIND THE DETECTION ERRORS? (1 = YES)')
      READ (1,*) ANS
      IF (ANS.NE.1.0) GOTO 9999
C
      DO 1000 ANG = 10,360,10
         ANGLE = FLOAT(ANG)
         ERROR = ANGSIG(ANG,2) - ESIG(ANG)
         WRITE (7,950) ANGLE, ERROR
950      FORMAT (F5.1,6X,F8.3)
1000  CONTINUE
C
9999  STOP
      END
C$ENTRY
```

REFERENCES

1. D.H. McMahon, A.R. Nelson, and W.B. Spillman, "Fiber-optic transducers," IEEE Spectrum, p. 24, December, 1981.

2. C.M. Davis, "Fiber Optic Sensors: an Overview," Optical Engineering, vol. 24, no. 2, p. 347, 1985.

3. J.L. McMillan and S.C. Robertson, "Single-mode Optical Fiber Sensors," GEC Journal of Research, vol. 2, no. 2, p. 119, 1984.

4. T.G. Giallorenzi, J.A. Bucaro, A. Dandridge, G.H. Sigel, J.H. Cole, S.C. Rashleigh, and R.G. Priest, "Optical Fiber Sensor Technology," IEEE J. Quant. Elect., QE-18, pp. 626-664, 1982.

5. G. Meltz and E. Snitzer, "Thermal Dependence of Cross Talk in Multicore Fibers," JOSA, vol. 19, no. 10, p. 1462, 1979.

6. E. Snitzer, J.R. Dunphy, and G. Meltz, "Fiber Optic Strain Sensors," in Proceedings, Interntl. Conf. on Fiber Optic Rotation Sensors and Related Technologies," (Springer, New York, 1982).

7. W.B. Spillman and D.H. McMahon, "Frustrated-total-internal-reflection multimode fiber-optic hydrophone," Applied Optics, vol. 19, p. 113, 1980.

8. A.R. Nelson, D.H. McMahon, and R.L. Gravel, "Passive multiplexing system for fiber-optic sensors," Applied Optics, vol. 19, p. 2917, 1980.

9. W.B. Spillman and D.H. McMahon, "Schlieren multimode fiber-optic hydrophone," Appl. Phys. Lett., vol. 37, no. 2, p. 145, 1980.

10. S.K. Yao, C.K. Asawa, and G.F. Lipscomb, "Stabilization of Single and Multimode Fiber Optical Microbend Sensors," Electron. Lett., vol. 19, no. 7, p. 257, 1983.

11. N. Lagakos, W.J. Trott, T.R. Hickman, J.H. Cole, and J.A. Bucaro, "Microbend Fiber-Optic Sensor as Extended Hydrophone," IEEE Trans. Microwave Theory and Techn., vol. MTT-30, no. 10, p. 1621, 1982.

12. D.C. Marvin and N.A. Ives, "Wide-range fiber-optic strain sensor," Applied Optics, vol. 23, no. 23, p. 4212, 1984.

13. J.A. Bucaro, H.D. Dardy, and E. Carome, "Fiber optic hydrophone," J. Acoust. Soc. Amer., vol. 62, p. 1302, 1977.

14. J.A. Bucaro, and T.R. Hickman, "Measurement of sensitivity of optical fibers for acoustic detection," Applied Optics, vol. 18, p. 938, 1979.

15. A.D. Kersey, D.A. Jackson, and M. Corke, "A Simple Fibre Fabry-Perot Sensor," Optics Comm., vol. 45, no. 2, p. 71, 1983.

16. T. Yoshino, K. Kurosawa, K. Itoh, and T. Ose, "Fiber-Optic Fabry-Perot Interferometer and Its Sensor Applications," IEEE Trans. Microwave Theory and Tech., vol. MTT-30, no. 10, p. 1612, 1982.

17. M. Corke, A.D. Kersey, D.A. Jackson, and J.D.C. Jones, "All-Fibre κMichelsonκ Thermometer," Elect. Lett., vol. 19, no. 13, p. 471, 1983.

18. N. Lagakos, E.U. Schnaus, J.H. Cole, J. Jarzynski, and J.A. Bucaro, "Optimizing fiber coatings for interferometric acoustic sensors," IEEE Trans. Microwave Theory and Techn., vol. MMT-30, no. 4, p. 529, 1982.

19. A. Dandridge, A.B. Tueten, G.H. Sigel,Jr., E.J. West, and T.G. Giallorienzi, "Optical fiber magnetic field sensor," Electron. Lett., vol. 16, p. 408, 1980.

20. F. Bucholtz, K.P. Koo, and G.H. Siegel, Jr., "Field annealing of metalic glass ribbons for fiber-optic sensors," Third Intnl. Conf. on Optical Fiber Sensors (San Diego, CA), February, 1985.

21. J.P. Wilson and R.E. Jones, "Magnestostricive fiber-optic sensor system for detecting dc magnetic fields," Optics Letters, vol. 8, no. 6, p. 333, 1983.

22. K.P. Koo and G.H. Sigel, "Characteristics of fiber-optic magnetic field sensors employing metalic glasses," Optics Letters, vol. 7, no. 7, p. 334, 1982.

23. D.R. Biswas and S. Raychaudhuri, "Optomechanical properties of long-length nickel-coated optical fibers," Third Intnl. Conf. on Optical Fiber Sensors (San Diego, CA), February, 1985.

24. H. Tolaat, W.J. Moore, J. Jarzynski, and J.A. Bucaro, "Fourier Transform IR photoacoustic study of piezoelectric coatings on optical fibers, Third Intn. Conf. on Optical Fiber Sensors (San Diego, CA), February, 1985.

25. J.L. McMillan and S.C. Robertson, "Dual-mode optical fiber interferometric sensor," Electron. Lett., vol. 20, p. 136, 1984.

26. M.R. Layton and J.A. Bucaro, "Optical fiber acoustic sensor utilizing mode-mode interference," Applied Optics, vol. 18, no. 5, p. 666, 1979.

27. K. Bohm, P. Martin, K. Peterman, E. Wiedel, and R. Ulrich, "Low-drift fiber gyro using a superluminecent diode," Electron. Lett., vol. 17, p. 352, 1981.

28. R.A. Bergh, H.C. Tefereve, and H.J. Shaw, "All-single-mode-fiber-optic gyroscope," Optics Letters, vol. 6, p. 198, 1981.

29. A.M. Smith, "Polarization and magnetooptic properties of single mode optical fiber," Applied Optics, vol. 17, p. 52, 1978.

30. S.C. Rashleigh, "Magnetic-field sensing with a single-mode fiber, Optics Letters," vol. 6, p. 19, 1981.

31. S.C. Rashleigh, "Acoustic sensing with a single coiled mono-mode fiber," Optics Letters, vol. 5, p. 392, 1980.

32. Y. Hanisaki, T. Miyamoto, Y. Kuhara, M. Katoh, K. Tada, S. Takeuchi, and T. Nakahara, "Optical Fiber Sensor for the Measurement of Electric Field Intensity and Voltage (OPSEF)," Fiber and Integrated OPtics, vol. 3, no. 4, p. 383, 1981.

33. Y. Hamasaki, H. Gotoh, M. Katoh, and S. Takeuchi, "OPSEF: An Optical Sensor for Measurement of High Electric Field Intensity," Elect. Lett., vol. 16, no. 11, p. 406, 1980.

34. R.H. Stolen and S.C. Rashleigh, "Polarization-holding fibers," Third Intnl. Conf. on Optical Fiber Sensors (San Diego, CA), February, 1985.

35. M. Corke, J.D.C. Jones, A.D. Kersey, and D.A. Jackson, "Dual Fabry-Perot interferometers implemented on a single monomode optical fiber," Third Intnl. Conf. on Optical Fiber Sensors (San Diego, CA), February, 1985.

36. H. Inaba, T. Kobayasi, M. Hirama, and M. Hamza, "Optical-Fibre Network System for Air-Pollution Monitoring over a Wide Area by Optical Absorption Method," Electron. Lett., vol. 15, no. 23, p. 749, 1979.

37. E. Gatt, "Color Multiplexing of Signals onto Optical Fibers using Interference Filters," Inland Motor, Patent Disclosure, 1985.

38. O. Sezerman, B.E. Paton, G.A. Klassen, and J.A. Armour, "Fiber-optic laser velocimeter for medical applications," Third Intnl. Conf. on Optical Fiber Sensors (San Diego, CA), February, 1985.

39. M.C. Hutley, "Optical fiber sensors for displacement measurement," Proc. SPIE Int. Soc. Opt. Eng., vol. 376, p. 37, 1983.

40. K.A. James, W.H. Quick, and V.H. Strahan, "Optical temperature sensor with digital output," Applied Optics, vol. 22, no. 20, 1983.

41. B. Culshaw, D.E.N. Davies, and S.A. Kingsley, "Fibre optic strains pressure and temperature sensors," Proc. 4th European Conf. on Opt. Comm., Genoa, Italy, 1978.

42. G.L. Tangonan, D.I. Persechini, R.J. Morrison, and J.A. Wysocki, "Current Sensing with Metal-Coated Multimode Optical Fibres," Elect. Lett., vol. 16, no. 25, p. 958, 1980.

43. K.D. Bennett, "Fiber Optic Sensors Based on Mode Modulation Techniques," unpublished.

44. R.L. Crane, "Fiber optics for a damage assessment system for fiber reinforced plastic composite naval structures," ARO/DARPA Workshop on NDE of Polymers and Polymer-Based Composites (Wrightsville Beach, NC), April 1982.

45. R.L. Crane, A.B. Macander, and J. Gagoriik, "Fiber optics for a damage assesment system for fiber reinforced plastic composite structures," Review of Progress in Quantitative NDE (San Diego, CA), August 1982.

46. G. Meltz and J.R. Dunphy, "Quantitative fiber-optic techniques for the nondestructive evaluation of composites," Review of Progress in Quantitative NDE (Williamsburg, VA), June 1985.

47. R.O. Claus and J.C. Wade, "Interferometric techniques using imbedded optical fibers for the quantitative NDE of composites," Review of Quantitative NDE, vol. 28, pp. 1731-1738, 1984.

48. R.O. Claus and J.C. Wade, "Distributed strain measurement in a rectangular plate using an array of optical fiber sensors," J. Nondestructive Evaluation, vol. 41, p. 106, 1983.

49. B.S. Jackson, "Optical Time Domain Reflectometry as a Nondestructive Evaluation Technique for Composite Materials," M.S. Thesis, Virginia Tech, 1984.

50. A.J. Rogers, "Polarization-optical time domain reflectometry: a technique for the measurement of field distributions," Applied Optics, vol. 20, no. 6, p. 1060, 1981.

51. G.L. Wilkes, "CHE5120 - Rheo-optics of Polymers," Class Notes, Spring, 1984.

52. F.P. Kapron,"Fiber-optic system tradeoffs," IEEE Spectrum, p. 68, March, 1985.

53. R.O. Claus, B.S. Jackson, and K.D. Bennett, "Nondestructive testing of Composite Materials by OTDR in Imbedded Fibers," Proceedings, SPIE International Sympsium (San Diego, CA), August, 1985.

54. R. Olshansky, "Mode Coupling Effects in Graded-Index Optical Fibers," Applied Optics, vol. 14, no. 4, p. 935, 1975.

55. D. Gloge, "Bending loss in multimode fibers with graded and ungraded core index," Applied Optics, vol. 11, no. 11, p. 2506, 1972.

56. D. Marcuse, "Field deformation and loss caused by curvature of optical fiber," J. Optic. Soc. Amer., vol. 66, no. 4, p. 311,1976.

57. R.M. Gill, Carbon Fibres in Composite Materials London: Iliffe Books, 1972.

58. M. Grayson, Ed., Encyclopidia of Composite Materials and Components, New York: John Wiley and Sons, 1983.

59. K.D. Bennett, "Bending Loss in Multimode Fibers," unpublished.

60. J.R. Dunphy and G. Meltz, United Technologies Research Center, personal communications, August, 1985.

61. Y.F. Guo, Engineering Science and Mechanics Department, Virginia Tech, personal communications, July 1985.

62. The Institution of Metallurgists, Composite Materials, New York: American Elsevier Publishing Company Inc., 1966.

63. W.G. Potter, Uses of Epoxy Resins, London: Newnes-Butterworths, 1975.

64. E.A. Smith, Ed., Carbon Fibres, London: Morgan-Grampian (Publishers) Ltd., 1970.

65. W.T. Freeman, NASA-Langley Research Center, Materials Division, personal communications, June, 1985.

66. D. Gloge, "Bending Loss in Multimode Fibers with Graded and Ungraded Core Index," Applied Optics, vol. 11, no. 11, p. 2506, 1972.

67. D. Marcuse, "Losses and Impulse Response of a Parabolic Index Fiber with Random Bends," Bell Syst. Tech. J., vol. 52, no. 8, p. 1423, 1973.

68. A.W. Snyder and D.J. Mitchell, "Bending Losses of Multimode Optical Fibers," Electron. Lett., vol. 10, no. 1, p. 11, 1974.

69. W.B. Gardner, "Microbending Loss in Optical Fibers," Bell Syst. Tech. J., vol. 54, p. 457, 1975.

70. D. Marcuse, "Field Deformation and loss caused by curvature of optical fibers," J. Opt. Soc. Am., vol. 66, p. 311, 1976.

71. W.A. Gambling, H. Matsumara, and C.M. Ragdale, "Curvature and Microbending Losses in Single-Mode OPtical Fibers," Opt. Quantum, Electron., vol. 11, p. 43, 1979.

72. J.N. Fields, "Attenuation of a parabolic-index fiber with periodic bends," Appl. Phys. Lett., vol. 36, no. 10, p. 799, 1980.

73. M.F.J. Diemeer and E.S. Trommel, "Fiber-optic microbend sensors; sensitivity as a fuction of distortion wavelength," Optics Letters, vol. 19, p. 260, 1984.

74. A. De Jongh, M.F.B. Diemeer, E.S. Trommel, and A.H.E. Breuls, "Simple Fibre-Optic Sensor for Detecting Water Penetration into Optical Fibre Cables," Electron. Lett., vol. 19, no. 23, p. 980, 1983.

75. C.M. Lemrow and V.A. Bhagavtula, "Advanced Fiber Designs," Laser Focus, p. 82, March, 1982.

76. G. Meltz, J.R. Dunphy, W.W. Morey, and E. Snitzer, "Cross-talk fiber-optic temperature sensor," Applied Optics, vol. 22, no. 3, 1983.

77. F. Reynard, Reynard Enterprises Inc., personal communications, July, 1985.

78. Call for proposal, "Advanced Optical POsition Transducer," U.S. Army Contract, DAAJ02-85-Q-0006, May, 1985.

79. Boston Electronics, Optical Chopper Model 300C/CD, Sales Literature.

80. Frequency Control Products, Inc., Fiberswitch In-Line Optical Fiber Light Chopper, Type SWC, Sales Literature.

The vita has been removed from the scanned document